Copyright Undertaking

This thesis is protected by copyright, with all rights reserved.

By reading and using the thesis, the reader understands and agrees to the following terms:

1. The reader will abide by the rules and legal ordinances governing copyright regarding the use of the thesis.

2. The reader will use the thesis for the purpose of research or private study only and not for distribution or further reproduction or any other purpose.

3. The reader agrees to indemnify and hold the University harmless from and against any loss, damage, cost, liability or expenses arising from copyright infringement or unauthorized usage.

Pao Yue-kong Library, The Hong Kong Polytechnic University, Hung Hom, Kowloon, Hong Kong

http://www.lib.polyu.edu.hk

The Hong Kong

Polytechnic University

Department of Applied Physcis

Piezoelectric Transducers for

Nebulizer Application

Xu, Wencheng

A thesis submitted in partial fulfilment of the

requirements for the degree of

Master of Philosophy

August, 2006

CERTIFICATION OF ORIGINALITY

I hereby declare that this thesis is my own work and that, to the best of my knowledge and belief, it reproduces no material previously published or written, nor material that has been accepted for the award of any other degree or diploma, except where due acknowledgment has been made in the text.

_____ (Signed)

_____Xu Wencheng_____ (Name of Student)

Abstract

This thesis presents the study on new liquid nebulizer devices which are based on ultrasonic horn transducers driven by different types of piezoelectric ceramics.

The design of the nebulizer device mainly includes two parts, the studies on materials and the transducer structures. The material fabrication, property measurements and resonance characterization of piezoelectric ceramics, including lead zirconate titanate (PZT) and two types of lead-free ceramics $(Ba_{0.95}Sr_{0.05})(Ti_{0.95}Zr_{0.05})O_3$ (BSZT) and $(Na_{0.5}K_{0.5})NbO_3$ (KNN) are presented and discussed. Theoretical studies of the ultrasonic horns and simulations of stepped horn transducers by finite element method are included in this thesis. Experiments of displacement and electrical impedance measurements are conducted to evaluate the performances of these transducers. Finally, the nebulization tests of the device prototypes based on different piezoceramics have been performed.

Original contributions reported in this thesis include:

1. A new, small in size, orientation controllable nebulizer prototype has been designed and fabricated. The nebulizer is driven by a PZT ceramic ring and works under an AC voltage equal to or higher than 27V in

i

amplitude.

2. A hard type lead-free ceramic KNN ring has been deployed in the nebulizer as a substitute of PZT ceramic. The lead-free nebulizer functions well but requires higher driving voltage comparing with the PZT-based ones.

3. A stepped horn transducer based on lead-free piezoelectric ceramic disk (BSZT) has been developed. It has a good displacement performance which is comparable with PZT based ones.

Lists of Publications

Journal Papers:

W. C. Xu, D. Y. Wang, X. G. Tang, Y. Wang, and H. L. W. Chan, "Tunable Dielectric Behaviors of Barium Zirconate Titanate Thin Film", *Integrated Ferroelectrics*, vol. 80, pp. 443-449, 2006.

W. C. Xu, K. H. Lam, S. H. Choy and H. L. W. Chan, "A Stepped Horn Transducer Driven by Lead-free Piezoelectric Ceramics", submitted to *Integrated Ferroelectrics*.

Acknowledgements

I would like to express my heartfelt appreciations to my supervisor, Prof. Helen L. W. Chan, for her constant support and encouragement, invaluable advice and guidance throughout the whole period of my research study, and for choosing the project interesting and suitable for me. I am truly grateful for all the time and efforts she has devoted to me, which helps me complete my two-year M.Phil. studies.

I would also like to thank Dr. Yu Wang, for his guidance and help with my initial research topic in the first two months of my studies. As the teaching assistant of Dr. Wang, I learned teaching skills and other knowledge which I cannot find in textbooks.

Thanks are also due to Dr. Kin Wing Kwok. He has shown continuous interest and has spent a lot of time conferring with me and offering constructive opinions to my nebulizer research.

To Dr. K. H. Lam, who has provided constant help, discussion, and assistance through out my research work, I give my sincere thanks. I would like also to give my thanks to Dr. D. Y. Wang, Mr. S. H. Choy, Mr. C. L. Sun, and Dr. D. M. Lin for their kind help and assistance.

I gratefully acknowledge the financial support from the Innovation and

Contents

List of Figures

List of Tables

Chapter 1

Introduction

1.1   Microdrop Generation

Nebulizers find important medical applications such as drug delivery which has been widely used in asthma therapies. Nebulizers convert liquids into aerosol particles. Essentially, the process of nebulization is the generation of microdrops of liquid. Other than nebulizers, microdrops are of great use in scientific and industrial applications, e.g. in particle physics, cell sorting, inkjet printing, displays manufacturing etc. [1–3].

1.1.1   Methods of Generating Microdrops

Robert Millikan performed the famous levitated oil drop experiment to determine the value of electronic charge in the early 1900s. He used a spray atomizer to aerosolize the low-viscosity watch oil [1]. This traditional method of generating microdrops is simple but rough. Nowadays, for applications requiring greater drop generation precision and efficiency, many other ways

have been developed [4].

Acoustically Disrupted Continuous Fluid Jet   A continuous fluid jet is produced by pressuring the fluid reservoir, which causes the fluid to be jetted out as a continuous stream of approximately the diameter of the ejection nozzle (Figure 1.1). The modulation voltage is applied on the cylindrical piezoelectric element. The ejector is excited with an acoustic waveform that causes instability and standing waves on the fluid stream as it emerges from the nozzle orifice hole. The standing wave forms the liquid stream into individual drops [5]. The diameter of the drops produced by the fluid stream is approximately twice the diameter of the ejection aperture. According to the rheology of the fluid, the drop production rate and the size of the drops can be controlled by altering the velocity of ejection and the frequency of driving signal.

Piezoelectric Direct Pressure Pulse   Piezoelectric elements are used to change the volume of the liquid reservoir in order to produce the fluid ejection and retraction pressure pulse. The advantage of piezoelectric actuation is that the pressure pulse rise and fall time can be tailored to optimize the drop generations and dynamically alter the diameter of the ejected drops [6,7]. As shown in Figure 1.2, the flat-drive plate design is suitable for being manufactured in miniaturized form by integrated circuit fabrication process.

Focused Acoustic Beam Ejection   The use of focused ultrasonic beams to actuate microdrop ejection is recently invented and developed at Xerox
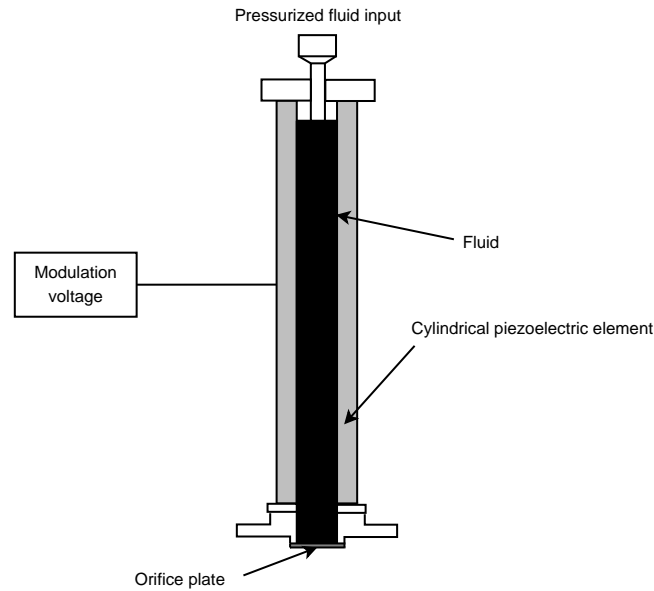
Figure 1.1   Continuous fluid jet microdrop generator. Monodisperse microdrops are formed from a continuous fluid jet by the formation of nodes along the fluid jet from an externally impressed source of acoustic energy.
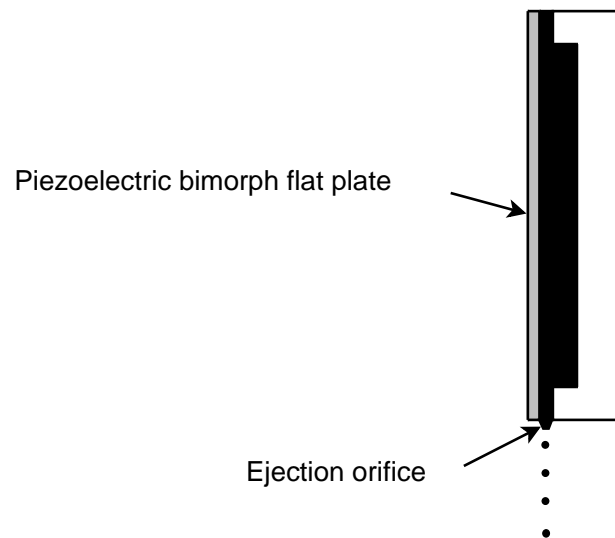
Figure 1.2   Piezoelectrically driven drop-on-demand microdrop ejectors.

PARC [8, 9]. This method works by focusing an ultrasound beam with an acoustic lens onto the surface of a fluid meniscus, using the acoustic pressure transient generated by the focused tone burst to eject a fluid jet (Figure 1.3). This technique has a very large practical advantage of being immune to jamming of the ejection apertures, since the ejection aperture is simply a region defined over a large, exposed fluid surface by the diameter of the focal spot. This can allow a reliable ejection of fluids that may otherwise clog small aperture holes.
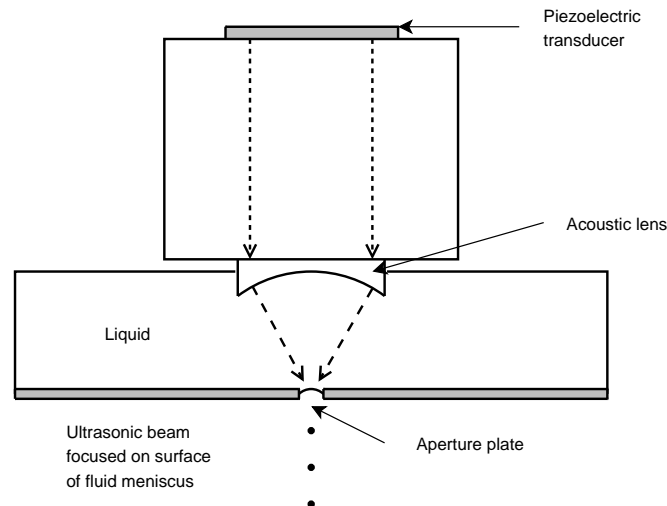
Figure 1.3   Focused acoustic beam microdrop ejector. A high frequency gated continuous wave ultrasonic source is focused on the surface of a fluid reservoir. The acoustic radiation pressure is used to produce a localized jet that forms into microdrops.

Flextensional Aperture Plate Ejector   This ejector is unique as it combines the ejection aperture plate and the actuating mechanism into a single structure, as shown in Figure 1.4. The flexible orifice plate is generally actuated by the thin film piezoelectric material deposited on the orifice mem-

brane [10, 11]. The advantage of this technology is that due to the integration of ejection and actuation, it has the potential for making highly spatially dense two-dimensional arrays of ejectors. Additionally, the flexible plate could also be actuated by thermal bimorph thin film or by electrostatic attraction of the aperture plate to an inner electrode [12].
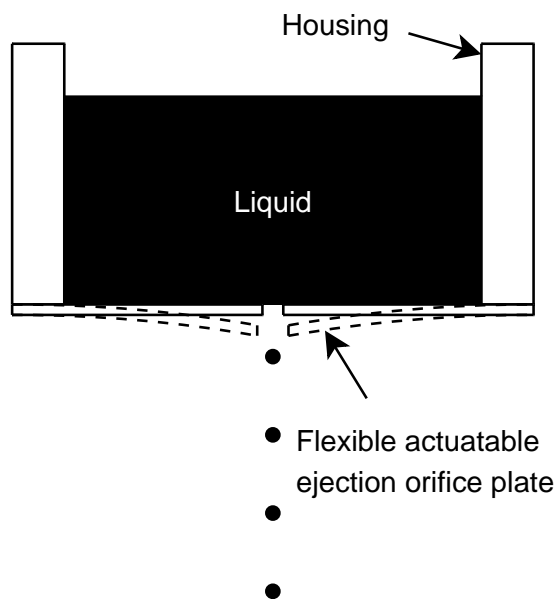
Figure 1.4   Flextensional aperture plate ejector. This design combines the ejection orifice plate with the mechanical actuator.

Electrohydrodynamic Inkjet   Experiments show that an applied electric field can draw fluid from a capillary nozzle. Electrohydrodynamic inkjets operate using this phenomenon (Figure 1.5). The electrohydrodynamic inkjet functions by pressurizing the fluid so that it forms a convex meniscus. An electric field is applied that draws out this convex meniscus into a sharp cone. When the electric field strength is large enough to overcome the surface tension, the liquid can break free. Depending on the static biasing field

and the duration and amplitude of the ejection pulse, this technique can be used to produce a wide-angle spray, a continuous stream, or under special conditions, discrete mono-disperse drops [13–15]. Due to the way the electric field draws the meniscus out into a sharp cone, this type of ejector is capable of producing drops much smaller than the aperture ejectors. The field strength needed to initiate drop ejection using this method is about 1000kV/mm; typical electrode gaps were 0.5mm. Pulse width is in the tens of microseconds to a few milliseconds range.
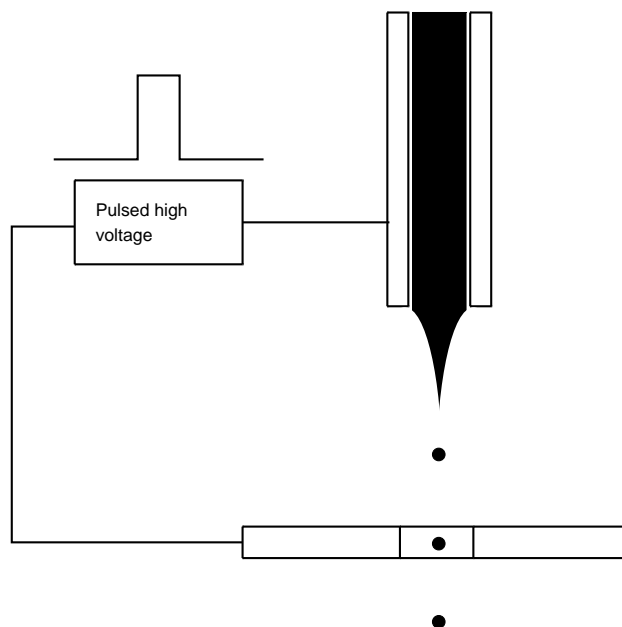
Figure 1.5   Electrohydrodynamic inkjet. An electrohydrodynamic inkjet uses a high electric field of ~ 1000kV/mm to pull fluid from a specially shaped and pressurized capillary tube. Under special conditions of proper fluid rheology, capillary geometry and precise control of the electric field monodisperse drops can be generated.

There are many other technologies used for microdrop generation, such as thermal inkjet (bubble jet) [16,17], liquid spark inkjet [18], electro-rheological fluid ejector [19], and liquid ink fault tolerant (LIFT) process [20]. Different

technique has its own advantages. However, not all of the above mechanism of microdrop generation can be used as a nebulizer, since high frequency of operation, quick response to signal and lower viscosity of the liquid are required in the process of nebulization.

1.1.2 Kinetics of Microdrops

Reynolds Number and Stokes Law   When designing a nebulization system with the aim to target the atomized drops accurately into predetermined locations, it is important to know the factors which govern the motion of the microdrops. A nebulized microdrop is small enough so that it is in the regime where forces associated with viscous flow resistance to motion defined by Stokes Law become the dominant factor. Reynolds number is a measure of the ratio of the dynamic pressure drag force to the Stokes viscous drag force on a given object moving through a fluid media, namely, air in this case. The Stokes drag force is first order independent of air density and is proportional to the first power of the relative speed of the object. The Reynolds number is defined as [4]:

$$Re = vd/\nu \tag{1.1}$$

where v is the velocity of the drop relative to air, d is the diameter of the drop and ν is the kinematic viscosity of air, which equals the viscosity of air divided by the density of air. The resistance to the drop caused by viscous resistance of the air is [4]:

$$F_{Stokes} = 3\pi\eta dv \tag{1.2}$$

where η is the viscosity of air (182.7×10^{-6}g/cm·s at standard temperature and pressure). The origin of this force is from the viscosity of the medium, in this case, air. Viscosity is roughly defined as the resistance of a medium to a change in its shape. The energy needed to deform the viscous medium so that objects can travel through is the source of the Stokes resistance.

Calculating the behavior of microdrops moving through air is significantly different from calculating the macroscale ones. For macroscale objects, the primary aerodynamic force is dynamic drag, which is proportional to the square of the object's speed and is proportional to the density of air. For microdrops the principal aerodynamic force is Stokes drag, which is proportional to the first power of the drop speed and is independent of the air density. The Reynolds number of a falling raindrop is about 10^3, while that for a 100μm water drop traveling in air is 1.8; for a 50μm water drop, Re is 0.3 and a 10μm water drop has a Reynolds number in the order of 10^{-3}. Obviously, in the region of 10μm or smaller, the Stokes drag dominates.

Cunningham's correction factor is a secondary factor that needs to be added to the simple form of the Stokes Law equation when highly accurate quantitative calculation is required for the motion of fluid microdrops. It is a correction for the atmosphere not being a perfect continuum. The net result is that the resistance of air is slightly less than that predicted by Stokes Law by a factor of $1/C_C$. The error is larger for smaller drops, about 16% for 1-micron-diameter drops and falls to a correction of less than 2% for 10-micron-diameter drops [4]. The Cunningham correction factor is:

$$C_C = 1 + (2\lambda/d)(A + Qe^{-bd/2\lambda}) \qquad (1.3)$$

Where the coefficients $A = 1.252$, $Q = 0.399$, $b = 1.100$, $\lambda = 0.065\mu$m, and d is the diameter of the drop in microns.

Terminal Velocity   The terminal velocity of a fluid microdrop traveling in air is calculated by setting the gravitational force equal to the drag force. The terminal velocities of drops smaller than 100 microns were calculated from Stokes Law including the Cunningham's correction. The movements of drops smaller than 0.1 microns are dominated by Brownian motion.

Table 1.1   Terminal velocities in air of water drops ($\rho =1$g/cm^3) [21].

Diameter (μm)	Velocity (mm/s)
0.1	9.0×10^{-4}
0.5	1.0×10^{-2}
1.0	3.5×10^{-2}
2.0	1.3×10^{-1}
5.0	7.7×10^{-1}
10	3.0×10^{0}
25	1.9×10^{1}
50	7.5×10^{1}
100	2.6×10^{2}
400	1.6×10^{3}
1000	4.0×10^{3}
5800	9.2×10^{3}

Table 1.1 [21] gives the terminal velocities of water drops with different diameters. The nebulizers typically eject the drops with the diameters in

several microns to 0.1 millimeters range. The initial velocity of the ejected drops is usually three orders of magnitude faster than the final terminal velocities. For such applications, understanding the nonequilibrium kinetics of the behavior of the ejected drops can be important in designing the nebulizers or ejectors.

Relaxation Time Constant The relaxation time constant, τ, is a measure of how fast the motion of the drop comes to steady state after initial ejection, changes in local air speed or application of external forces induced by electric or magnetic fields. A 5-micron-diameter microdrop has a relaxation time of 7.8×10^{-5} seconds.

Streaming Drops moving through air produce motion in the air that affects the motion of other nearby drops. This can be seen clearly when operating drop generators at high rates. One manifestation of inter-drop coupling via the media (air) is the droplet streaming. Streaming is the tendency for droplets ejected at a high rate from a single source to collimate into a single well defined stream. When taking precise measurements of drop positions and velocities, tens of diameters away can significantly affect the motion of the measured drop. This increases the velocity of the drop from what it would have if it is isolated from other droplets. Streaming also collimates the drops which tend to deviate from the average trajectory.

Brownian Motion Microdrops generated by a nebulizer are sometimes in a small size range in which Brownian motion can influence the motion of the drop. For small drops the Brownian displacement over a few seconds can be

many times of the diameter of the drop. A 1.0-micron-diameter drop can have a Brownian motion displacement of about 7μm in one second, which is seven times of its diameter. The mean distance that Brownian motion will deviate the trajectory of a particle from its predicted path over a time t, is given by [4]:

$$\Delta x = \sqrt{2Dt} \tag{1.4}$$

where D is the diffusion coefficient: $D = kT/F_{drag}$. For microdrops in air, the drag force F_{drag} is given by Stokes Law, hence the Brownian trajectory deviation can be written as:

$$\Delta x = \sqrt{\frac{2kTt}{3\pi\eta vd}} \tag{1.5}$$

1.2 Reviews on Nebulizer Technology

1.2.1 The Development of Nebulizers

Nebulizer, defined as the device which converts liquids into aerosol particles, has been developed and used for a long time. The first use of nebulizers might be in ancient Greece, by Pedanus Discorides, the father of the science of pharmacy, who, during the first century prescribed inhaled fumigation [22]. The most famous use of a nebulizer must be Robert Millikan, he performed his well-known levitated oil drop experiment to determine the value of the electronic charge in the early 1900s with fluid microdrops made by aerosolizing low-viscosity watch oil [1]. Nowadays, nebulizers find wide applications, especially in some medical devices. For example in the therapy of asthma,

nebulizers are used to generate aerosol particles of the medication and to deposit them in the lower respiratory tract of human beings [23, 24].

According to the actuation mechanism, typically there are two types of traditional nebulizers which have been widely developed. One is pneumatic (jet) nebulizers, which use the energy provided by compressed gas flow to generate an aerosol. The second type is ultrasonic nebulizers. An ultrasonic nebulizer uses electricity to vibrate a piezoelectric crystal at high frequencies. Standing waves are generated when the high-frequency vibrations are focused onto the surface of the medication solution. Liquid droplets break off from the wave crest to form an aerosol.

Pneumatic (Jet) Nebulizers   Jet nebulization was the first technical operation developed for aerosol production (Figure 1.6). It uses gas flow either from a compressor or a central air supply. The gas passes through a small aperture in the nebulizer in order to pick up and atomize the liquid drug. The aerosol that is generated by atomization contains large and small droplets, and is driven to a baffle. Large droplets are impacted by the baffle and forced onto the side of the nebulizer to be recycled in liquid form in a reservoir. More than 90% of the droplets produced by atomization are selected and recirculated in the nebulizer to be recycled in the liquid drug reservoir. Small droplets are transported out of the nebulizer by the gas to be inhaled by the patient.

The drug mass loaded in the nebulizer is greater than that delivered as an aerosol to the patient. Part of the drug mass is trapped in the nebulizer as residual mass and another significant part is lost in the form of aerosol

particles in the ambient air during exhalation as leakage.

There are three types of jet nebulizers, which are defined by their output during inhalation [25].

- Standard unvented nebulizers are those with a constant output during the patient's inhalation and exhalation phases.

- Breath-enhanced vented nebulizers produce a higher aerosol output during the inhalation phase and lower output during exhalation.

- Dosimetric or breath-actuated nebulizers only produce an aerosol during the inhalation phase or a fraction of it.

Jet nebulizers atomized all types of liquid (solutions, suspensions, oils, etc.). The residual mass is about 50% of the drug mass loaded into the nebulizer and the aerosol is cooled. Jet nebulization can partially destroy brittle active drug compounds (e.g. liposomes, adenovirus), due to the mechanical stress of atomization. They are often portable and disposable, but compressors are often noisy and bulky.

Ultrasonic Nebulizers   Ultrasonic nebulizers use the vibration of a piezo-electric crystal to generate the aerosol (Figure 1.7). Vibrations are transmitted to a liquid drug, generating a liquid drug fountain comprising large and small droplets. Large droplets drop into the liquid drug reservoir or are thrown onto the side of the nebulizer and recycled. Small droplets are stored in the nebulization chamber to be inhaled by the patient or leave the nebulizer with the airflow produced by a ventilator. Like the jet nebulizer, some residual mass is trapped in the nebulizer, but there is little leakage since
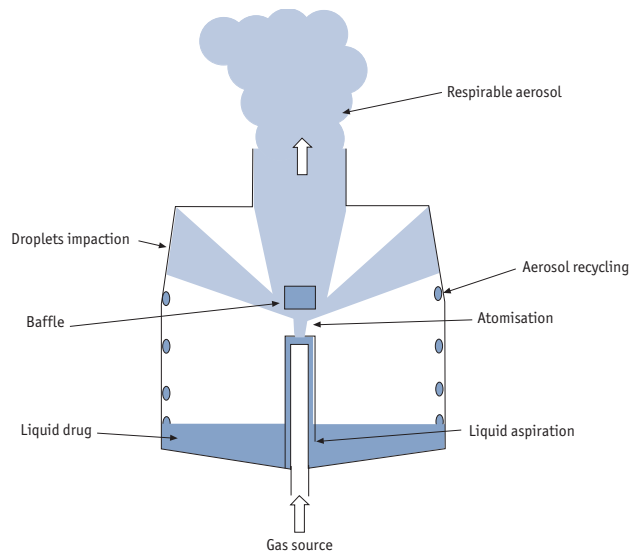
Figure 1.6 The working principle of a pneumatic (jet) nebulizer [26].

there is no gas source to transport the aerosol out of the nebulizer during exhalation.
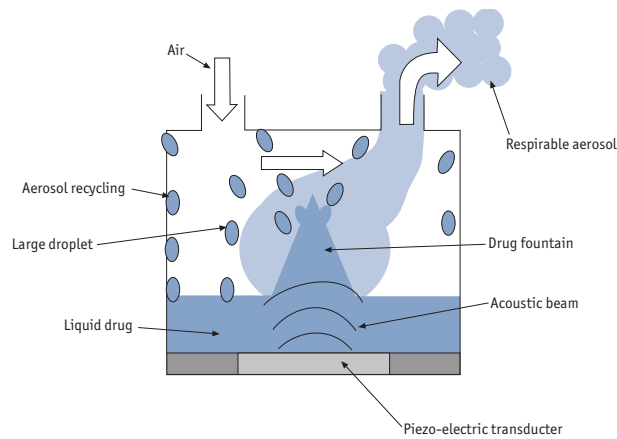
Figure 1.7 The working principle of an ultrasonic nebulizer [26].

There are two types of ultrasonic nebulizers.

- Standard nebulizers are those where the drug is directly in contact with the piezoelectric transducer. This contact causes the drug tem-

perature to increase due to heating of the transducer. In addition the piezoelectric transducer is difficult to disinfect.

- Ultrasonic nebulizers with a water interface use a volume of water between the piezoelectric transducer and a separate reservoir for the drug. Water reduces drug heating and the drug is not in contact with the transducer.

Ultrasonic nebulizers are not capable of nebulizing suspensions or liquids with high viscosity or a high surface tension [27], the residual mass is often more than 50% of the drug mass loaded in the nebulizer and the aerosol is heated. Ultrasonic nebulizers are silent, but often bulky.

The traditional nebulizers have advantages in their simple constructions and low fabrication costs but they are generally large in size, low in efficiency and poor in precision and consistency of the aerosol depositions. Meanwhile, the demand for aerosol therapy, however, are rapidly expanding: aerosols are required to deliver drugs to the respiratory tract for systemic effects [28] and to deliver genes to the respiratory tract [29]. Therefore, an advanced technology of nebulizers is demanded to have improved efficiency, precision, and consistency of aerosol deposition in the lung, to use new formulations, and to allow efficient aerosolization of suspensions and drugs with high lipid solubility [29, 30]. In addition, there needs to be a concerted effort to protect respiratory therapists and other health care workers from occupational exposure to aerosolized drugs [31].

1.2.2   New Nebulizer Technology

Several manufacturers (Aerogen, Mountain View, California; Omron, Vernon Hills, Illinois; ODEM, Melbourn, United Kingdom; and Pari Respiratory Equipment, Monterey, California) have developed new nebulizer technology that uses a vibrating mesh or plate with multiple apertures to produce a liquid aerosol. Some features are common to all these devices in which they generate aerosols with a high fine particle fraction [32], and they have a significantly higher efficiency of delivering drugs to the respiratory tract than do conventional jet or ultrasonic nebulizers [33]. The aerosol is generated as a fine mist and no internal baffling system is required. Moreover, they are portable, can be battery operated (operation with alternating current is optional with some of them), they efficiently aerosolize solutions and suspensions, and they have minimal residual volume of medication left in the device. Some of these devices are breath-actuated, thereby limiting release of aerosolized drug into the ambient air.

This section reviews several devices that deployed the new vibrating mesh (plate) technology, including Aerogen's aerosol generator, Omron's vibrating mesh technology, and ODEM's TouchSpray technology.

Aerogen's Aerosol Generator   Aerogen's aerosol generator consists of a vibrational element and a domed aperture plate, as shown in Figure 1.8. The ceramic vibrational element expands and contracts when electric signal is applied on it. The expansion and contraction produce an upward and downward movement in the domed plate. The aperture plate has up to 1,000 tapered holes, which are electroformed in a sheet. The wider portion of the

hole is towards the medication liquid and the narrower end is towards the atmosphere. The liquid is placed in a reservoir above the domed aperture plate. During operation, upward and downward movement (in several microns) of the aperture plate creates a micro-pumping action that extrudes the liquid through the holes to generate an aerosol. Particle size, flow, and fine particle fraction are influenced by the aperture exit diameter. The size of the holes in the aperture plate and the size of the aerosol particles can be modified for specific applications.
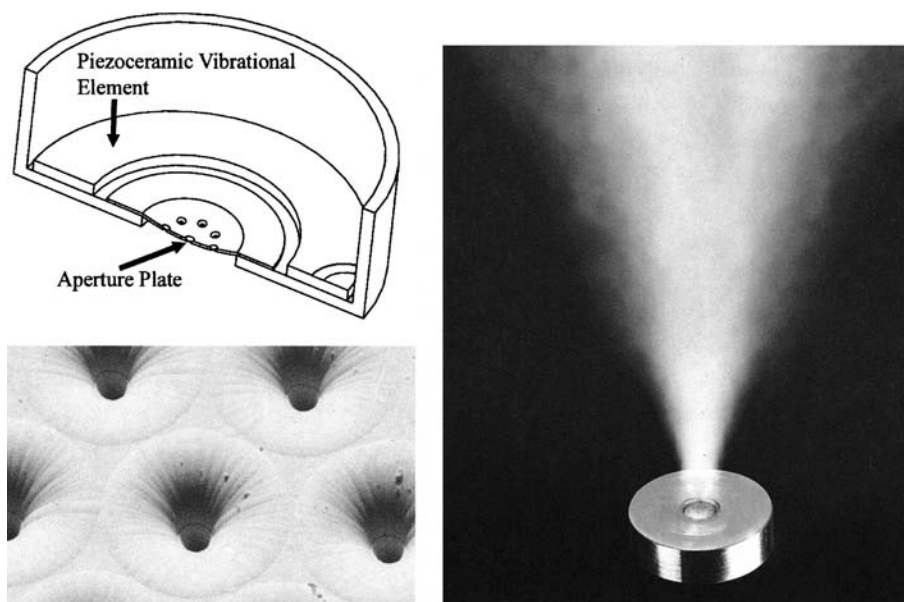
Figure 1.8   Components of Aerogen's aerosol generator. Top left: When the vibrational element is made to contract and expand by applying electric voltage, the up-and-down movement of the aperture plate creates a micro-pumping action that extrudes the liquid through the apertures. Bottom left: Microscopic view of the apertures on the plate. Right: a low-velocity mist is generated [34] .

The devices that incorporate the Aerogen aerosol generator can be battery operated. These nebulizers nebulize at 0.3-0.6ml/min, requiring less time for drug delivery than conventional ones. Also, the operation is quiet, and

moreover, the aerosol generator can aerosolize almost down to the very last drop of the liquid. Some of Aerogen's nebulizers are designed to operate in any orientation, including inverted. Aerogen's aerosol generator efficiently nebulizes suspensions, proteins, and peptides [33].

Omron's Vibrating Mesh Technology   The Omron's nebulizers (NE-U03 and NE-U22)incorporate a piezoelectric transducer that vibrates at a high frequency when electric voltage is applied (Figure 1.9(a)). The vibration of a piezoelectric ceramic disk is transmitted to a transducer horn that is in contact with the liquid to be aerosolized. Vibration of the transducer horn causes upward and downward motion of the mesh plate (Figure 1.9(b)), and the liquid passes through the apertures in the plate to form an aerosol. The mesh plate consists of numerous (up to 6,000) tapered holes, each approximately 3µm in diameter. These holes amplify the velocity of the liquid volumes in the horns and reduce the amount of power required to generate the aerosol. Using a high frequency vibration with a mesh plate containing numerous minute holes allows efficient generation of a fine particle mist.

The Omron devices are battery operated and can be AC powered too. They require no propellant or compressor and they can produce an aerosol in almost any orientation. Additionally, the energy required for nebulization is applied on the piezoelectric ceramic disk which is not in contacted with the medication liquid and hence temperature increase in the fluid is minimized, which eliminates the risk of chemical change in the liquid medications.

Omron's horn transducer based nebulizer is deemed as one of the best state-of-the-art techniques. It is the smallest in size and it is battery oper-
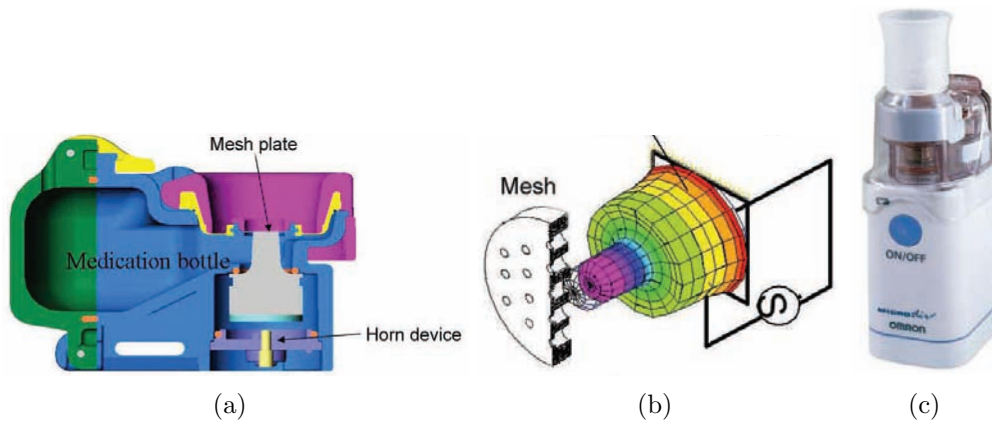
Figure 1.9 Omron's vibrating mesh technology. (a) The configuration. (b) The simulation of the working principle. (c) A photo of Omron's NE-U22 nebulizer.

ated. The piezoelectric ceramic driven transducer has a high working efficiency. The vibrating mesh makes the nebulization available in all directions and its medication bottle design leaves a small dead volume comparing with other products.

ODEM TouchSpray Technology The ODEM TouchSpray Inhaler devices are still under development in partnership with various pharmaceutical companies [33]. These devices are portable and simple to use. They have low power consumption and can be custom designed for specific clinical applications.

ODEM's TouchSpray technology employs a perforated membrane that vibrates at a high frequency against the body of liquid. The vibration source is a piezoelectric actuator, which is activated by a simple electronic drive circuit. The perforated membrane is a wafer-thin plate of stainless steel with many laser-drilled holes. The actuator and the perforated membrane

form the TouchSpray atomization head, which is in contact with the liquid to be aerosolized. Liquid jets are created as an inertial response to the vibration of the perforated membrane. Surface tension and hydrodynamic effects then cause these jets to break up to produce streams of precisely controlled droplets. This stream of liquid drops has a low velocity, and the atomization head can generate an aerosol in any orientation.

Summary Several electronic nebulizer devices that use a vibrating mesh or plate with multiple apertures to generate a fine-particle-size, low-velocity aerosol are now available. Figure 1.10 shows some commercial nebulizers on the market now. Because these devices nebulize at a faster rate than conventional jet or ultrasonic nebulizers, the duration of each nebulization process could be shortened. The nebulizers efficiently nebulize solutions and suspensions; they have been successfully used for aerosolizing insulin, other proteins and peptides, and fragments of DNA [33] and they have a negligible dead volume. Devices that use a vibrating mesh technology have overcome many of the limitations associated with the conventional jet or ultrasonic nebulizers, such as the bulky size, low efficiency and very high dead volume. With the devices using the new technology, clinicians are now able to precisely control drug delivery to patients' respiratory tract.

1.3 Project Objectives

Nebulizers are of great interest in some medical applications and this project aims to develop new piezoelectric transducers for nebulizers. Since the piezo-

(a) (b) (c) (d)

Figure 1.10   Photographs of some commercial mesh nebulizers that are currently available: (a) Aeroneb Go nebulizer (Nektar Therapeutics); (b) Aeroneb Pro nebulizer (Nektar Therapeutics); (c) Micro air NEU-22V (Omron Healthcare); and (d) eFlow rapid (Pari).

electric materials and the structure of the transducer are key elements for tailoring the device, the study on both of them will be conducted. The main objectives of the research project include:

1. To fabricate and characterize the state-of-the-art nebulizer transducers using lead-zirconate titanate (PZT) ceramics as the driving elements.

2. To use lead-free piezoelectric materials to fabricate transducers for neubulizers and compare their performance with the PZT-based transducer.

3. To design, model and fabricate a new type of nebulizer.

4. To characterize and evaluate the newly designed nebulizer prototype.

1.4   Outline of the Thesis

In this chapter, the theory of microdrop generation has been briefly introduced; the development of nebulizers and the state-of-the-art technologies have also been reviewed. The objectives of this research work and the original contributions of thesis are presented in this chapter too.

Following the introduction, the main body of the thesis is logically divided into six chapters. In Chapter 2, after briefly reviewing the fundamentals of piezoelectricity, the preparation process of the piezoelectric ceramics, both the PZT ones and two types of lead-free ceramics, has been presented. This process mainly includes three steps: dry pressing, heat treatment and poling.

Chapter 3 gives the characterization results of the piezoelectric ceramics and the transducers. The material properties are then calculated from the results using the *IEEE* resonance techniques. These data are required in the finite element analysis of Chapter 5.

The theoretical models of ultrasonic horns have been studied in Chapter 4. The longitudinal acoustic wave equations are used to derive the mechanical properties of a stepped horn. Different horn types have been compared and the stepped horn is regarded as the best one in displacement performance. The equivalent circuit of a stepped horn is studied too.

Chapter 5 is the finite element analysis of the horn transducer using a commercial software package ANSYS. Results for both the state-of-the-art solid stepped horn and the newly designed hollow horn are presented. The computed results show good agreements to the experimental results in Chapter 6.

Chapter 6 presents the displacement performance of the transducers. The performances are compared between the transducer with lead-free (BSZT) ceramic disk and the one with PZT ceramic disk. The lead-free ceramic stepped horn transducer shows displacement comparable with the PZT one.

In Chapter 7, the operations of the new nebulizer prototype are demonstrated and simple calculations are given to estimate the nebulization requirements.

As the last part of the thesis, Chapter 8 consists of the conclusion and suggestions for future work.

Chapter 2

Piezoelectricity and Piezoelectric Ceramic Preparation

2.1 Introduction

The functions and basic working principle of the stepped horn nebulizer have been briefly described in the previous chapter and it is noted that choosing the correct piezoelectric ceramic as the driving element is very important as it determines the transducer performance .

Piezoelectric materials find applications in a wide range of sensors, actuators and transducers in diverse fields including industrial process control, environmental monitoring, communications, information systems, and medical instrumentations. In detail, devices such as igniters, power generators, ultrasonic and acceleration sensors are based on the direct piezoelectric effect

whereas piezoelectric actuators, motors, printer heads, and ultrasonic vibrators are based on the converse piezoelectric effect. Other applications such as pulse-echo ultrasound transducers, piezoelectric transformers and active sonar transducers use both the direct and converse piezoelectric effects.

Commonly used piezoelectric materials include bulk ceramics, ceramic thin films, multilayer ceramics, single crystals, polymers and ceramic-polymer composites. For piezoceramic materials, it starts with barium titanate and later lead zirconate titanate (PZT) was introduced as a replacement. Because of the increased concern about the lead oxide toxicity, lead-free piezoelectric materials as an alternative to PZT have attracted much research attention, especially in bio-compatible or medical applications. While none of the presently available lead-free materials can match the overall performance of PZT [35], several classes of materials are now being considered as potentially attractive alternatives to PZT for special applications. These materials include the langasite family, $GaPO_4$, the well-known $LiNbO_3$, ZnO, AlN, and a number of other compositions [36].

In this project, both PZT and lead-free ceramics have been deployed in transducer devices.

2.2 Piezoelectricity

Piezoelectricity literally means "pressure generated electricity". It characterizes piezoelectric materials. The ability of certain crystalline materials which develop an electric charge proportional to a mechanical stress was discovered by J. and P. Curie in 1880. Soon it was realized that materials showing this

phenomenon must also show the converse effect with a geometric strain (deformation) proportional to an applied voltage. These properties are named as the direct and converse piezoelectric effects, respectively. Piezoelectricity could be found naturally in many monocrystalline materials such as quartz, tourmaline, topaz and Rochelle salt. Some man-made polycrystalline ceramic materials, such as lead zirconate titanate (PZT), barium titanate ($BaTiO_3$), lead titanate (PT), and lead metaniobate (PMN), can be processed to exhibit significant piezoelectric properties. Efficient conversion between mechanical and electrical energy and ease of production enable the piezoceramics to be widely used in electromechanical transducer designs.

2.2.1 Piezoelectric Ceramics

Materials exhibit piezoelectric properties have in common an asymmetric crystal structure. Piezoelectric ceramics such as PZT are perovskite ABO_3 crystals. As shown in Figure 2.1, each crystal is composed of a small, tetravalent metal ion (A) placed inside a face-centered cubic (FCC) lattice of larger divalent metal ions (B) and oxygen ions (O). Above a critical temperature, known as the "Curie temperature" (T_c), each perovskite crystal in the piezoelectric ceramics exhibits a simple cubic symmetry with no dipole moment, as demonstrated in Figure 2.1(a). However, if the temperature of the material is below the Curie temperature, each crystal has tetragonal symmetry and, associated with that, a dipole moment, as demonstrated in Figure 2.1(b). Adjacent dipoles which have the same direction form regions of local alignment called "domains". This alignment gives a net dipole moment to the

(a) Above T_c.   (b) Below T_c.
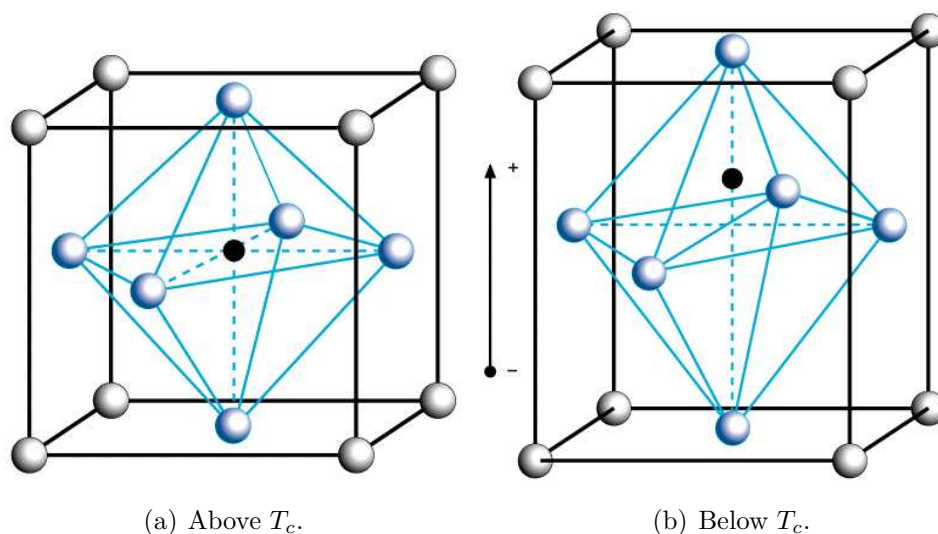
Figure 2.1   The Perovskite crystal structure ABO_3 (Grey atoms: A, Black: B, Blue: O).

domain, and thus a net polarization. As shown in Figure 2.2(a), the directions of polarization among domains is random. Subsequently, the whole ceramic element has no overall polarization.

By exposing the piezoceramic element to a strong electric field, the domains in the element are aligned, oriented with the electrical field (Figure 2.2(b)). This process is called "poling". When the electric field is removed, most of the dipoles are locked into a configuration of near alignment (Figure 2.2(c)). The piezoceramic element then has a net, permanent polarization and becomes anisotropic. An elongation of the element along the poling electric field also happens, usually within the micrometer range.

Properties of a poled piezoelectric ceramic element can be explained by the series of images in Figure 2.3. Mechanical compression or tension acted on the element changes the dipole moment associated with that element. This creates a voltage. Compression along the direction of polarization or

      (a)   (b)   (c)
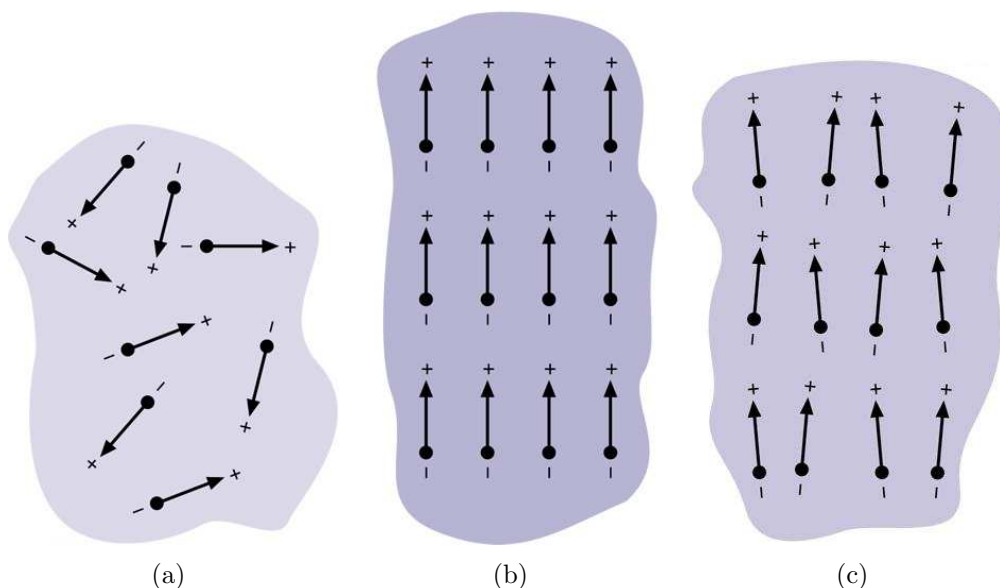
Figure 2.2   Poling process: (a) Prior to polarization polar domains are randomly oriented; (b) Polarization happens by applying a very large electric field; (c) A net polarization remains after the electric field is removed [37].

tension perpendicular to the direction of polarization generates voltage of the same polarity as the poling voltage (Figure 2.3(b)). Tension along the direction of polarization or compression perpendicular to that direction generates a voltage with polarity opposite to that of the poling voltage (Figure 2.3(c)). If a voltage of the same polarity as the poling voltage is applied to a ceramic element, in the direction of the poling voltage, the element will elongate and its diameter will decrease (Figure 2.3(d)). Conversely, if a voltage is applied opposite to the polarity of the poling voltage, the element will become shorter and broader (Figure 2.3(e)). If an alternating voltage is applied, the element will expand and contract cyclically, at the frequency of the driving voltage. When operated in this mode, the piezoelectric ceramic is used as an actuator, and electrical energy is converted into mechanical

energy. These two working modes have different applications. The actuating action is adapted to piezoelectric motors, sound or ultrasound generating devices, while the sensing action is used in fuel-igniting devices, solid state batteries, mechanical sensors and many other applications.

(a) (b) (c) (d) (e)
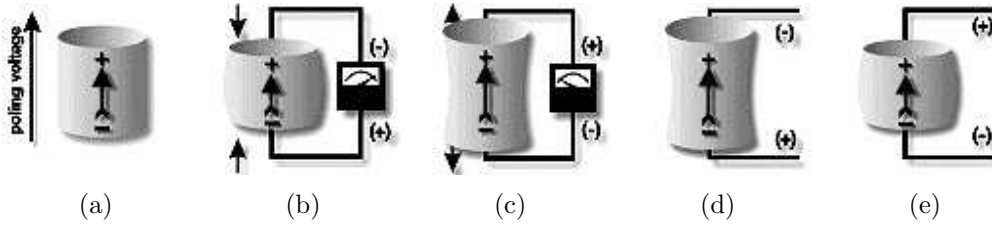
Figure 2.3   Piezoelectric properties: sensor and actuator actions of a poled piezo-ceramic element to applied stimuli [37].

2.2.2   Piezoelectric Constitutive Equations

The electromechanical coupling properties of piezoelectric materials could be described by a set of constitutive equations. These equations are based on the *IEEE standard on piezoelectricity* which assumes that piezoelectric materials are linear, and gives a good approximation at low electric field and low mechanical stress level. However, when the operating electric field or the mechanical stress level are high, the piezoelectric materials show considerable nonlinearity and their properties may deviate from the prediction.

The constitutive equations describe the "direct piezoelectric effect" and the "converse piezoelectric effect". They are based on the assumption that the total strain in the material is the sum of mechanical strain induced by the mechanical stress and the electric voltage caused strain by converse piezoelectric effect. Strain which is proportional to higher powers of the field,

such as the electrostrictive strain, is ignored. For convenience of writing, an matrix notation system is introduced: axes are identified by numerals rather than letters; 1, 2, 3 refer to the x, y and z axis respectively, and axis 3 is assigned to the direction of the initial poling (Figure 2.4).

Notation	Axis
1	x
2	y
3	z
4	Shear around x
5	Shear around y
6	Shear around z
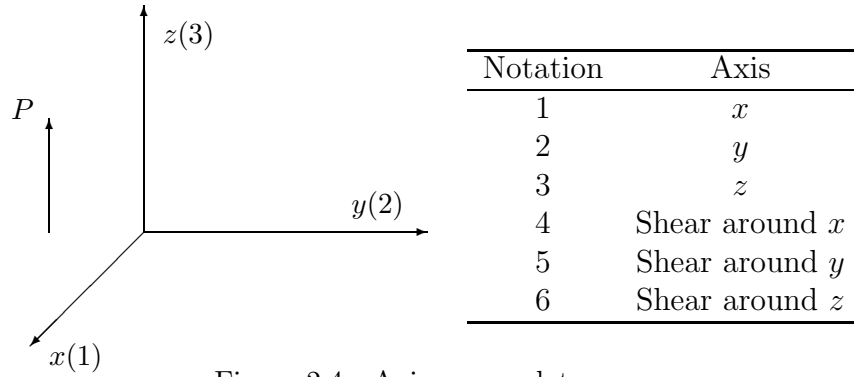
Figure 2.4   Axis nomenclature.

The constitutive equations can be written as:

$$\epsilon_i = S_{ij}^E \sigma_j + d_{mi} E_m \qquad (2.1)$$

$$D_m = d_{mi} \sigma_i + \xi_{ik}^\sigma E_k \qquad (2.2)$$

where the indices $i, j = 1, 2, ..., 6$ and $m, k = 1, 2, 3$ refer to different directions within the matrix notation system. The above equations are usually rewritten in the following form for sensing applications:

$$\epsilon_i = S_{ij}^E \sigma_j + g_{mi} D_m \qquad (2.3)$$

$$E_i = g_{mi} \sigma_i + \beta_{ik}^\sigma D_k \qquad (2.4)$$

where

σ $\cdots$ stress vector (N/m^2)

ϵ $\cdots$ strain vector (m/m)

E $\cdots$ vector of applied electric filed (V/m)

ξ $\cdots$ permittivity (F/m)

d $\cdots$ matrix of piezoelectric strain constants (m/V) or (C/N)

g $\cdots$ matrix of piezoelectric constants (m^2/C)

S $\cdots$ matrix of compliance coefficients (m^2/N)

D $\cdots$ vector of electric displacement (C/m^2)

β $\cdots$ impermittivity component (m/F)

and the superscripts D, E, and σ represent measurements taken at constant electric displacement, constant electric field, and constant stress.

Equations (2.2) and (2.4) express the direct piezoelectric effect, which describe the situation when the element is be used as an sensor. Equations (2.1) and (2.3) describe the converse piezoelectric effect, which deal with the case of actuating. The converse effect is often used to measure the piezoelectric coefficients.

2.3   Preparation of PZT Ceramics

Generally, to prepare a piezoelectric ceramic, fine powders of the component metal oxides are mixed in specific proportions. The mixed oxides are calcined to promote a solid state reaction among the oxides to form the required phase. The powder is then mixed with an organic binder and is formed into specific shapes, such as disks, rods, plates, etc. These elements are heated to a predetermined high temperature for a specific time. As a result

of this process the powder particles sinter and the material forms a dense crystalline structure. The elements are then cooled and, if needed, trimmed into required dimensions. Finally, electrodes are added to the appropriate surfaces of the ceramic element.

In this work, both lead-based and lead-free piezoelectric ceramics were used as the driving element of the stepped horn transducer which formed the major part of the nebulizer. Poled PZT APC-841 rings used in the hollow horn were supplied by APC International Ltd. PA, USA, and PZT PKI-402 powder, used in fabricating PZT disks and rings, was supplied by Piezo Kinetics, PA, USA. $BaCO_3$, $SrCO_3$, ZrO_2 and TiO_2 were used as raw materials for preparing lead-free piezoceramics.

Lead zirconate titanate (abbreviated as PZT) is the most widely used material in piezoelectric applications due to its good electromechanical coupling performance and stability. After doping with specific elements, piezoelectric properties of PZT ceramics may change significantly. There are various types of PZT ceramics in commercial products but each of them has its own properties which differ from others. PKI-402, 502, 552, and 802 are four typical commercial PZT ceramic products from Piezo Kinetic, USA. Table 2.1 lists several important properties of them.

PKI-402 which is equivalent to US Navy type I has a piezoelectric property of not very hard nor very soft. Good electromechanical coupling ability and stability made it widely used in transducer applications. In this work, PKI-402 has been chosen to fabricate disk and ring-shaped ceramic plates to be used as the driving elements of the transducer. The preparation includes the steps as given in the following sections.

Table 2.1   Properties of four types of PZT ceramics [38].

	ϵ_{33}^T	d_{33} (pC/N)	k_{33}	k_p	Q_m
PKI-402	1250	275	0.67	0.52	500
PKI-502	1800	400	0.69	0.60	80
PKI-552	3400	550	0.71	0.63	75
PKI-802	1000	220	0.61	0.51	900

2.3.1   Dry Pressing

Dry pressing is the first procedure of fabricating ceramic samples [39]. It is simply done by placing the as-supplied PZT ceramic powder into a metal mold, and then applying pressure to press the powder into a disk or ring shape. In this process. Lubricants ensure the ceramic powder being able to flow smoothly in the mold while applying pressure, and the binders provide strength to the compressed plates to maintain their shape before the heat treatments. For the PKI-402 powder supplied by Piezo Kinetic, the lubricants and binders are already included.

The weighed amount of PKI-402 powder was placed inside the cavity of a stainless steel mold. A torsional movement was applied to the rod inside the mode to make all powder uniformly distribute inside the mode and then a uniaxial pressure of 243MPa was applied for a few minutes. Excess air inside the mold was driven out and the ceramic power became well-packed disk or ring-shaped plates with the assistance of binders.

2.3.2 Binder Burnout, Calcination and Sintering

Heat treatment which contains three steps: binder burnout, calcination and sintering are essential procedures in ceramic sample preparation. It is usually processed in a computer-controlled furnace.

Organic binders, such as PVA should be removed; otherwise they may react with the lead oxide and yield undesirable compounds which may reduce the mechanical strength of the ceramic samples. The organic binders within the sample could be burnt out at around 550°C. During this step, the samples were placed on an alumina plate for the evaporation of the binders and other impurities and the temperature of 550°C was kept for one hour. The binder burnout schedule is shown in Figure 2.5.
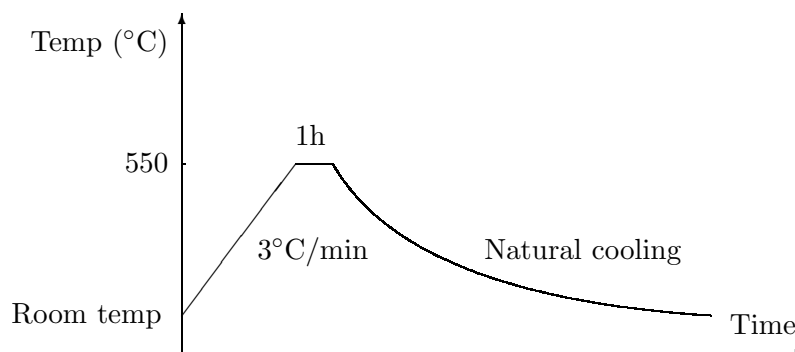
Figure 2.5   Temperature profile of the binder burnout process.

Calcination is a high temperature reaction in which various solid-state material components react to form a new material. It is the second step of the heat treatment. Sintering which is the final step of heat treatment is carried out to densify the ceramics. After sintering, the pores among powder particles become smaller and more spherical in shape [40], and the properties of the sample can be enhanced. Since the temperatures during

calcination and sintering are high enough to make lead evaporate (lead starts to evaporate at temperature above 888°C), the samples should be insulated from the atmosphere to prevent excessive loss of the lead content. Samples were placed on an alumina plate and covered by sintered ceramic powder of same ingredients to reduce the lead loss, as shown in Figure 2.6. The

Figure 2.6   Photograph of the configuration used in calcination and sintering.

calcination and sintering time of PKI-402 PZT were both set as two hours to complete the reaction and grain growth and the temperature were set as 850°C and 1350°C, respectively. After sintering, the furnace was turned off to allow the samples to cool naturally. The samples were taken out at room temperature. The temperature-time profile of calcination and sintering is demonstrated in Figure 2.7.
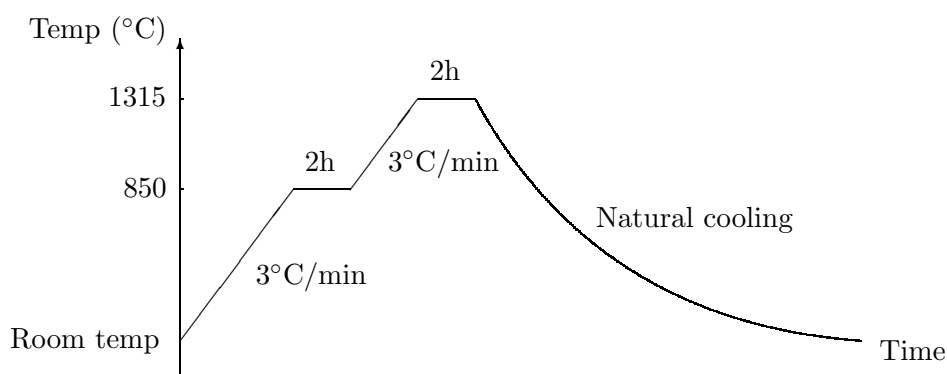
Figure 2.7   Temperature profile of calcination and sintering process.

2.3.3   Poling

After heat treatments, the surfaces of the samples were rough because the ceramics had shrunk in the sintering process. Thus, polishing is needed before adding electrodes to the samples. The ceramics were polished in wet condition with fine silicon carbide abrasive papers. The plates must be uniform in thickness, or they would possibly break down during poling due to the nonuniform electric field distribution caused by variation in thickness. In addition, the non-uniform thickness may adversely affect the performance of the ceramic disks (or rings) in both thickness and radial modes. Silver paste was applied to the two parallel surfaces of the sample disks (or rings) when they had been polished. After fired at 650°C the silver electrodes were affixed firmly on the sample surfaces.

The ceramics do not possess any piezoelectric properties before they are poled. As mentioned in Section 2.2.1, a high electric field is required to align domains to nearly the same direction, and the net polarization remains after the voltage has been removed. This process is called "poling". For different

materials, the poling condition differs: hard piezoelectric ceramics may need higher poling fields and/or longer poling time. The poling field of a material can be estimated from its hysteresis loop while the poling time and poling temperature can be optimized by a set of tests. The poling condition of PKI-402 PZT ceramic is summarized in Table 2.2. The sample was mounted

Table 2.2   Poling condition of PKI-402 PZT ceramic.

Material	Poling field (MV/m)	Temperature (°C)	Time (min)
PKI-402	3.00	120	30

on a holder with electrodes and placed into a silicone oil bath for a stable insulating environment. The oil bath was heated to the poling temperature and was kept constant during the poling process. The applied poling voltage, V_{poling} can be calculated by: $V_{poling} = E_{poling} \times t$, where E_{poling} is the poling field of the sample material and t is the thickness of the disk (or ring). The voltage was increased slowly until the poling voltage V_{poling} has been reached and the voltage was kept for a designated time (the poling time). After that, the silicone oil bath was cooled down. During cooling, the voltage was kept constant until the system cooled to room temperature. The leakage current of the whole process was monitored in order to ensure the stability of the system under the high electric field. The poling system is illustrated in Figure 2.8.

After poling, surface charges generated on the surface of the sample were removed by short-circuit annealing. The poled sample was wrapped in a aluminum foil and placed inside a programmable oven (Memmert, Germany)
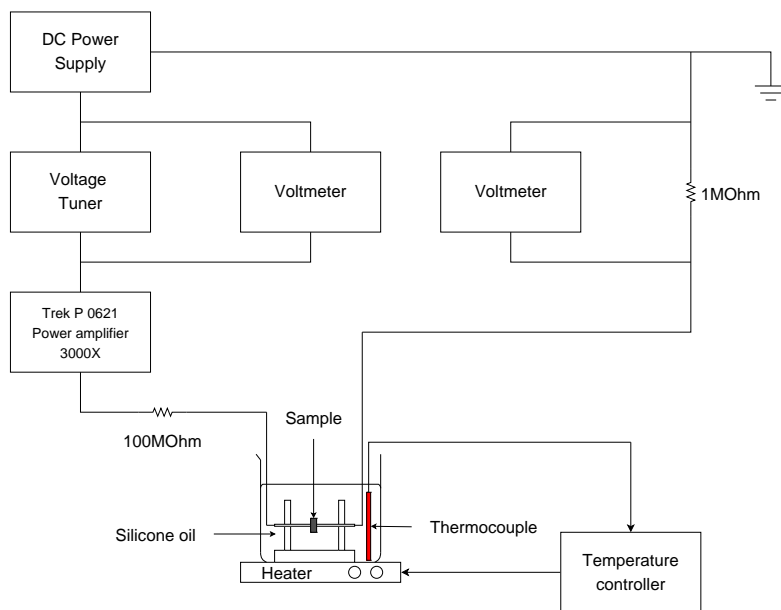
Figure 2.8   Schematic diagram of the DC poling system for bulk ceramics.

at 40°C for 8 hours. The moderate temperature enhanced the charge mobility and enabled the space charges trapped inside the sample escape easily. Several finished ceramic disks and rings are shown in Figure 2.9.

Figure 2.9   Photograph of piezoelectric ceramic samples.

2.4 Preparation of Lead-free Ceramics

2.4.1 Preparation of BSZT Disks

PZT has long been deemed as an ideal driving element for transducer designs because of its superior piezoelectric performance and stability. However, PZT contains more than 60 weight per cent of lead [35], the concerns regarding toxicity of lead has limited its further applications in commercial products, especially in some medical devices. Thus, lead-free piezoelectric materials have attracted much attention. Although there has been a concerted effort to develop lead-free piezoelectric ceramics, no complete alternative to PZT has yet been found. However, in some aspects, lead-free piezoceramics is competent. In this work, the lead-free material, strontium and zirconium doped barium titanate (BSZT) is chosen. BSZT has a good piezoelectric coefficient ($d_{33} \sim 200\mathrm{pC/N}$), and more importantly, it has a much lighter density and thus a lower acoustic impedance. The similar acoustic impedance with titanium made the transmit wave much less reflected at the interface between BSZT and titanium transducer. Therefore, a better match in acoustic impedance may increase the performance of the device.

The general fabrication procedure of BSZT is not different from that of PZT. However, before dry pressing, a step of powder preparation is required, since the formula is not commercially available. The strontium and zirconium doped barium titanate with the formula of $Ba_{0.95}Ti_{0.95}Sr_{0.05}Zr_{0.05}O_3$, is a solid solution of barium titanate ($BaTiO_3$) and strontium zirconate ($SrZrO_3$). A conventional mixed oxide technique was used to prepare the BSZT ceramics. Reagent grade $BaCO_3$, $SrCO_3$, ZrO_2 and TiO_2 were used as the raw materi-

als. They were weighed according to the ratio of $0.95(BaTiO_3)-0.05(SrZrO_3)$. The powder was ball-milled for 10h in ethanol using zirconia balls. Calcination was conducted at $1100°C$ for 10h. After calcination, the mixture was dried and added with PVA as binder for granulation. The granulated powder was pressed into disk-shaped plates. The disks were sintered at $1500°C$ for 5h in air. The sintered disks were polished to dimensions of 10.0mm in diameter and 1.0mm in thickness. Silver paste was fired on both surfaces of the disk at $650°C$ as electrodes. The samples were poled in silicone oil at room temperature under an electric field of 2kV/mm for 20min.

2.4.2   Preparation of KNN Rings

As our nebulizer is based on a piezoelectric transducer which is designed to work at its resonance frequency to obtain large displacements, the working current might be large and the heat generation is considerable. To avoid the degradation of the material properties against the high temperature, harder type of piezoceramics is preferred, and hence, a hard type lead-free ceramic $(Na_{0.5}K_{0.5})NbO_3$ (KNN) has been chosen.

Raw materials include potassium carbonate (K_2CO_3), sodium carbonate (Na_2CO_3) and niobium pentoxide (Nb_2O_5). They were weighed according to their mole ratio 1: 1: 2. The conventional mixed oxide technique was used to prepare the ceramics. The raw materials were ball milled in ethanol using zirconia balls and then dried at $80°C$. Binders (PVA) were added and a steel pressing mould was used for dry pressing the mixture powders into ring-shaped plates. After the binder burnout process at $550°C$, calcination

and sintering were processed at 880°C and 1110°C for four hours respectively. After the ceramic rings cooled down and have been electroded by firing the silver paste on their two plane surfaces, they were poled in the thickness directions. The poling condition was 180°C in silicone oil for 30min and with an applied electric field of 4kV/mm. Finally, the rings were packed in an aluminum foil and placed in a 45°C oven overnight to short-circuit anneal the samples and get rid of the surface charges.

Chapter 3

Characterization of Materials and Devices

3.1 Introduction

While designing the piezoelectric transducer, questions like: what kind of piezoelectric ceramics should be used and how to determine the optimum configuration of the device are always posted. To answer these questions, thorough studies of the material properties are required, because the material properties have critical influence on the design. Therefore, the characterization of the materials is an essential part of this work. After being fabricated, the piezoelectric ceramics are characterized with their densities, electrical properties, and piezoelectric properties. The density measurement used the Archimedes' principle and the piezoelectric properties were characterized with *IEEE* resonance techniques [41]. These property data are used in the finite element analysis (Chapter 5).

After the transducer prototypes have been developed, the electrical properties of the transducers are also measured to determine their resonance frequencies.

3.2   Material Characterization

3.2.1   Density Measurement

The measurement of density is important in evaluating the quality of a material. If the density of the material is low compared with its theoretical value, the performance of such material degrades. Also, the density value of a material is important in the acoustic calculations. Defects such as pores and impurities affect the density of a piezoelectric ceramic and the fabrication conditions such as the sintering and calcination temperatures have influence on it too: defects and lower sintering temperature cause the decrease in the ceramic density.

Density is a commonly used physical quantity and there are many ways to measure it. In this work, the measurement is based on the Archimedes' principle using an electronic balance. The measured parameters are the mass of a sample (m_0) and the mass of the sample completely immersed in water (m_1). With these two value, the density of the sample can be calculated by:

$$\rho = \frac{m_0}{m_0 - m_1} \cdot \rho_{water} \tag{3.1}$$

where ρ is the density of the sample and ρ_{water} is the density of water which equals 1000kg/m^3. The calculated results are listed in the following sections.

3.2.2 Relative Permittivity Measurement

For a parallel plate capacitor in free space or air, the capacitance C is given by:

$$C_0 = \frac{Q}{V} = \frac{\epsilon_0 \cdot A}{t} \tag{3.2}$$

where ϵ_0 is the permittivity of free space , A is the area of the conducting plate and t is the distance between the two plates.

Piezoelectric materials studied in this project belong to dielectric materials, which contain randomly oriented dipole molecules. When an external field is applied across the material, the dipoles aligns parallel the the external field and an internal electric field is formed. The internal electric field reduces the overall electric field and potential. Referring to Equation (3.2), when the electric potential decreases, the capacitance increases. The capacitance of a dielectric material filled parallel plate capacitor is:

$$C = \frac{\epsilon \cdot A}{t} \tag{3.3}$$

where ϵ is the permittivity of the dielectric material. Comparing ϵ with ϵ_0 (the permittivity of free space), the relative permittivity is defined:

$$\epsilon_r = \frac{\epsilon}{\epsilon_0} \tag{3.4}$$

Since dielectric loss exists in the dielectric materials, ϵ_r is a complex value:

$$\epsilon_r = \epsilon' - i\epsilon'' \tag{3.5}$$

$$\tan\delta = \frac{\epsilon''}{\epsilon'} \tag{3.6}$$

where ϵ' is the real permittivity, ϵ'' is the dielectric loss and $\tan\delta$ is the loss tangent.

In a ferroelectric material, a Curie temperature exists, at which the material undergoes a phase transition from a non-polar state to a polar state (the lower temperature side). The phase transition can be of the first order or second order. The relative permittivity of the material usually increases with rising temperatures because of the increasing spontaneous polarization, and reaches the maximum value at the Curie point. After the peak, the relative permittivity decreases again.

Besides the temperature dependence, the dielectric properties are also frequency dependent. Usually, with increasing frequency, the relative permittivity of a material decreases while the loss tangent increases. This phenomenon is explained by the deformation of domains inside the material. At lower frequencies, the piezoelectric deformation can follow the periodic change of the the applied AC field and then the dielectric properties are measured under a "mechanically free" state. If the frequency of applied AC field increases and exceeds the mechanical resonance frequency of the material, the material is "mechanically clamped", which means the periodic piezoelectric deformations cannot catch up with the AC field and the deformation are thus reduced gradually by the inertial effect.

In this chapter, the capacitance of the piezoelectric ceramic samples was measured by an impedance analyzer and the relative permittivity was calculated from Equation (3.4). The temperature dependence of the relative permittivity is not involved in this study since the temperature change in our device is not expected to be very high.

3.2.3 Piezoelectric Coefficient Measurement

In the *direct* piezoelectric effect, the induced charge is proportional to the force and in the *converse* piezoelectric effect, the applied electric field produces a proportional strain. For both effects, the proportionality constant is the piezoelectric constant d which is numerically identical for both direct and converse effect:

$$d = D/T = S/E \qquad (3.7)$$

where D is the dielectric displacement (the area density of charge Q), T is the stress, S is the strain, and E is the applied electric field. Therefore, d can be expressed in two units according to the different definitions: C/N for direct effect and m/V for the converse effect.

The piezoelectric d coefficient relates closely to the mechanical displacement. To identify directions in a piezoelectric material, three axes (1, 2, 3) are used, these axes are analogous to x, y, and z of the Cartesian coordinate. The 3-axis is parallel to the direction of polarization of the material (Figure 2.4). The first subscript i of d_{ij} represents the direction of polarization and the latter subscript j represents the direction of response such as the induced strain or a mechanical stress.

Among the d coefficients, only d_{33} were directly measured, and the other d coefficients were calculated according to *IEEE standard on Piezoelectricity* in the following sections. The d_{33} coefficient was measured by a d_{33} meter (model no. ZJ-3B) supplied by the Institute of Acoustics Academica Sinica. The value of d_{33} can be read directly from the meter.

3.2.4   Resonance Characterization

Electromechanical Coupling Factor

Energy can be applied to a piezoelectric material body either by mechanically stressing it or by electrically charging it. The electromechanical coupling factor measures the square of the fraction of the mechanical energy converted to electrical energy in each cycle, or vice versa. The remainder is simply stored elastically or dielectrically during each cycle or dissipated.

The square of the coupling factor is not a measurement of efficiency. The power conversion efficiency of a transducer depends on an expression of the form $k^2/(k^2 + D)$, where D is the dissipation factor on the input side.

The electromechanical coupling factors are important material parameters for piezoelectric ceramics, and they depend on the degree of poling. They are dimensionless measures of the strength of the piezoelectric effects. The commonly used coupling factors are those derived from the equations of

state that use the d_{ij} coefficients. They are as following:

$$k_{15} = \frac{d_{15}}{\sqrt{s_{44}^E \epsilon_1^T}} \tag{3.8}$$

$$k_{33} = \frac{d_{33}}{\sqrt{s_{33}^E \epsilon_3^T}} \tag{3.9}$$

$$k_{31} = \frac{d_{31}}{\sqrt{s_{11}^E \epsilon_3^T}} \tag{3.10}$$

$$k_p = \frac{d_{31}}{\sqrt{2/(s_{11}^E + s_{12}^E)\epsilon_3^T}} = k_{31}\sqrt{2/(1-\sigma)} \tag{3.11}$$

where $\sigma = -s_{12}^E/s_{11}^E$ is the Poisson's cross-contraction ratio. The planar coupling factor k_p refers to the simultaneous application of equal stress along the 1 and 2 axes, which is equivalent to uniform radial tension or compression in the plane normal to the poling axis. Another coupling factor k_t, which relates to E_3 and strain S_3, but in the absence of other strains, need to be considered:

$$k_t = \frac{e_{33}}{\sqrt{\epsilon_3^S c_{33}^D}} \tag{3.12}$$

k_t refers to the coupling applied to longitudinal thickness vibrations of laterally clamped plates and c_{33} is a stiffness constant giving ratio of stress to strain in the 3 direction.

The coupling constants relate the open- and short-circuit elastic constants

in the form of:

$$s_{44}^D = s_{44}^E(1 - k_{15}^2) \tag{3.13}$$

$$s_{33}^D = s_{33}^E(1 - k_{33}^2) \tag{3.14}$$

$$s_{11}^D = s_{11}^E(1 - k_{31}^2) \tag{3.15}$$

$$s_{12}^D = s_{12}^E - k_{31}^2 s_{11}^E \tag{3.16}$$

$$s_{33}^E = s_{33}^D(1 - k_t^2) \tag{3.17}$$

Resonance Method

Measurements of resonance and antiresonance frequencies of a piezoelectric material sample can be used to evaluate piezoelectric effects. Elastic bodies show numerous resonance; the most pronounced are those where the body can just accommodate one half wavelength of a standing elastic wave. The piezoelectric effect is a convenient way to excite such elastic waves to permit observation of the interaction of the mechanical resonance with the electric behavior. This is best seen in the equivalent circuit idealized for a single resonance. The equivalent circuit of a piezoelectric sample near a fundamental resonance is shown in Figure 3.1. The values of L and C_1 are those that at the resonance frequency f_r the impedances $2\pi f_r L$ and $-1/2\pi f_r C_1$ are opposite in sign and equal in magnitude, and the total impedance of this branch is given only by the mechanical resistance R, which is comparatively quite small. This mechanical branch is parallel with the electric capacitance C_0. At the frequency of minimum impedance or the resonance, f_r, the standing wave in the piezoelectric body is under a zero-field condition. For applied
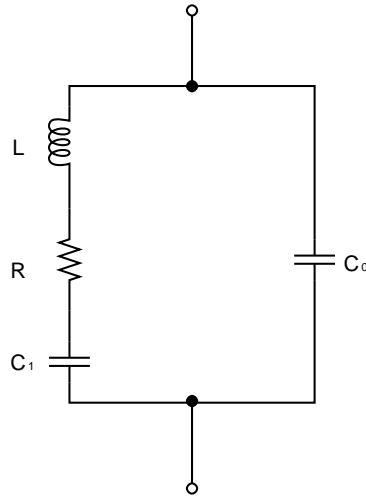
Figure 3.1   Equivalent circuit of a piezoelectric body near one of its fundamental resonance frequencies.

frequencies above f_r the mechanical branch becomes inductive. When the series impedance of this branch becomes opposite and equal to the impedance of C_0, the impedance of the sample reaches a maximum since opposite currents flow in the two branches. This condition of parallel resonance, however, means constant charge on the sample. The frequency of maximum impedance or antiresonance f_a, is therefore that of a standing wave under open-circuit conditions. The relation between fundamental resonance and antiresonance frequency and elastic compliance is given by:

$$2 f_r \cdot l = \frac{1}{\sqrt{\rho s^E}} \tag{3.18}$$

$$2 f_a \cdot l = \frac{1}{\sqrt{\rho s^D}} \tag{3.19}$$

where l is the controlling dimension and ρ is the density. Since s^E and s^D is related by coupling factor k, the f_a and f_r can be related:

$$\frac{f_a^2 - f_r^2}{f_a^2} = p\frac{s^E - s^D}{s^E} = pk^2 = \frac{C_1}{C_0 + C_1} \qquad (3.20)$$

A dimensionless shape factor p is inserted because nonuniform amplitude distribution at resonance makes both the short-circuit or the open-circuit condition imperfect. The influence of the series resistance R has been disregarded.

Impedance Spectrum

The impedance spectrum over frequency is measured by an impedance/gain-Phase analyzer (model no. HP 4194A).

Figure 3.2 shows the impedance spectrum of a 10mm diameter 1mm thick PZT disk over 0 - 3MHz. There are two fundamental modes in the spectrum: the radial mode and the thickness mode. As indicated in the figure, the fundamental radial mode is at about 200kHz, and the thickness mode is above 2MHz. Several weak peaks between the two intense peaks can be seen too; they are recognized as the higher order harmonic modes of the fundamental radial mode. From this figure, the thickness mode contains several small peaks, they are induced from the coupling of the thickness mode and the harmonic radial modes. As for our transducer, the resonance of the fundamental radial mode is of the most interests. The resonance frequency of the radial mode is at 225kHz.

Figure 3.3 is the impedance spectrum of the 10mm diameter 1mm thick

lead-free ceramic (BSZT) disk over the frequency range of 0 - 3MHz. This spectrum is similar to that of PZT disk, except for the difference in peak locations. The resonance frequency of the fundamental radial mode locates at 290kHz for the BSZT disk.
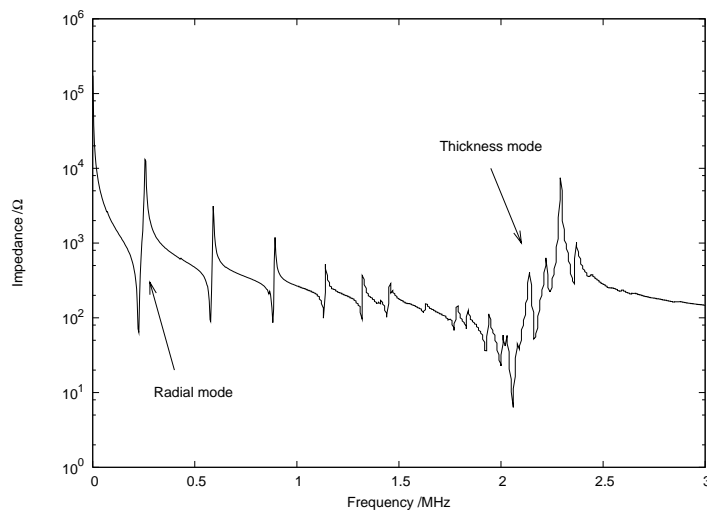
Figure 3.2   The impedance spectrum of a PZT disk with a diameter of 10mm and thickness of 1mm.
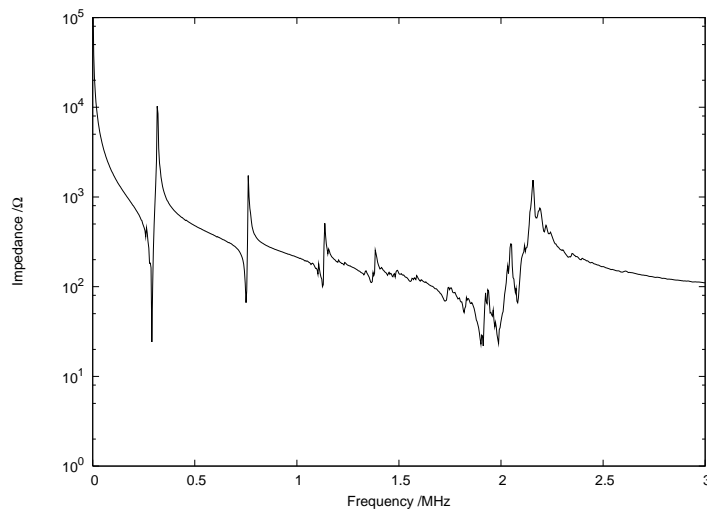
Figure 3.3   The impedance spectrum of a BSZT disk with a diameter of 10mm and thickness of 1mm.

Figure 3.4 is the impedance spectrum of a PZT ring. The ring has an outer diameter of 12.7mm, inner diameter of 0.5mm and the thickness of 1.0mm. Different from the spectrum of disks, there are three fundamental modes: the radial mode, the wall thickness mode and the thickness mode. These three modes are indicated in this figure respectively.
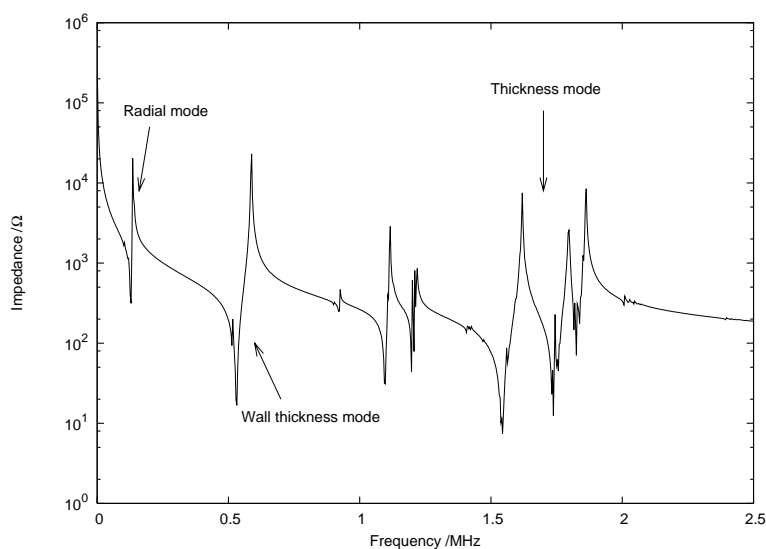
Figure 3.4   The impedance spectrum of a PZT ring with inner diameter of 5mm, outer diameter of 12.7mm and thickness of 1.0mm.

Figure 3.5 gives the spectrum of the KNN lead-free ceramic ring which has the same dimensions as the PZT ring. The resonance frequency of the radial mode is about 201kHz.

Summary of Material Properties

From reading the impedance spectrum, the resonance and antiresonance frequencies could be found. According to the *IEEE standard on Piezoelectricity* the parameters of materials can be calculated. Some important properties of PZT, BSZT and KNN are summarized in Table 3.1.
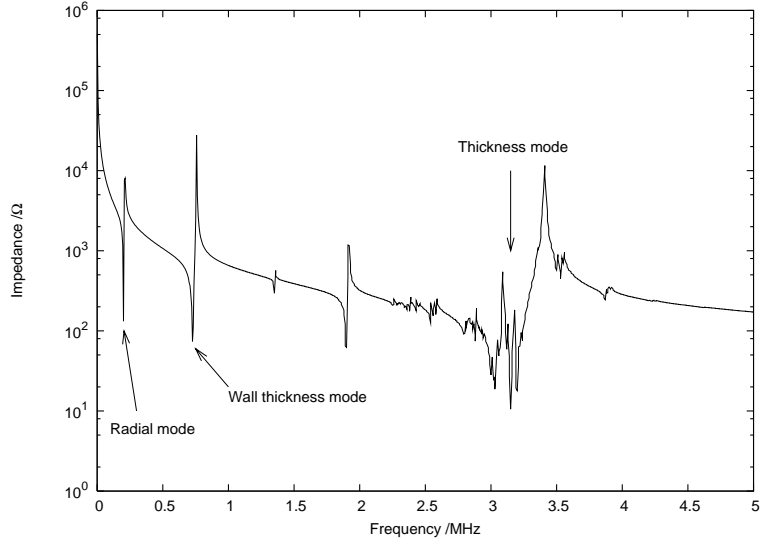
Figure 3.5   The impedance spectrum of a KNN lead-free ceramic ring with inner
diameter of 5mm, outer diameter of 12.7mm and thickness of 1.0mm.

Table 3.1   Properties of the piezoceramics used in this work.

Parameter	Unit	PZT	BSZT	KNN
ϵ_{11}^S	-	1730	404	279
ϵ_{33}^S	-	1700	684	295
d_{33}	pC/N	374	200	92
d_{31}	pC/N	-171	-98	-32
d_{15}	pC/N	584	240	110
ρ	kg/m^3	7750	5800	4650
k_t	-	0.47	0.49	0.47
k_p	-	0.52	0.49	0.40
Q_M	-	500	250	800
Z_a	MRayl	30.9	25.3	32

3.3   The Horn Transducers

As reviewed in Chapter 1, vibrating mesh technology has been used in some state-of-art devices to generate aerosols. They have great advantages over the conventional nebulizers. In Omron's nebulizer NE-U22 (see Figure 1.9 in Chapter 1), a stepped horn transducer driven by a PZT disk "beats" the alloy mesh at a high frequency, to cause the mesh vibrating. The pros and cons of the device are both obvious. The stepped horn has a large vibration displacement and can easily be driven by battery operated circuit; on the other hand, the liquid directly contacts with the horn's surface, a sealing structure, which dampens the vibration of the horn, must be added to keep the medication. Also the different natural frequency of the mesh and the liquid between the horn and mesh both lower the driving efficiency of the horn transducer. Additionally the dead volume is also large comparing with other technologies and the lead-base piezoceramics are not suitable for medical device applications.

In our new nebulizer design, the vibration of the mesh is also generated by a stepped horn. The new feature is, we drilled a hole along the symmetric axis at the center of the horn. The mesh is capped on the small end of the horn and the rear end of the hole is connected to a pipe. A piezoelectric ring is used as the driving element instead of the disk because of the unique construction. Liquid from the pipe flows through the hollow horn and is kept by the mesh, thus no sealing part is required. Since the mesh is fixed on the horn and vibrates together with it, the driving efficiency is much higher than the contact structure. Furthermore, the dimensions of the device can

be greatly reduced because the reservoir is detached from the horn.

The horns are machined from a titanium rod with different geometries. Figure 3.6 shows the geometry of the solid horn. The hollow horn are designed with larger diameters due to the center hole. The geometry of a hollow horn is shown in Figure 3.7. The horns were bonded with the piezoelectric disk (or ring) using an epoxy resin (Eccobond 45LV black). Hot curing is processed at 45°C for 8 hours or at 60°C for 4 hours.

We started the study of the horn transducers with the solid horn transducers. The electrical impedance is measure by the impedance analyzer (HP 4194A) and the spectrum over frequency are recorded. Figure 3.8 is the impedance spectrum of the solid horn transducer driving by a PZT disk. Since the piezoelectric disk is bonded firmly with the stepped horn, the disk vibrates together with the horn and their modes are coupled. A very sharp resonance peak near 180kHz has been pointed by an arrow in the figure. It is determined as the working mode of the transducer. This working mode is also described by finite element analysis in Chapter 5 and by experiments in Chapter 6.

Figure 3.9 shows the impedance spectrum of a solid horn transducer with a BSZT lead-free ceramic disk. The resonance frequency of its working mode is also about 180kHz, since this frequency is mainly determined by the total length of the transducer which is the sum of the length of the horn plus the thickness of the disk (see Chapter 4).

The new hollow horns with piezoelectric ceramic rings as the driving elements have also been measured of their impedance over frequency. The impedance spectrum of the hollow horn with a PZT ceramic ring is shown in
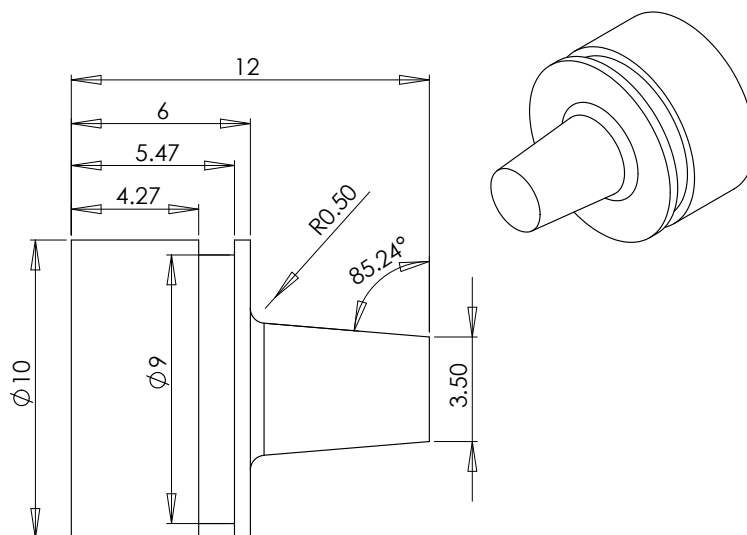
Figure 3.6   The geometry of the solid horn.
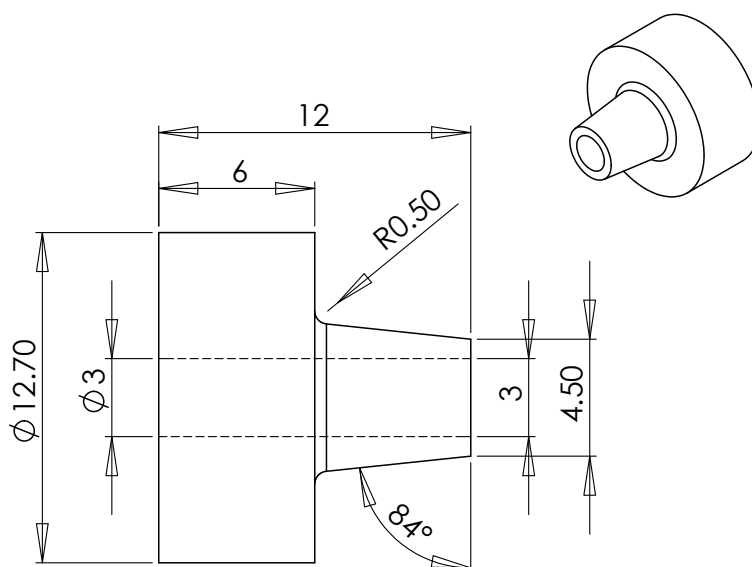
Figure 3.7   The geometry of the hollow horn.
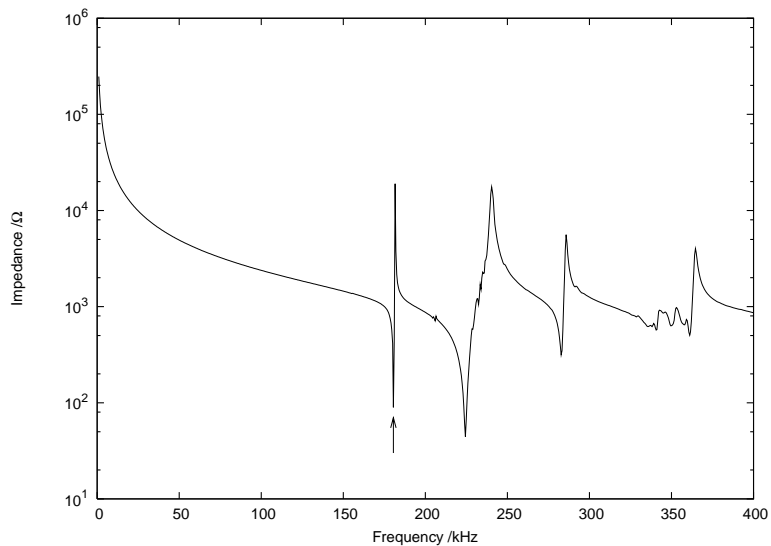
Figure 3.8   The impedance spectrum of the solid horn transducer with a PZT disk.
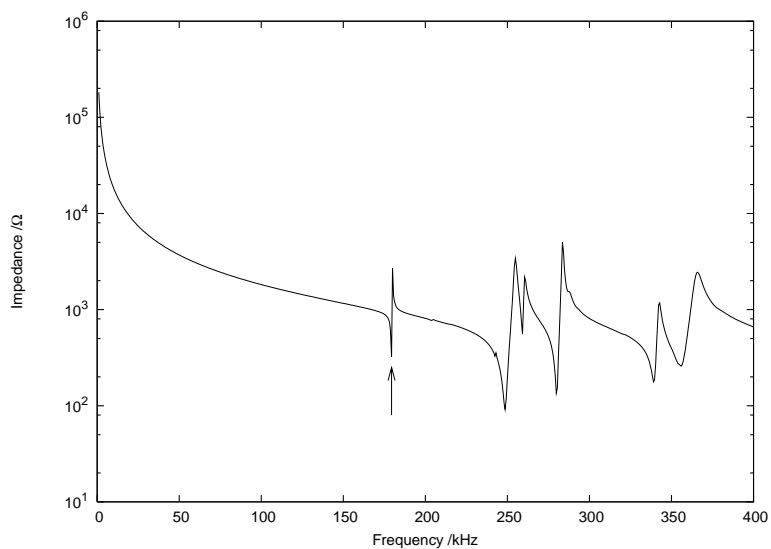
Figure 3.9   The impedance spectrum of the solid horn transducer with a BSZT lead-free disk.

Figure 3.10 and the one of the hollow horn with a KNN lead-free ceramic ring is shown in Figure 3.11. The impedance spectrum is more complex than the solid horn's, because the piezoelectric ring has more resonance modes than the disk at low frequencies. These modes are coupling with the horn hence more peaks can be observed. Additionally, the inner diameter of the ring is larger than the diameter of the center hole on the horn (space is reserved for the connecting pipe used in the nebulizer application), and the geometry difference also made the coupling more complicated. The FEM simulation in Chapter (5) describes the deformation of the transducer of each mode and extracts the ones that could be used as the working mode of the nebulizer. Those results show that the hollow horn with a PZT ring has one working mode at about 185kHz while the hollow horn with a KNN ring has two, at 165kHz and 198kHz, respectively. (These modes are pointed by an arrow in Figure 3.10 and 3.11) This difference comes from the coupling between the horn and the ring. The difference in material properties of the two ceramic rings induced different coupling states.
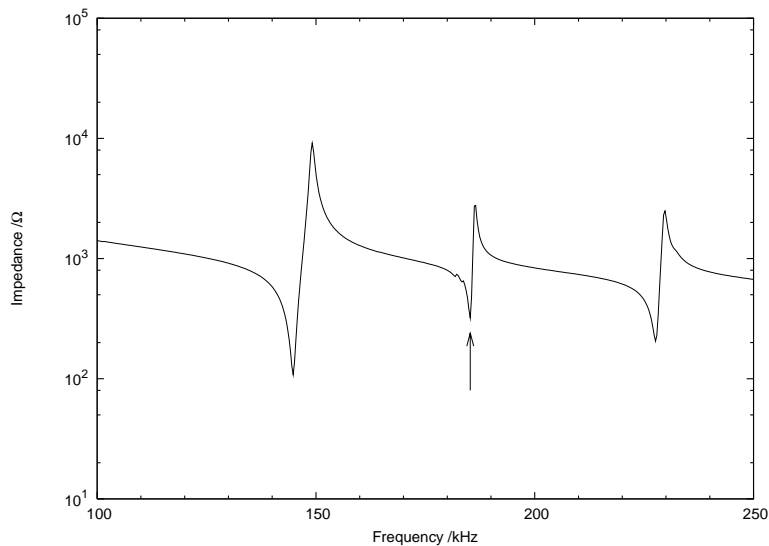
Figure 3.10   The impedance spectrum of the hollow horn transducer with a PZT ceramic ring.
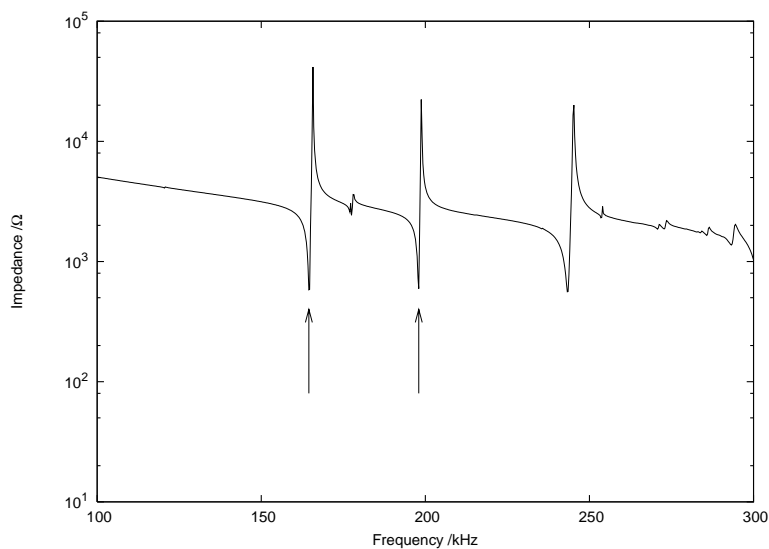
Figure 3.11   The impedance spectrum of the hollow horn transducer with a KNN lead-free ceramic ring.

Chapter 4

Stepped Horns and Wave Motions in Stepped Horns

4.1 Introduction

In Chapter 2, piezoelectric ceramic rings and disks, including PZT, lead-free BSZT and KNN, have been fabricated. They can be used as driving elements in transducers. When AC voltages are applied to them, the disks or rings generate mechanical vibrations. The values of the piezoelectric constant d_{33} or d_{31} of the piezoelectric ceramics, they all, including the lead-based and the lead-free ones, are all in the order of 10^{-10} in the unit of C/N. In other words, when a 100V DC voltage is applied on a ceramic sample, the converse piezoelectric effect induced deformation is less than 0.01μm. A bulk ceramic with such a tiny deformation under DC driving could hardly be used in any device applications directly, but the deformation of the piezoelectric ceramics is significantly enhanced near their resonance frequencies.

Furthermore, in transducer designs, acoustic or ultrasonic horns are usually used to amplify the strain induced by the driving elements. In this work, for producing ultrasonic vibration, a stepped horn structure excited by the radial mode of a piezoelectric ring or disk has been adopted. The titanium stepped horn transforms and amplifies the radial deformation of the ceramic ring or disk into an axial vibration at the horn tip. Comparing with other horn structures, the amplification of a stepped horn is the highest. In the following sections, horn structures and wave motion in a stepped horn are briefly described.

4.2   Longitudinal Wave Motions

A sharp, localized disturbance in a medium will transmit or spread to other parts of the medium in the mode known as wave propagation. Waves in different forms can propagate in gas, liquid, and solid media. The wave propagation in solids can be divided into three categories: elastic wave which happens in elastic materials where Hooke's law is obeyed, elastic wave in which the yield stress of the media material has been exceeded, and the viscoelastic waves where viscous as well as elastic stress acts. In this chapter, the study of stepped horn transducer is based on an elastic assumption. This approximation makes the problems simple and describes the real case accurately (for the solid titanium stepped horn structure).

4.2.1   Longitudinal Wave in a Free Rod

In mathematical equations, the longitudinal wave motion in a cylindrical rod is similar to a transverse wave motion of a tense string, but physically they are different: when a longitudinal wave moves along a rod, the displacement of particles of the rod is in the direction of the wave propagation.

Consider a uniform rod which is parallel to x, as shown in Figure 4.1. The shape of the cross-section is arbitrary and the material is isotropic. If the plane cross-sections stay plane, the particle motion is permitted only parallel to the x axis. Hence, the displacement of each section can be expressed by $u(x, t)$, where t is the time variable. When the longitudinal wave propagates
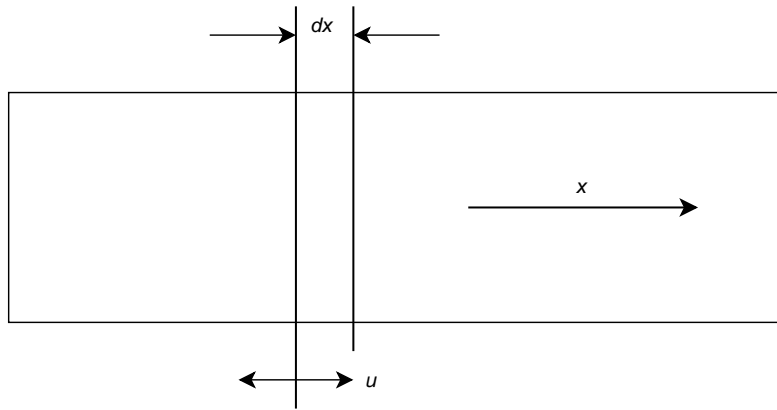
Figure 4.1   A rod with coordinate x and displacement u.

in the rod, the rod has a dynamically varying stress field $T(x, t)$. If we introduce an expression of $q(x, t)$ to indicate the body force of any unit volume in the rod, the motion in the $+x$ direction is described as:

$$-TA + (T + \frac{\partial T}{\partial x}dx)A + qAdx = \rho Adx\frac{\partial^2 u}{\partial t^2} \tag{4.1}$$

where A is the cross section area of the rod. Since A remains constant along the axis x, the equation could be rewritten as:

$$\frac{\partial T}{\partial x} + q = \rho \frac{\partial^2 u}{\partial t^2} \tag{4.2}$$

By applying Hooke's law:

$$T = ES \tag{4.3}$$

and the definition of strain:

$$S = \frac{\partial u}{\partial x} \tag{4.4}$$

where E is the Young's modulus and S is the axial strain, we have:

$$\frac{\partial^2 u}{\partial x^2} + \frac{q}{E} = \frac{\rho}{E} \frac{\partial^2 u}{\partial t^2} \tag{4.5}$$

If we neglect the lateral inertial effects which are associated with the perpendicular contraction and expansion, the body force $q(x,t)$ is omitted. Equation (4.5) becomes:

$$\frac{\partial^2 u}{\partial x^2} = \frac{\rho}{E} \frac{\partial^2 u}{\partial t^2} = \frac{1}{v_l^2} \frac{\partial^2 u}{\partial t^2} \tag{4.6}$$

where $v_l = \sqrt{E/\rho}$. Equation (4.6) is known as the wave equation. The velocity v_l is often designated as the bar velocity.

The partial differential equation (4.6) has a solution in the form of:

$$u(x,t) = \sum_{n=1}^{\infty} [A_n \cos(\omega_n t) + B_n \sin(\omega_n t)][C_n \cos(\beta_n x) + D_n \sin(\beta_n x)] \tag{4.7}$$

where $\beta_n^2 = \omega_n^2/v_l^2$. For a free rod with length l, the boundary conditions are:

$$E\frac{\partial u(0,t)}{\partial x} = E\frac{\partial u(l,t)}{\partial x} = 0 \tag{4.8}$$

By substituting Equation (4.7) into Equation (4.8), we have:

$$\sin(\beta l) = 0 \quad \beta l = n\pi \quad n = 0, 1, 2, ... \tag{4.9}$$

Thus, the natural frequencies are:

$$\omega_n = \frac{n\pi v_l}{l} \tag{4.10}$$

or

$$f_n = \frac{nv_l}{2l} \tag{4.11}$$

The normal modes for the first three natural frequencies of the longitudinal wave in a free rod are plotted in Figure 4.2. The vertical coordinate refers to the longitudinal displacement and the arrows give the direction of the motion of particles.

As showing in the next section, Equations (4.10) and (4.11) are also suitable for stepped horns consisting of two rods with same length, e.g. our stepped horn transducers. In our case, l is the total length of the horn (12mm) and v_l is the acoustic speed in titanium, which is 4580m/s. Therefore, the natural frequency of the fundamental resonance mode ($n = 1$) of
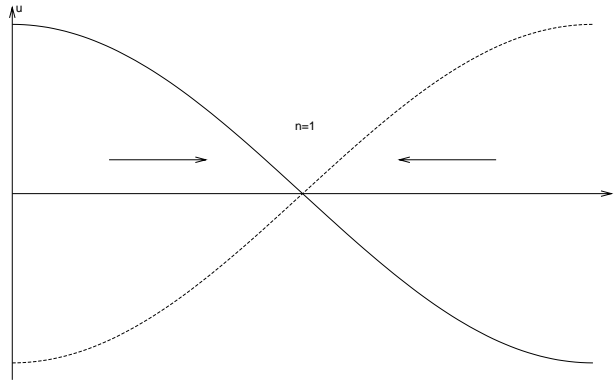
(a) n=1
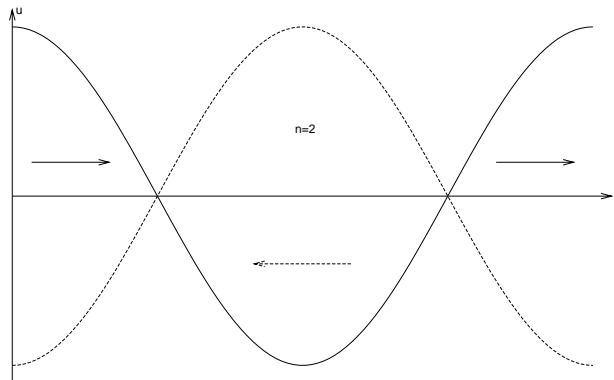
(b) n=2
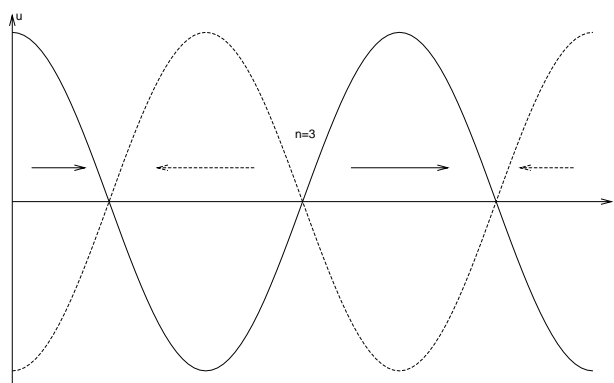
(c) n=3

Figure 4.2   The first three modes of longitudinal wave in a free rod.

our horn is obtained:

$$f_{nat} = \frac{nv_l}{2l} = \frac{4580\text{m/s}}{2 \times 12\text{mm}} = 190.83\text{kHz} \tag{4.12}$$

This calculated frequency is higher than the experimental operating frequency, since the total length increases when a piezoelectric ceramic element is attached to the rear end of the horn. In fact, problems such as "the two sections of the horn are no longer having the same length" and "the two materials have different sound speeds" are also brought in by adding the piezoelectric ceramic elements. The analytical calculation becomes very difficult and hence computational tools are required to solve these problems. In Chapter 5, finite element method is used to calculate the resonance frequencies.

4.2.2   Longitudinal Wave in a Stepped Horn

A stepped horn, in the simplest form, consists of two cylindrical rods of different diameters placed end to end concentrically. As shown in Figure 4.3, the two cylinders are different in length (l_1 and l_2), cross section area (A_1 and A_2), and elastic modulus (E_1 and E_2). By applying the wave equation (Equation (4.6)) to each cylindrical rod:

$$\frac{\partial^2 u_1}{\partial x_1^2} = \frac{1}{v_1^2}\frac{\partial^2 u_1}{\partial t^2} \tag{4.13}$$

$$\frac{\partial^2 u_2}{\partial x_2^2} = \frac{1}{v_2^2}\frac{\partial^2 u_2}{\partial t^2} \tag{4.14}$$
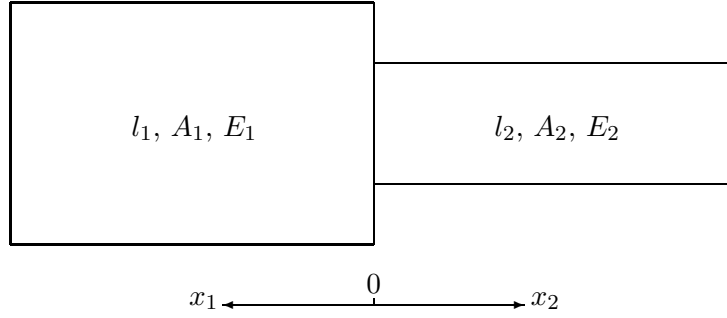
Figure 4.3 A stepped horn in its simplest form.

The harmonic solutions can be written as:

$$U_1 = A \sin(\beta_1 x_1) + B \cos(\beta_1 x_1) \tag{4.15}$$

$$U_2 = C \sin(\beta_2 x_2) + D \cos(\beta_2 x_2) \tag{4.16}$$

where $\beta_i = \omega/v_i$ and $v_i = \sqrt{E_i/\rho_i}$, $i = 1, 2$.

The boundary conditions are:

$$\left. \frac{dU_1}{dx_1} \right|_{x_1=l_1} = 0 \tag{4.17}$$

$$\left. \frac{dU_2}{dx_2} \right|_{x_2=l_2} = 0 \tag{4.18}$$

$$-U_1|_{x_1=0} = U_2|_{x_2=0} \tag{4.19}$$

$$E_1 A_1 \left. \frac{dU_1}{dx1} \right|_{x_1=0} = E_2 A_2 \left. \frac{dU_2}{dx2} \right|_{x_2=0} \tag{4.20}$$

Among them, Equations (4.19) and (4.20), the boundary conditions at the junction face $x_1 = x_2 = 0$, express the continuity of displacement and force.

Applying these conditions into the solutions (4.15) and (4.16) gives:

$$A \cos \beta_1 l_1 - B \sin \beta_1 l_1 = 0 \tag{4.21}$$

$$C \cos \beta_2 l_2 - D \sin \beta_2 l_2 = 0 \tag{4.22}$$

$$B = -D \tag{4.23}$$

$$E_1 A_1 A \beta_1 = E_2 A_2 C \beta_2 \tag{4.24}$$

Combining the above four equations, we have:

$$\begin{pmatrix} \cos \beta_1 l_1 & -\sin \beta_1 l_1 \\ \frac{E_1 A_1 \beta_1}{E_2 A_2 \beta_2} \cos \beta_2 l_2 & \sin \beta_2 l_2 \end{pmatrix} \begin{pmatrix} A \\ B \end{pmatrix} = \begin{pmatrix} 0 \\ 0 \end{pmatrix} \tag{4.25}$$

In order to have a solution, the determinant of coefficients must be vanished, hence, the following frequency equation could be obtained:

$$\frac{E_1 A_1 \beta_1}{E_2 A_2 \beta_2} \cos \beta_2 l_2 \sin \beta_1 l_1 + \sin \beta_2 l_2 \cos \beta_1 l_1 = 0 \tag{4.26}$$

This equation is general and could be used to numerically solve problems for given material and geometry parameters. For most common cases, the two rods in the stepped horn are of the same material, so $E_1 = E_2$ and $\beta_1 = \beta_2 = \beta$. Hence, Equation (4.26) could be simplified and be rewritten as:

$$\frac{A_1}{A_2} \cos \beta l_2 \sin \beta l_1 + \sin \beta l_2 \cos \beta l_1 = 0 \tag{4.27}$$

or

$$\frac{A_2}{A_1} \sin \beta l_2 \cos \beta l_1 + \cos \beta l_2 \sin \beta l_1 = 0 \tag{4.28}$$

Equation (4.28) is known as the frequency equation for the stepped horn. By using the equation, the design curve of a stepped horn could be plotted. In Figure 4.4, the x, y axis represents βl_1 and βl_2 respectively. Different curves refer to different area ratios. Curves of A_1/A_2=1, 2, 4, 6.25 are plotted in Figure 4.4 ($A_1/A_2 = 6.25$ is the area ratio of the stepped horn used in our experiments). From this design curve, we chose the point of $\beta l_1 = \beta l_2$ on it to set our horn transducers, as the maximum magnification factor is achieved at $\beta l_1 = \beta l_2$, i.e. $l_1 = l_2 = l/2$ (see the next section).
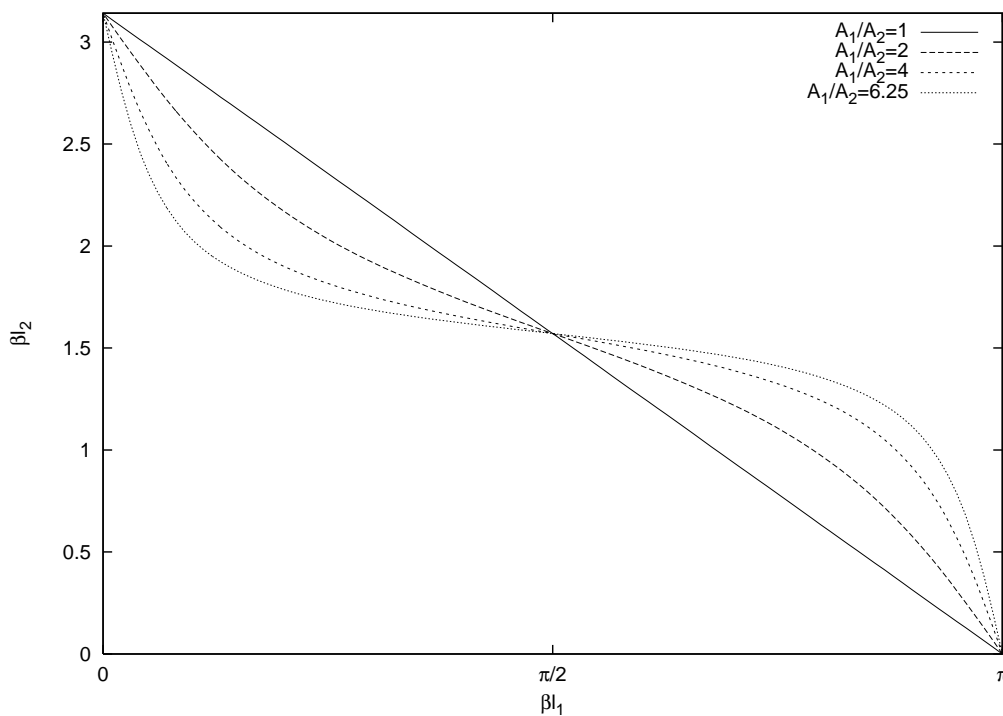
Figure 4.4   Design curves for calculating the lengths.

4.3   Mechanical Properties of a Stepped Horn

Ultrasonic horns are usually used to mechanically amplify vibrations produced by magnetostrictive and piezoelectric elements. Standard horn designs have changed very little since their inception. Referred to the degree to which the area changes from the base to the tip, there are generally four designs: constant, linear, exponential and stepped [42], as shown in Figure 4.5. Among these four types, stepped horn is apparently the most efficacious
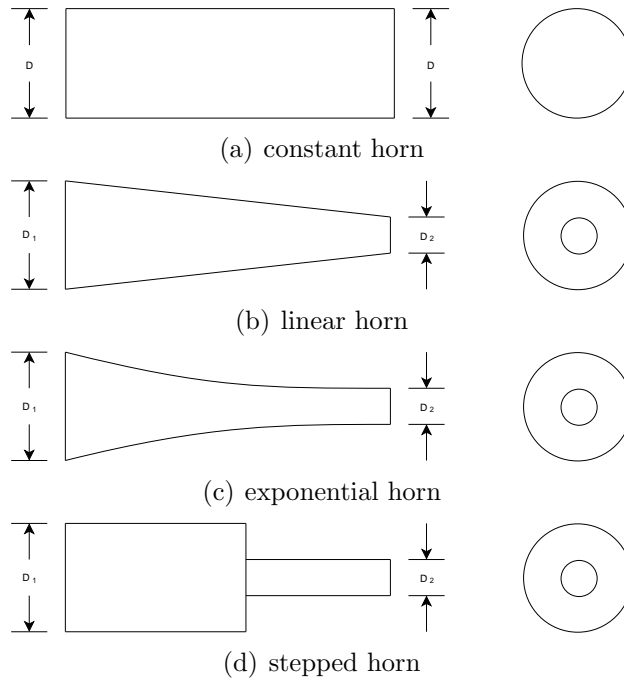
Figure 4.5   Four basic shapes of standard horns [42].

in mechanical amplification. The displacement magnification and other mechanical properties of the stepped horn are studied in this section.

4.3.1 Displacement Magnification

The magnification in displacement of a stepped horn is defined as the ratio of the displacements of the two ends of the horn, i. e. $M = u_2(l_2, t)/u_1(l_1, t)$ in Equations (4.13) and (4.14). Substituting the solution, Equations (4.15) and (4.16) into the definition, there is:

$$
\begin{aligned}
M &= \frac{C \sin \beta l_2 + D \cos \beta l_2}{A \sin \beta l_1 + B \cos \beta l_1} = \frac{C \sin \beta l_2 + (C \frac{\cos \beta l_2}{\sin \beta l_2}) \cos \beta l_2}{A \sin \beta l_1 + (A \frac{\cos \beta l_1}{\sin \beta l_1}) \cos \beta l_1} \\
&= \frac{C}{A} \frac{\sin \beta l_1}{\sin \beta l_2} = \frac{E A_1 \beta}{E A_2 \beta} \frac{\sin \beta l_1}{\sin \beta l_2} = \frac{A_1}{A_2} \frac{\sin \beta l_1}{\sin \beta l_2}
\end{aligned}
\tag{4.29}
$$

Combining the frequency equation (4.28) which confines l_1 and l_2 and the magnification equation (4.29), the maximum value of M could be obtained:

$$
M_{max} = \frac{A_1}{A_2}
\tag{4.30}
$$

Figure 4.6 gives the relationship between M (magnification) and βl_1 (the step position) with different area ratios A_1/A_2, while Figure 4.7 shows the normalized magnification versus the position of the step. The maximum values of the curves were found at $\beta l_1 = \pi/2$. From Equation (4.28) or Figure 4.4, we get: $\beta l_2 = \beta l_1 = \pi/2$, or $l_1 = l_2 = l/2$. It means that the maximum magnification can be obtained when the step of the stepped horn is placed in the middle of the total length. This result gives the geometrical definition in the stepped horn designing. In our horn design, as we set $l_1 = l_2 = l/2$, the maximum magnification could be reached: $M_{max} = A_1/A_2 = 6.25$.

One thing should be noted: if we extend the x axis of Figure 4.7, more
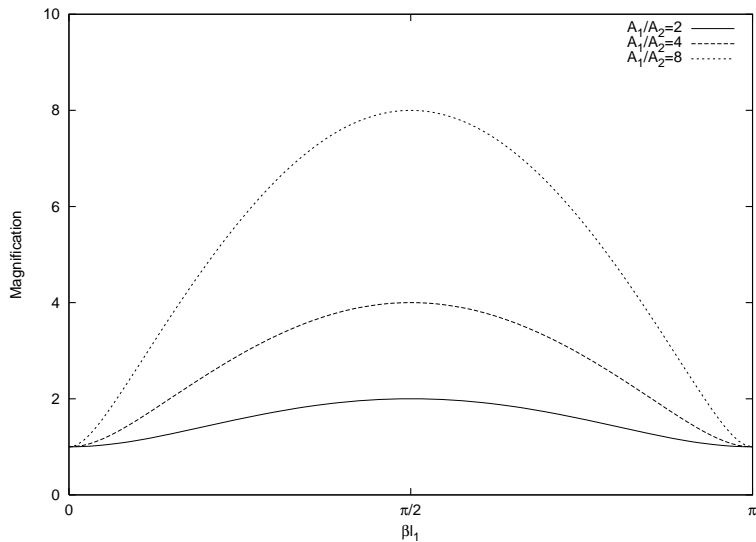
Figure 4.6   Relation between magnification and step position with different area ratios.
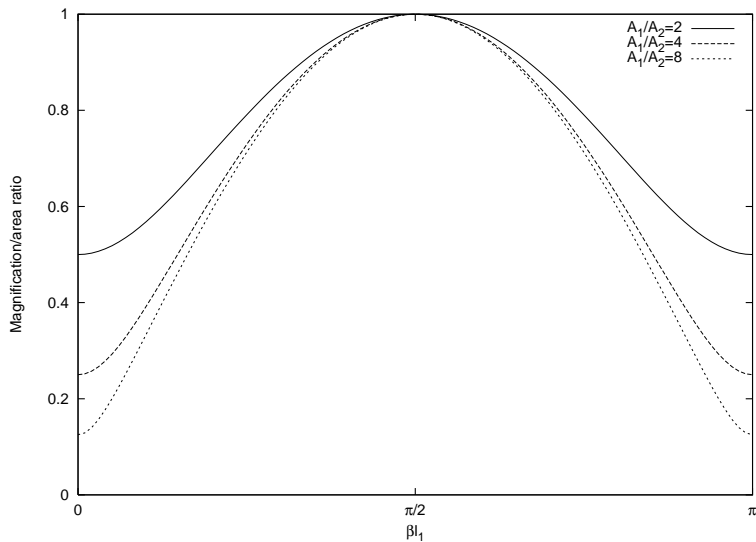
Figure 4.7   Normalized magnification versus step position with different area ratios.

maximum values of M could be discovered. And by the same method, the relations between βl_1 and βl_2 at these points could be obtained by solving Equation (4.28) or by reading Figure 4.4 . In fact, the maximum magnification can be found at these places where l_1 and l_2 satisfy the following equation:

$$\frac{l_1}{l_1 + l_2} = \frac{2m - 1}{2n} \quad m = 1, 2, \cdots, n \qquad (4.31)$$

where n is the overtone order and $m = 1, 2, \cdots, n$.

Table 4.1 lists the maximum magnifications of four types of horns, namely constant, linear, exponential, and stepped horn. Clearly, stepped horn has the superior amplification ability. Hence, the stepped horn structure was chosen and deployed in our traducers.

Table 4.1   Maximum magnification of the four types of horns.

Horn Type	Constant	Linear	Exponential	Stepped
Max Magnification	1	4.61	$\sqrt{A_1/A_2}$	A_1/A_2

4.3.2   Q Factor

Q factor of a device is defined as the ratio of energy stored to energy dissipated per working cycle. For aluminum stepped horns, the Q value usually exceeds $25,000$ while the value of Q factor for aluminum solid is only $10,000$ [43]. The mechanism of dissipation and Q depend not only on the material but also on the geometry of configuration and modes of vibration. Stored energy depends on configuration and modes through the equivalent mass and compliance parameters and the Q factor varies appreciably with

level or drive [43], even at low levels, where most measurements were carried out. This is probably because of the higher stress occurring at the step of the horns.

4.3.3   The Stress Problem

There is one problem inherent in all horns if they are working as mechanical amplifiers: high stress sets up when large amplification is achieved. Especially in the case of a stepped horn, the maximum magnification $M = A_1/A_2$ is obtained only when the step is placed at the nodal points. Positions of these points are given by Equation (4.31): $l_1/l = (2m - 1)/2n$, where n is the overtone order and $m = 1, 2, \cdots, n$. At resonance, the nodal points are under the greatest stress. If high amplitude of motion are required, it is necessary to move the high stress to a larger cross-section and take the loss in magnification or to reinforce the stress area by means of fillets or flanges.

With the concern about the high stress, in our stepped horn transducer, the structure has been slightly modified: the thiner cylinder part in the stepped horn has been changed into a cone-shape, and a fillet of 0.5mm radius has been added to weaken the stress concentration.

Chapter 5

Finite Element Analysis of the Horn Transducer

5.1 Introduction

The mathematical analysis in Chapter 4 gives a simple but useful model of the stepped horn. It describes the wave transitions in the horn and predicts some general characteristics, such as resonance frequencies and displacement/stress distributions. However, because of the complexities of the modified structure in our device and the coupling fields, the theoretical calculation becomes inaccurate or extremely difficult. Fortunately, with the highly improved computers and computational techniques nowadays, ways of obtaining these design information or parameters have been developed. Finite element methods form one of the most versatile class of such methods. Designers can obtain more information with deeper insights of the behaviors of the design which can hardly be given by the theoretical models and

76

mathematical or matrix calculations.

In this chapter, backgrounds and principles of the finite element method and typically the formulation of piezoelectric structures are reviewed. A commercial finite element software package, ANSYS, is used to perform the modal analysis of the device. The computed results will be compared with the experimental ones whenever they are available. Emphasis is putting on the deformation of the stepped horn which is essential to the nebulizer.

5.2 Finite Element Analysis

5.2.1 Fundamentals of Finite Element Analysis

Finite Element Methods (FEM) or Finite Element Analysis (FEA) is a numerical simulating solution to practical problems in engineering. It mathematically describes, or predicts the physical behavior of an actual engineering structure by constructing the structure as a virtual object or model and solving the complex partial differential equations [44]. The main advantage of FEA is that it is suitable for practical engineering problems with complex structures: they may have arbitrary shapes, loads, geometries, boundary conditions and material properties. The main features are [45]:

- The entire solution domain is divided into small finite segments (hence the name 'finite elements').

- Over each element, the behavior is described by the displacement or stress of the element.

- All elements are assembled together and the requirements of continuity and equilibrium are satisfied between neighboring elements.

- Provided that the boundary conditions of the actual problem are satisfied, a unique solution can be obtained to the overall system of linear algebraic equations.

- The solution matrix is sparsely populated, i.e. with relatively few nonzero coefficients.

Finite element analysis does not give a formula solution. The simulation is only an approximation unless the structure is so simple that a convenient exact formula is available. To obtain good accuracy in the solution set, a large number of small elements must be used. A simple description of FEM could be like that: it first meshes the structure into several discrete regions or pieces called elements, and each element is described by the material law in a simple way. The elements are reconnected together at a finite numbers of points called nodes to hold the elements together. The shapes and number of the used elements are determined by the structure shape, geometries and the required accuracy of the solution (Figure 5.1(b), 5.1(d)). The analysis process always results in thousands of simultaneous algebraic equations which require powerful computers and good algorithm to solve.

A more sophisticated description of FEA regards it as a piecewise polynomial interpolation. For each element, a field quantity (displacement or stress field in structural analysis) is interpolated from values of the field quantity at nodes. By connecting elements together, the field quantity becomes interpolated over the entire structure in piecewise fashion by polynomial expressions

(a)

(b)

(c)

(d)
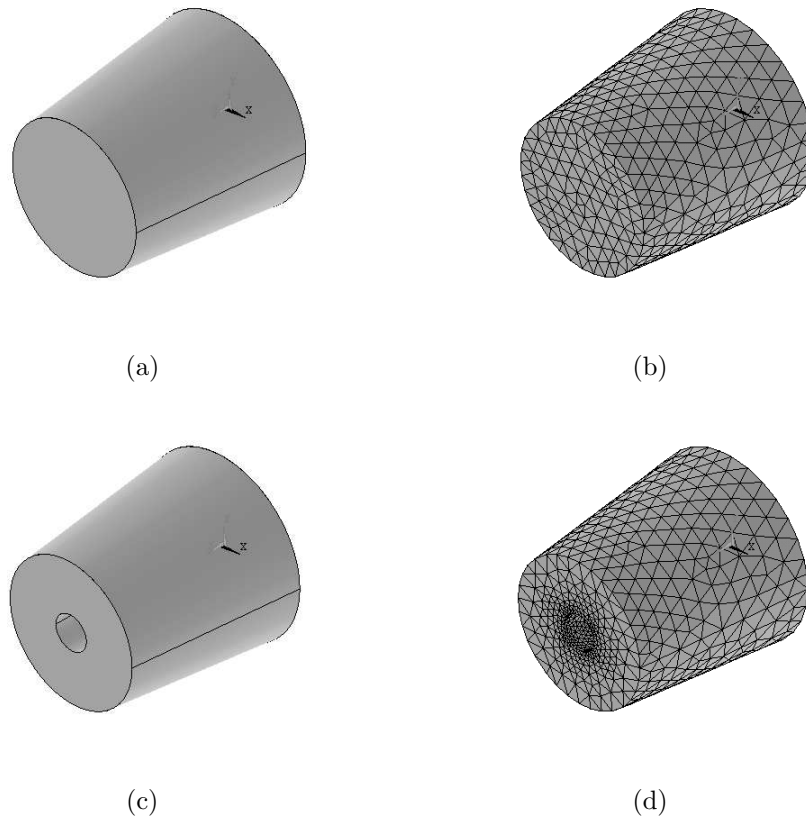
Figure 5.1 Schematic diagrams of (a) a 3D solid cone-shaped structure; (b) mesh of (a) with finite element methods; (c) a 3D cone-shaped structure with a center hole; (d) mesh of (c) with finite element methods.

of these elements. At an equilibrium state, the values of the field quantity at nodes are those which lead to a minimization of the total potential energy (*TPE*). According to these extreme values of energy functions, a set of simultaneous algebraic equations for the field quantity at the nodes could be acquired. If the force-displacement relationship (such as the stiffness, mass and damping matrices) for each of these discrete structural elements is known, then the force-displacement relationship for the entire structure can be assembled using standard matrix methods. Results of greatest interest

are usually peak values of the field quantities or their gradients.

5.2.2 Finite Element Formulation for Piezoelectric Structures

The piezoelectric finite element formulation is based on the variational principle based on the concept of virtual work [46]. It has been widely used in finite element softwares including ANSYS [47]. A thoroughly understanding of the basis is a necessity to use the FEM tool appropriately.

The piezoelectric constitutive equations for a linear material behavior with more than one degree of freedom can be expressed in matrix form:

$$\{T\} = [c]\{S\} - [e]\{E\} \tag{5.1a}$$

$$\{D\} = [e]^T\{S\} + [\varepsilon]\{E\} \tag{5.1b}$$

where $\{T\}$ is the mechanical stress vector, $\{S\}$ is the mechanical strain vector, $\{D\}$ is the electric displacement vector, $\{E\}$ is the electric field vector, $[c]$ is the elastic stiffness matrix evaluated at a constant electric field, $[e]$ is the piezoelectric matrix, and $[\varepsilon]$ is the permittivity matrix evaluated at constant mechanical strain. All the electrical quantities are one tensorial rank lower than the corresponding mechanical quantities. Additionally, for each element, Newton's laws of motion and Maxwell's equation in charge and potential relations must be considered.

By using the variational principle, the internal and external electrical and

mechanical energies can be equated in matrix notation:

$$
\iiint_V \big\{ \{\delta S\}^T[c]\{S\} - \{\delta S\}^T[e]\{E\} - \{\delta E\}^T[e]^T\{S\} - \{\delta E\}^T[\varepsilon]\{E\}
$$

$$
- \{\delta u\}^T\{\bar{F}\} + \rho\{\delta u\}^T\{\ddot{u}\} + \delta\phi\bar{\sigma}\big\}dV - \iint_{S_1} \{\delta u\}^T\{\bar{T}\}dS + \iint_{S_2} \delta\phi\bar{\sigma}'dS
$$

$$
- \{\delta u\}\{P\} + \delta\phi Q = 0 \tag{5.2}
$$

where the following prescribed quantities are defined as $\{u\}$ the displacement, $\{\ddot{u}\}$ the acceleration, $\{\bar{F}\}$ the body force, $\{\bar{T}\}$ the surface traction, $\{P\}$ the point force, ρ the density, δ a virtual quantity, ϕ the electric potential, $\bar{\sigma}$ the body charge, $\bar{\sigma}'$ the surface charge, and Q the point charge. The domains, V denotes the volume of the body, S_1 is the part of the boundary where traction is prescribed and S_2 is the part of the boundary where charge is prescribed. The variational principle can be thought of as a generalization of the elasticity principle of minimum potential energy, since deletion of the electrical quantities results in the principle's first variation.

To obtain the electroelastic relations in matrix for FEM, the continuous displacements and potentials are expressed in terms of i nodal values, as used in the finite element mesh, via interpolation functions f_u and f_ϕ:

$$
\{u\} = [f_u]\{u_i\} \tag{5.3a}
$$

$$
\phi = \langle f_\phi \rangle \{\phi_i\} \tag{5.3b}
$$

It is assumed that the interpolation function possess the requisite properties for convergence to the correct solution with diminishing element size. In a similar manner, the prescribed body and surface force (charge) distributions

are given through interpolation functions and nodal values:

$$\{\bar{F}\} = [f_{\bar{F}}]\{\bar{F}_i\} \tag{5.4a}$$

$$\{\bar{T}\} = [f_{\bar{T}}]\{\bar{T}_i\} \tag{5.4b}$$

$$\bar{\sigma} = \langle f_{\bar{\sigma}} \rangle \{\bar{\sigma}_i\} \tag{5.4c}$$

$$\bar{\sigma}' = \langle f_{\bar{\sigma}'} \rangle \{\bar{\sigma}_i'\} \tag{5.4d}$$

Differentiating Equation (5.3), there comes the equations of strain and electric field:

$$\{S\} = [B_u]\{u_i\} \tag{5.5a}$$

$$\{E\} = -[B_\phi]\{\phi_i\} \tag{5.5b}$$

Substituting Equations (5.3), (5.4) and (5.5) into (5.2), two general equilibrium equations could be obtained:

$$[m]\{\ddot{u}_i\} + [k_{uu}]\{u_i\} + [k_{u\phi}]\{\phi_i\} = \{F_B\} + \{F_S\} + \{F_P\} = \{F\} \tag{5.6a}$$

$$[k_{\phi u}]\{u_i\} + [k_{\phi\phi}]\{\phi_i\} = \{Q_B\} + \{Q_S\} + \{Q_P\} = \{Q\} \tag{5.6b}$$

The definition of terms in Equation (5.6) are:

$[k_{uu}]$ $\cdots$ Stiffness matrix

$[k_{u\phi}]$ $\cdots$ Piezoelectric stiffness matrix

$[k_{\phi u}]$ $\cdots$ Piezoelectric stiffness matrix

$[k_{\phi\phi}]$ $\cdots$ Dielectric stiffness matrix

$[m]$ $\cdots$ Kinematically consistent mass matrix

$\{F_B\}$ $\cdots$ Body force vector

$\{F_S\}$ $\cdots$ Surface force vector

$\{F_P\}$ $\cdots$ Concentrated force vector

$\{Q_B\}$ $\cdots$ Body charge vector

$\{Q_S\}$ $\cdots$ Surface charge vector

$\{Q_P\}$ $\cdots$ Point charge vector

Once the nodal displacement and electric potential for an element have been determined by Equation (5.6), stress and electric displacement at any point in the element can be given by Equations (5.5) and (5.1) as:

$$\{T\} = [c][B_u]\{u_i\} + [e][B_\phi]\{\phi_i\} \tag{5.7a}$$

$$\{D\} = [e]^T[B_u]\{u_i\} - [\varepsilon][B_\phi]\{\phi_i\} \tag{5.7b}$$

Without introducing additional notations, it is pertinent to consider the nature of the assembled structural equation, which is formed in the usual manner, simply by a nodal addition of elemental contributions. By performing a static condensation of $\{\phi\}$ degrees of freedom in Equation (5.6), we may write the structural equation as:

$$[k^*]\{u\} + [m]\{\ddot{u}\} = \{F^*\} \tag{5.8}$$

where $[k^*]$ is the condensed electroelastic stiffness matrix, in the form of:

$$[k^*] = [k_{uu}] - [k_{u\phi}][k_{\phi\phi}]^{-1}[k_{\phi u}] \tag{5.9}$$

and $\{F^*\}$ is the corresponding electromechanical force function, in the form of:

$$\{F^*\} = \{F\} - [k_{u\phi}][k_{\phi\phi}]^{-1}\{Q\} \tag{5.10}$$

To implement the modal analysis of a structure without regards to how resonance is initiated, $\{F^*\}$ is set equal to zero in Equation (5.8), then it becomes a standard eigenvalue problem:

$$([k^*] - \omega^2[m])\{u\} = 0 \tag{5.11}$$

Mathematically, this equation has the physical interpretation that a natural mode is a configuration in which electroelastic (stiffness) loads are in balance with inertial loads. The equality is satisfied when either $\{u\} = 0$ or the determinant of $[k^*] - \omega^2[m] = 0$. The first option gives the trivial solution and hence is of no interest. The second one gives the nontrivial solutions,

$$\left|[k^*] - \omega^2[m]\right| = 0 \tag{5.12}$$

If j is the order of the matrices, then the equation results in a polynomial of order j, which should have j roots: $\omega_1^2, \omega_1^2, \cdots, \omega_j^2$. These roots are the eigenvalues of the equation. When they are substituted into Equation (5.11), each vector can be calculated: $\{u\}_1, \{u\}_2, \cdots, \{u\}_j$. These vectors are known as

the eigenvectors. In the modal analysis, the eigenvalues represent the square of the natural angular frequencies of the structure (ω_j is the jth natural angular frequency) while the eigenvectors represent the corresponding mode shapes. In principle, the calculation of eigenvalues involves finding the roots of polynomial of order j. Therefore, an iterative solution is required. In ANSYS, the extraction of eigenvalues and eigenvectors from Equation (5.11) is commonly processed by the Reduced (Householder) method [47], which is a method to make a few degrees of freedom for representing all degrees of freedom of the model, in order to decrease the complexity of the problem. From Equations (5.8) and (5.11), the dynamical matrix equations of piezoelectricity are of identical form to the ordinary equations in structural dynamics. In particular, when the electrical and piezoelectric quantities in the two equations vanish, the ordinary structural dynamics equations are recovered as:

$$[k_{uu}]\{u\} + [m]\{\ddot{u}\} = \{F\} \tag{5.13}$$

$$([k_{uu}] - \omega^2[m])\{u\} = 0 \tag{5.14}$$

This indicates that the piezoelectric and elastic solid elements can be solved concurrently in a finite element model.

5.3 Finite Element Models For the Design Prototypes

As depicted in Chapter 3, the prototype of our nebulizer device mainly consists of two parts: a ring or disk shaped piezoelectric ceramic and a ultrasonic horn. In our project, we have adopted PZT, BSZT ceramic disks and PZT, KNN ceramic rings as the driving elements for solid and hollow horn (Figure 3.6 and 3.7)respectively. The horns are made of titanium. Therefore, the finite element model should also contain these two parts: the piezoelectric ceramic and the titanium horn. In our finite element models, the piezoelectric elements are assumed to have a linear and anisotropic property while the metal components have linear and isotropic properties. The material properties which have been used in the finite element models are listed in Table 5.1. The data of PZT, BSZT and KNN lead-free ceramics are calculated from the characterization result (Chapter 3) and the data of and titanium comes from the manufacturer. The elastic properties of KNN are not known. Hence, we use the elastic properties of BSZT in the simulation assuming that they are similar. Since changes on elastic compliances have minor influence to the simulation, the simulation result of KNN is still meaningful.

The geometries of the models were created by a CAD tool and then imported to the FEA software. In the real case, the two plane surfaces of the piezoelectric ceramic element are covered with silver layers as the electrodes and there is an epoxy layer between the piezoelectric ceramic element and titanium horn. These layers have thicknesses of $\sim 10\mu$m; they are ignorable when compared with all the relevant acoustic wavelengths at the frequency

Table 5.1   Data of material properties used in the finite element modeling.

Parameter	Unit	PZT APC-410	BSZT	KNN	Titanium
ϵ_{11}^{S}	-	1730	404	279	-
ϵ_{33}^{S}	-	1700	684	295	-
d_{33}	pC/N	374	200	92	-
d_{31}	pC/N	-171	-98	-32	-
d_{15}	pC/N	584	240	110	-
ρ	kg/m^3	7750	5800	4650	4730
s_{11}^{E}	$\times 10^{-12}$m^2/N	16.4	8.3	-	-
s_{12}^{E}	$\times 10^{-12}$m^2/N	-5.74	-2.31	-	-
s_{13}^{E}	$\times 10^{-12}$m^2/N	-7.22	-2.03	-	-
s_{33}^{E}	$\times 10^{-12}$m^2/N	18.8	8.1	-	-
s_{44}^{E}	$\times 10^{-12}$m^2/N	47.5	20.9	-	-
s_{66}^{E}	$\times 10^{-12}$m^2/N	44.3	21.2	-	-
Y	GPa	-	-	-	115
σ	-	-	-	-	0.3

range of interest ($\sim$ 100kHz). Hence, they were neglected from the finite element models.

A h-type adaption [48] is applied in the analysis. At least 8 element nodes are required to approximate a shear wavelength. To provide a highly refined mesh for the model, 3D coupled-field solid elements SOLID98 and 3D structural solid elements SOLID45 are used to mesh the piezoelectric ceramic and stepped horn respectively. SOLID98, as shown in Figure 5.2(a), is defined by

ten nodes with up to six degrees of freedom at each node. It has a quadratic displacement behavior and is well suited to model irregular meshes. When used in structural and piezoelectric analyses, SOLID98 has large deflection and stress stiffening capabilities. Figure 5.2(b) shows a schematic diagram of SOLID45, which has been used for the 3D modeling of solid structures. The element is defined by eight nodes having three degrees of freedom at each node: translations in the nodal x, y, and z directions. The element has plasticity, creep, swelling, stress stiffening, large deflection, and large strain capabilities.
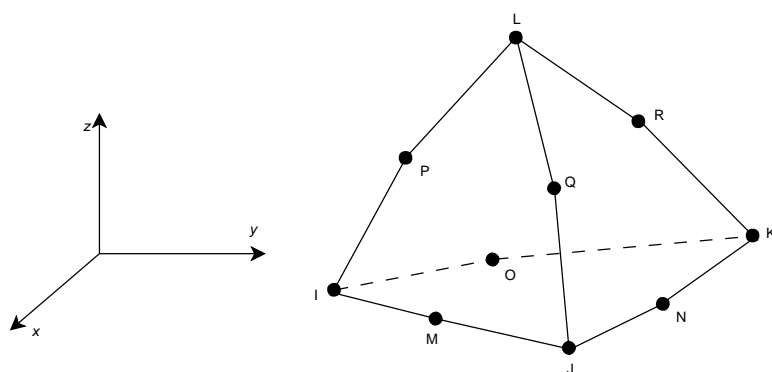
(a) SOLID98
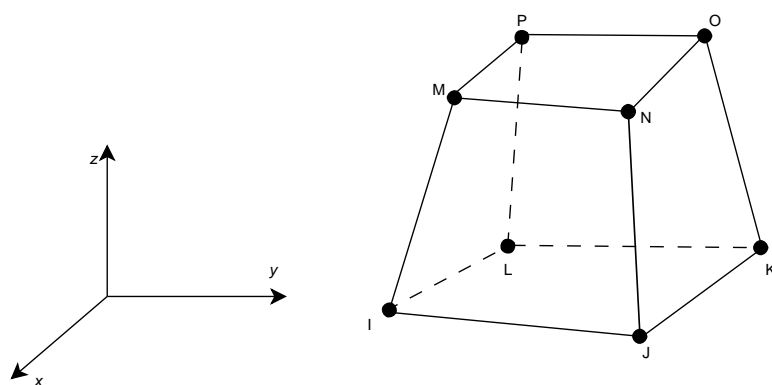
(b) SOLID45

Figure 5.2   3D coupled-field solid element SOLID98 and 3D structural solid element SOLID45 used in the finite element models.

Figure 5.3(a) is the finite element model of the solid horn transducer while Figure 5.3(b) represents the model of the hollow horn transducer. Meshing is restricted by the length of the element size, which is set to a range from 0.3 to 1.0 mm depending on the region shapes. The temperature and magnetic degrees of freedom of SOLID98 elements are not taken into account. All active displacement degrees of freedom are selected as the master degrees of freedom.

(a) Solid horn on a BSZT ceramic disk   (b) Hollow horn on a PZT APC-840 ring
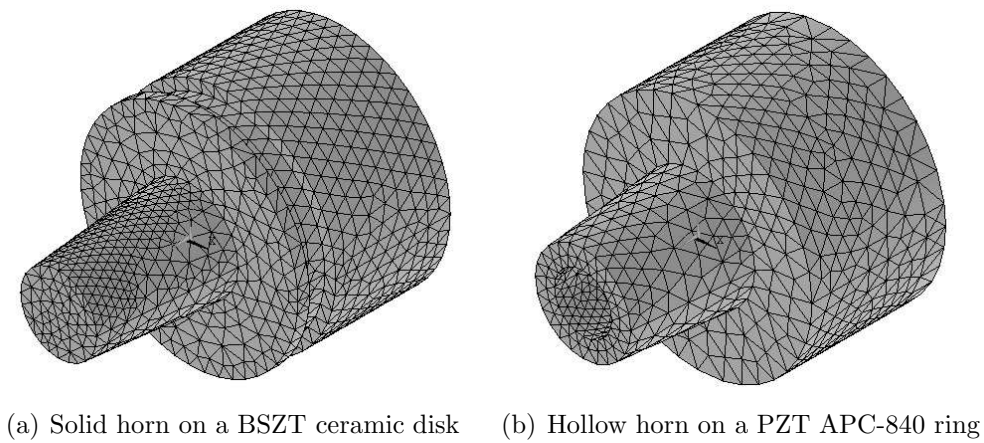
Figure 5.3   Finite element models of the stepped horn transducers.

5.4   Finite Element Analysis of The Transducers

5.4.1   Modal Analysis

ANSYS provides a tool of modal analysis which resolves the natural frequencies and extract the resonant modes of the finite element models. The analysis ascertains the linear response of the structure but without nonlinearity

consideration. Our nebulizer prototype is designed to work at its resonance frequencies since the vibration amplitude can be significantly enhanced there. To find the natural frequencies of the resonance, the applied voltage is set to zero by grounding all electrodes.

The lowest 30 natural frequencies and mode shapes of the stepped horn transducers (including the solid horn with a PZT PKI-402 disk, the solid horn with a BSZT lead-free ceramic disk, the newly designed hollow horn with a PZT APC-840 ring and the new hollow horn with a KNN ring) are computed, as listed in Table 5.2. Among them, only few are of interest: ones with both large axial displacement of the horn tip and high frequencies. The preferred mode of each transducer type is underlined.

Typically, Figure 5.4(a) describes the deformed shape of the solid horn transducer with BSZT lead-free ceramic disk at 183.23kHz mode and Figure 5.4(b) show the displacement distribution contour. At this preferred mode, the horn tip vibrates parallel to the axis with a large displacement. Figure 5.5(a) and 5.5(b) shows the deformed shape and displacement contour of the hollow horn transducer with a PZT ring. The other two transducers, solid horn on PZT disk and hollow horn on lead-free ring, exhibit a similar manner, so they are not plotted repeatedly.

Many modes listed in Table 5.2 are of no interest. The transducer at these modes does not offer a large axial displacement, but it twists or sways instead. Figure 5.6(a) and 5.6(b) give two examples of unwanted modes of the solid horn transducer while Figure 5.7(a) and 5.7(b) are unwanted modes for the hollow horn transducer. In Figure 5.6(b) and 5.7(b) the transducer twists and no axial displacement of the horn tip could be observed. In Figure

Table 5.2   First 30 computed natural frequencies (kHz) of the four types of trans-
ducers.

Mode number	Solid horn with PZT	Solid horn with BSZT	Hollow horn with PZT	Hollow horn with KNN
1	79.92	80.70	91.61	92.28
2	80.17	80.94	91.74	92.32
3	144.13	144.82	99.83	114.51
4	150.30	<u>183.23</u>	100.22	114.68
5	151.93	185.57	144.98	145.76
6	<u>179.66</u>	186.13	147.04	150.79
7	204.82	210.71	147.21	150.84
8	204.92	210.81	147.64	165.84
9	205.13	220.79	178.43	186.97
10	227.26	238.78	178.69	187.06
11	227.39	238.97	180.45	<u>199.92</u>
12	228.97	253.13	180.75	211.08
13	229.60	253.20	188.77	211.19
14	232.40	270.19	188.94	215.85
15	232.44	270.29	<u>192.67</u>	218.57
16	233.66	271.54	197.72	218.96
17	241.85	300.32	227.78	228.97
18	242.05	301.43	228.48	230.16
19	279.91	301.46	229.03	236.37
20	293.95	318.04	229.51	236.66
21	294.25	318.38	231.45	240.41
22	297.37	320.86	243.85	271.38
23	297.51	321.09	245.28	271.72
24	297.73	348.29	252.94	278.19
25	297.82	348.49	253.23	278.22
26	315.28	353.58	253.28	285.13
27	316.72	353.88	253.82	285.30
28	324.34	364.07	258.40	289.76
29	324.79	364.83	259.36	290.22
30	329.07	365.91	263.35	313.10
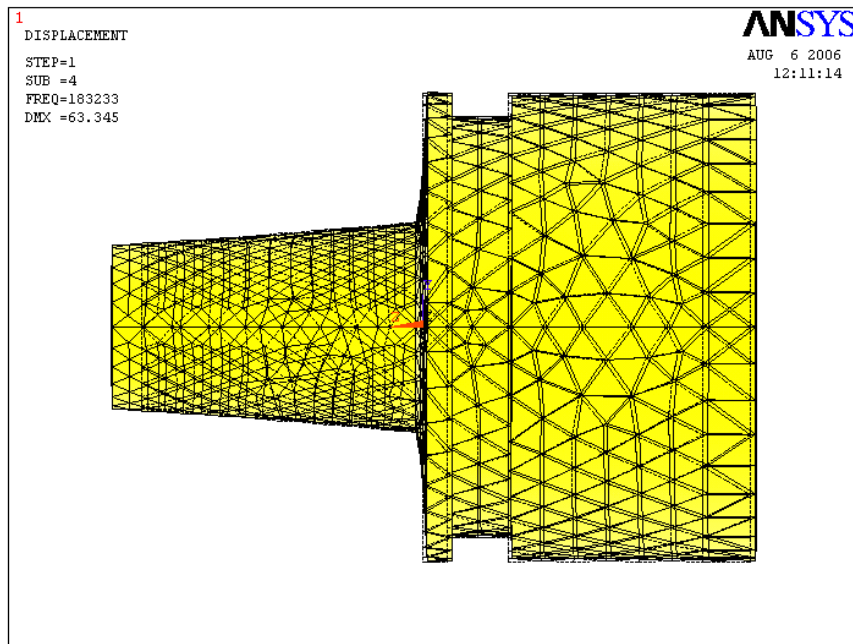
(a) Deformed shape with undeformed in dashed line
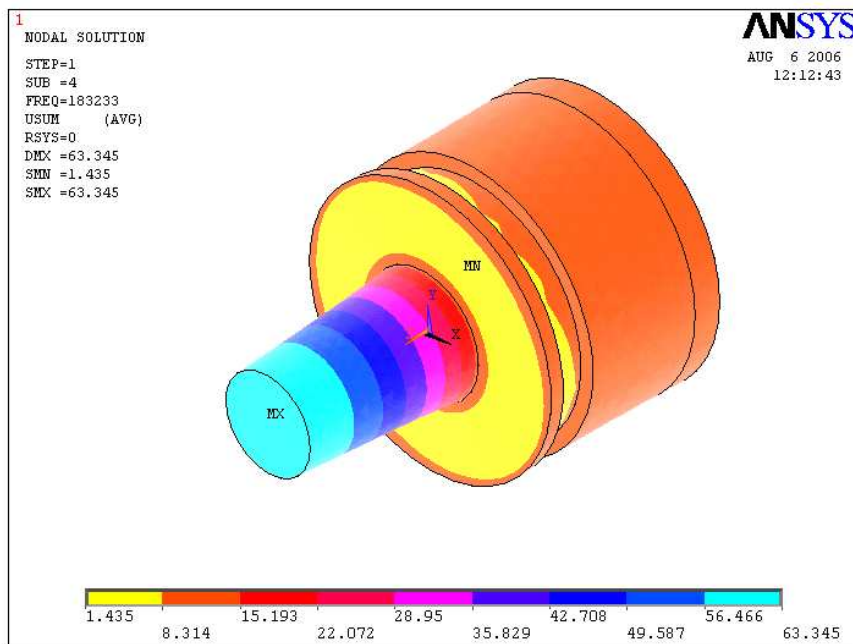
(b) Displacement distribution contour

Figure 5.4   Solid horn with BSZT lead-free ceramic disk transducer at 183.23kHz mode.
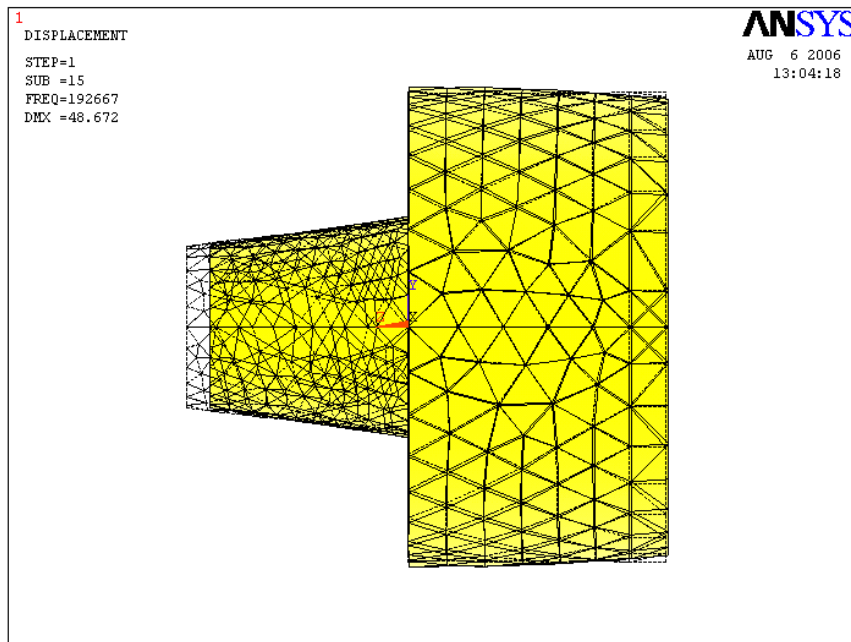
(a) Deformed shape with undeformed in dashed line
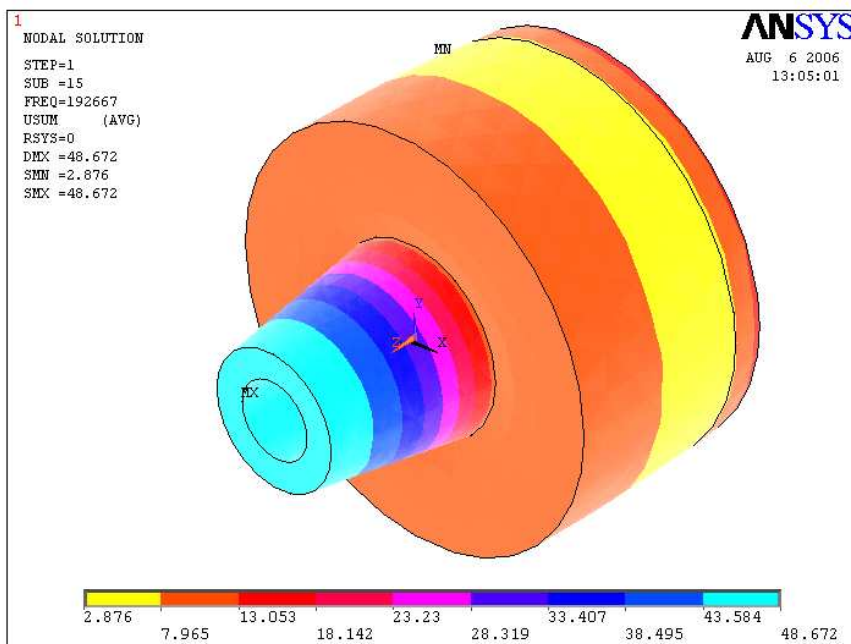
(b) Displacement distribution contour

Figure 5.5   Solid horn with KNN lead-free ceramic disk transducer at 192.67kHz mode.

5.6(a) and 5.7(a), the horn shakes and the displacement of the horn tip is not only small but also nonuniform.

(a) 210.71kHz   (b) 220.79kHz
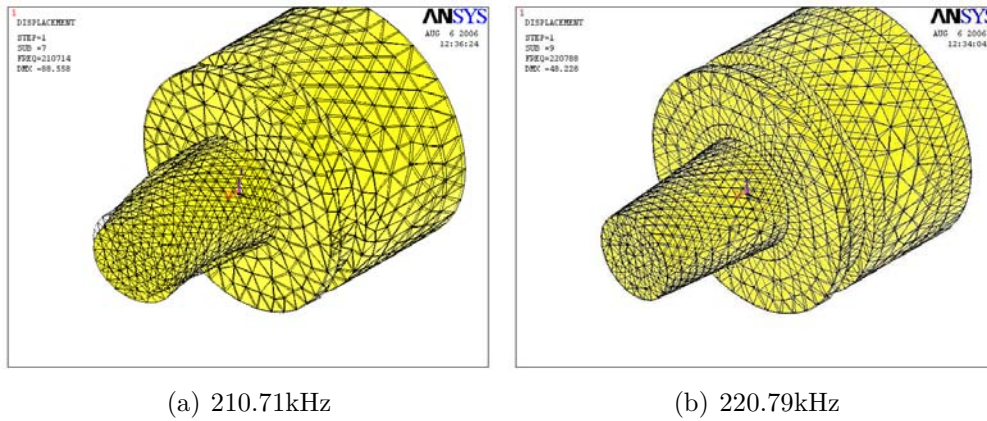
Figure 5.6   Two unwanted modes of the solid horn with BSZT ceramic disk transducer.

(a) 178.43kHz   (b) 197.72kHz
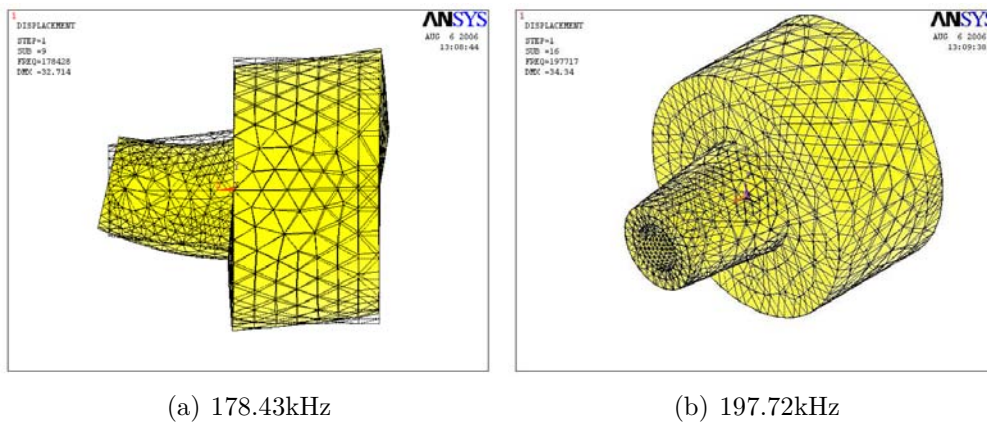
Figure 5.7   Two unwanted modes of the hollow horn with PZT ring transducer.

5.4.2   Harmonic Analysis

In the modal analysis, the device is computed under a short-circuit condition: the applied voltage is set to zero and the electrodes are grounded. In the real

case, when an AC voltage is applied, the piezoelectric ceramic vibrates and causes strain in the titanium horn. The mechanical vibration is transmitted and amplified by the stepped horn. If the electrical stimulation matches the resonance of the whole transducer, the vibration is significantly enhanced and the largest strain or maximum displacement at the horn tip could be achieved. ANSYS provides a tool named harmonic analysis to simulate this condition. Harmonic AC voltages are applied to the piezoelectric elements, the software solves the mechanical deformation of the finite element model. Figures 5.8(a) to 5.8(e) show the computed axial displacements of the horn tips versus the frequency axis near the resonance frequencies of the transducer models. They are for PZT disk with solid horn, BSZT disk with solid horn, KNN ring with hollow horn and PZT ring with hollow horn transducers respectively. One thing should be noted: for the lead-free KNN ring with hollow horn transducer, two modes with large axial displacements could be observed: one locates near 170kHz and another is near 200kHz, as shown in Figure 5.8(c) and 5.8(d). In the simulations we assume a 3V amplitude harmonic AC voltages are applied to the piezoelectric elements.

Since damping and boundary conditions are not included in the finite element models, the peak value of the axial displacement could be infinite theoretically. In fact, the absolute peak value in a computed displacement-frequency plotting (Figures 5.8(a) to 5.8(e)) is meaningless, but the width of the peak indicates the relative strength of the vibration at each mode. More importantly, the simulations calculate the resonance frequencies accurately: in fact, the peak frequencies match the experimental results (seeing Chapter 6) very well.
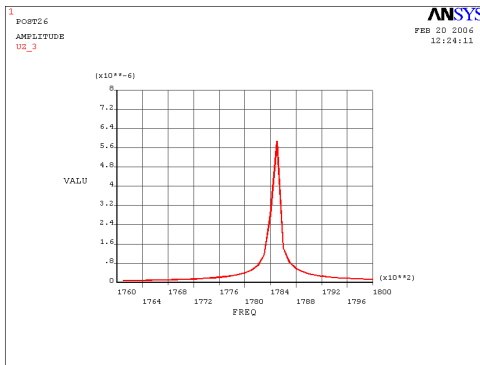
(a) Solid horn with PZT disk
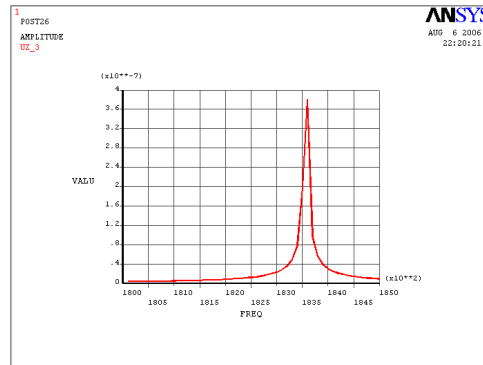
(b) Solid horn with BSZT disk
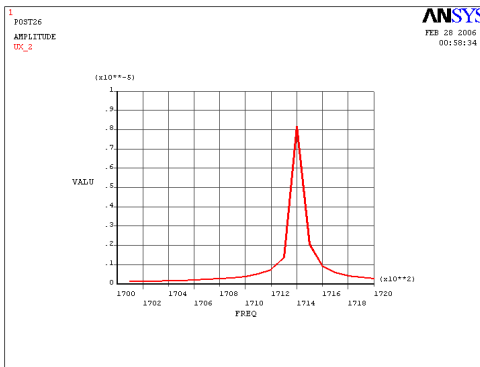
(c) Hollow horn with KNN ring, mode one
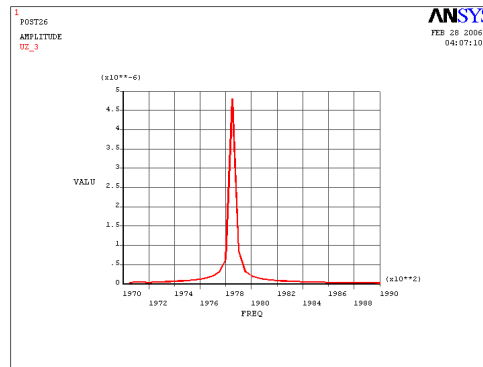
(d) Hollow horn with KNN ring, mode two
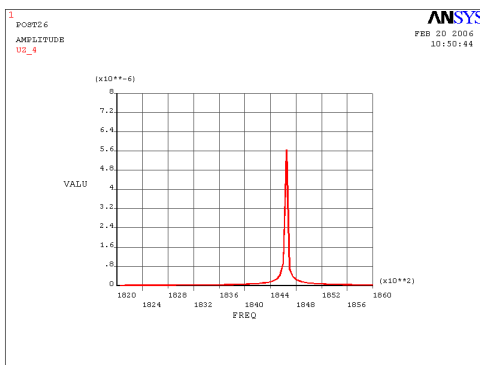
(e) Hollow horn with PZT ring

Figure 5.8 Computed axial displacement of the horn tips versus frequency.

Additionally, we studied the deformation behavior of the horn tip. Four nodes at different positions on the horn tip plane are chosen as shown in Figure 5.9. Their displacements are computed at resonance. The four nodes have nearly the same displacements: the differences between them are in the order of 10^{-9}m, which is less than 1/1000 of the displacement value. This result shows that the horn tip plane does not suffer from a torsion while vibrating, which means the mesh mounted on the tip in our nebulizer would just vibrate along the symmetry axis as anticipated.
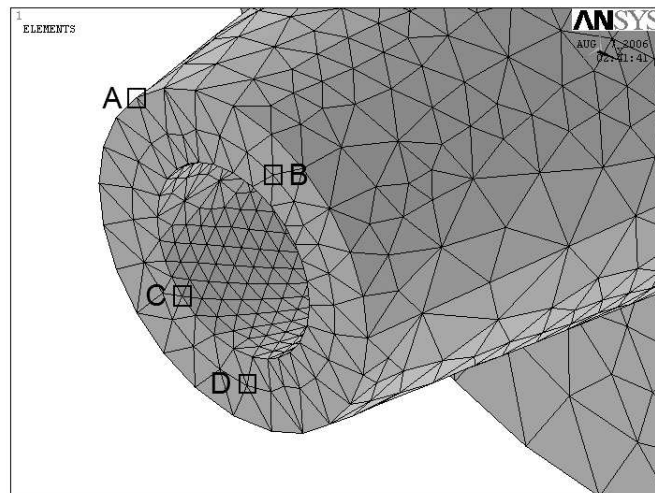
Figure 5.9   Nodes on the horn tip plane.

Chapter 6

Displacement Performance of The Transducer

6.1 Introduction

Generally, electro-mechanically coupled transducers or actuators can be divided into two types: high-force output transducers/actuators and high-displacement output transducers/actuators, according to their output. The former type usually have a large force output but with relatively small displacement, while the later ones are on the contrary. For these transducers, especially the high-displacement output transducers, the output displacement is an essential parameter in transducer design and, hence, the measurement of displacement is essential.

Particularly in our case, the nebulization performance of our device is directly influenced by the axial vibration velocity of the horn tip and the velocity is related to the axial vibration amplitude or the tip displacement.

The nebulization performance and vibration displacement are discussed in the next chapter. In this chapter, after the fabrication and characterization of the piezoelectric stepped horn transducers, the axial peak-to-peak displacements of the horn tips have been measured by a laser vibrometer (Polytec outplane vibrometer, Model No. OFV-3001). The setup is shown in Figure 6.1. Laser vibrometers are used to measure the vibrations of objects in the directions of a laser beams. The principle of the instrumentation is based upon the Doppler effect. Axial displacements of various types of horns (solid and hollow) with different driving elements (PZT and lead-free ceramics) have been measured. Their displacement amplitudes have been compared.

Figure 6.1   A photograph of the Laser Doppler Vibromter setup in our laboratory.

6.2 The Displacement Measurement Instrumentation

Unlike traditional contact vibration transducers, Laser Doppler Vibrometers (LDVs), require no physical contact with the test object. Remote vibration measurements on targets that are difficult to access are typical applications where a laser-based vibration transducer would be the choice. For example, LDVs can measure vibrations up to 30MHz with very linear phase response and high accuracy. Measurements of the surface of liquid materials or vibrations of very small and light structures can also only be made using non-contact measurement techniques. Furthermore, the ability to incorporate advanced, optical mirror systems together with the laser source provides the measurements a superior resolution and accuracy.

6.2.1 Principle of Laser Doppler Vibrometry

Laser Doppler Vibrometry is based on the principle of optical interferometry. Figure 6.2 shows a schematic diagram of a directionally sensitive type of interferometer (a modified Mach-Zehnder interferometer), which combines a laser with a Laser Doppler Vibrometer sensor head.

The helium-neon laser has an extremely stable wavelength (0.6328μm in this Laser Doppler Vibrometer). A polarizing beam splitter prism BS1 splits this into an incident beam, to be emitted from the sensor head to the object surface, and a reference beam, which remains within the vibrometer. The linearly polarized incident beam passes through a second polarizing beam
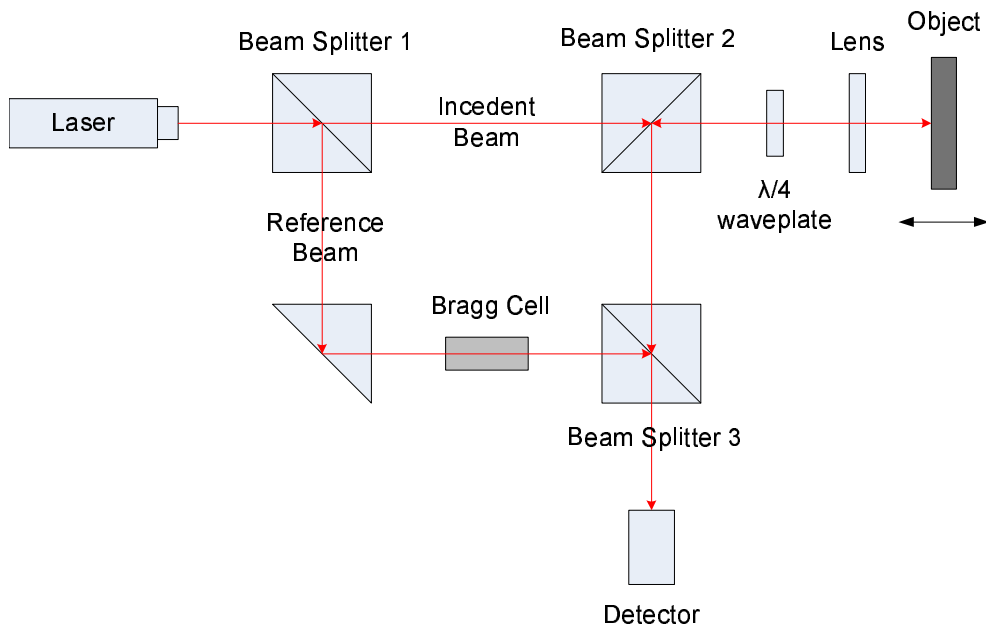
Figure 6.2   Schematic diagram of the optical configuration in the interferometer [50]

splitter BS2 and then a $\lambda/4$ waveplate, which converts it to a circular polarized light. A lens then focuses the beam onto the surface of the object under test. After reflection, the beam passes back through the lens and is converted to a plane polarized light by the $\lambda/4$ waveplate. The direction of polarization of the reflected beam is orthogonal to that of the incident beam. The reflected beam is then deflected by beam splitter BS2 to a third beam splitter BS3 where it is recombined with the reference beam causing optical interference. The interference signal is converted into an electrical signal by the photo detectors (two are used to minimize noise and drift) which is then decoded by the electronics controlling circuit.

Velocity Determination

If the incident beam from a vibrometer is focused onto a moving surface, it experiences a Doppler frequency shift upon reflection from that surface. The frequency of the reflected beam is higher than that of the incident beam if the surface is moving towards the vibrometer and lower if the surface is moving away. This Doppler frequency shift is a function of the velocity component v in the direction of the incident beam:

$$f_D = 2 \cdot \frac{v}{\lambda} \tag{6.1}$$

where f_D is the Doppler frequency shift and λ is the wavelength of the laser.

If the reflected beam is combined with the incident beam, a beat frequency or intensity modulation equals to the magnitude of the Doppler frequency shift will be generated in the resultant beam. If this resultant beam is measured using photo detectors, the electrical signal will fluctuate at a frequency:

$$f' = |f_D| = 2 \cdot \frac{|v|}{\lambda} \tag{6.2}$$

Analyzing this signal could only obtain the magnitude of the velocity. Hence, a Bragg cell is combined within the reference beam. The Bragg cell adds a fixed frequency shift f_B to the reference beam (the frequency f_B in our system is 40MHz). As a result, the overall frequency shift when the reflected incident beam and the reference beam are combined is equal to the sum of the Bragg

frequency shift and the Doppler frequency shift.

$$f_{dect} = f_B + f_D \qquad (6.3)$$

As the frequency shift introduced by the Bragg cell is known, the analysis of the detected signal can yield the magnitude and direction of the velocity of the moving object.

Displacement Determination

Displacement information, when calculated by the integration of the velocity signal, can become inaccurate due to the integration errors at low frequencies. Therefore, more modern systems include a decoder which enables the displacement to be measured independently of the velocity.

When the reflected and reference beams are combined within the vibrometer sensor head, optical interference occurs producing a fringe pattern. The resulting intensity, I, measured by the photo detectors varies with the phase difference $\Delta\varphi$ between the two beams according to the equation:

$$I = \frac{I_{max}}{2} \cdot (1 + \cos \Delta\varphi) \qquad (6.4)$$

The phase difference $\Delta\varphi$ comes from the path difference (ΔL) between the incident beam and the reference beam.

$$\Delta\varphi = 2\pi \cdot \frac{\Delta L}{\lambda} \qquad (6.5)$$

When the incident beam from the vibrometer is reflected by the moving

surface, the path difference is a function of time. Thus, the displacement of the moving object as a function of time can be determined by counting the fringes pass over the photo detector.

6.2.2 Signal Processing

The laser vibrometer of the heterodyne interferometer type uses an acousto-optic modulator in one arm of the interferometer. It generates a frequency modulated carrier signal in the RF region, and the center frequency of the carrier signal is identical to the acousto-optical modulator drive signal. The directionally sensitive Doppler information is thus contained in the RF carrier: The object velocity determines direction (+/-) and amount of frequency deviation with respect to the center frequency (Figure 6.3).

The Doppler frequency is proportional to the vibrating velocity of the surface and the phase change $\Delta\varphi$ with respect to the phase φ_0 of the reference signal is proportional to the displacement of the object surface.

Velocity Decoding

To decode the velocity, the RF detector signal is mixed with a variable local oscillator frequency before demodulation. The output signal of the velocity demodulator $v(t)$ is related to the input frequency f_{mod} via a linear relationship (Figure 6.4). Because of the Doppler effect, the frequency modulation $\Delta\varphi$ of the RF carrier is proportional to the measuring velocity: $\Delta f = 2v/\lambda$, where λ is the wavelength of the laser light. Hence, the required modulation bandwidth can be estimated as $2(\Delta f + f_{vib})$ where f_{vib} is the vibration fre-
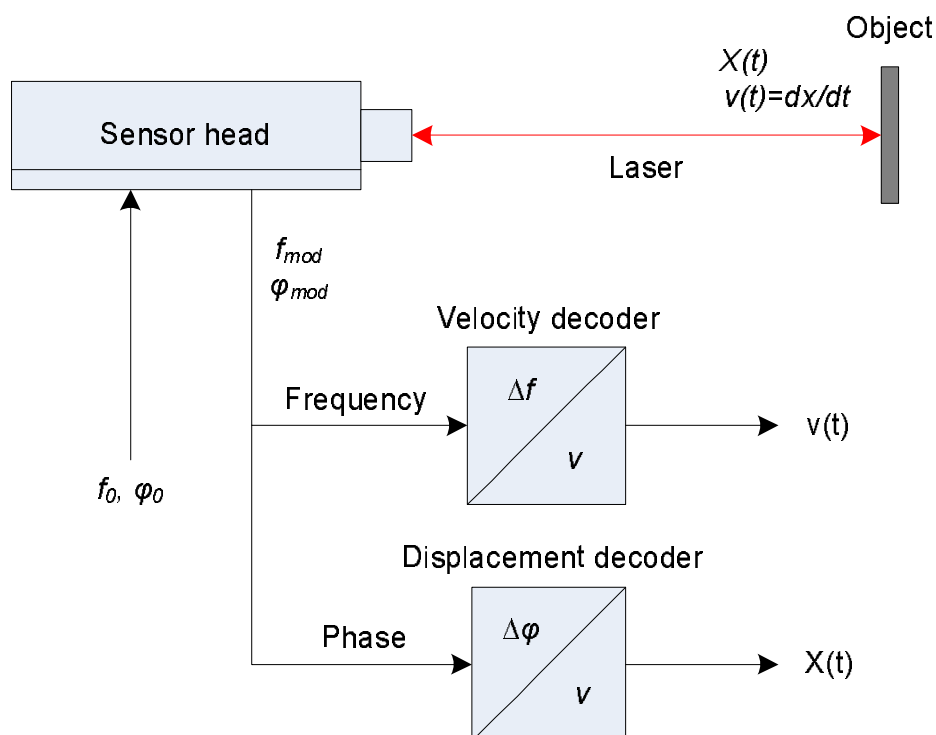
Figure 6.3   A schematic diagram showing the signal processing in the vibrometer system [50].

quency of the measuring object. In order to cover the ranges of applications required, several demodulation techniques can be used: the Phase Locked Loop (PLL), the coincidence demodulator techniques and as a new development digital demodulation using nearly real-time DSP techniques [51]. Figure 6.5 gives the main procedures in the velocity decoding process.

Displacement Decoding

The laser vibrometer measures the displacement by counting the fringes. Values of displacements are electronically derived by measuring the phase change at the detector as the surface motion of the object changes the total path length of the beam. A displacement of $\lambda/2$ changes the phase by 2π.
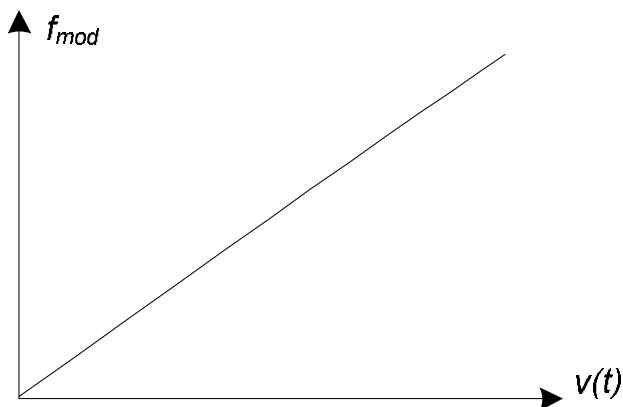
Figure 6.4   The relationship between the vibrating velocity and the modulation frequency.
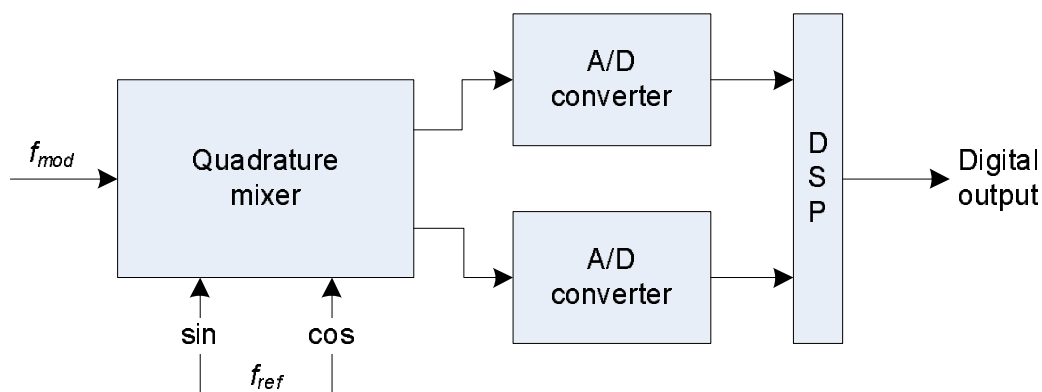
Figure 6.5   The general process of velocity decoding.

By counting the zero-crossings or "fringes" the laser vibrometer measures the distance which the object moves, with an increment of $\lambda/2$ per count. With a D/A converter the digital information is changed into a voltage on time output. The decoding process is demonstrated in the following figure.
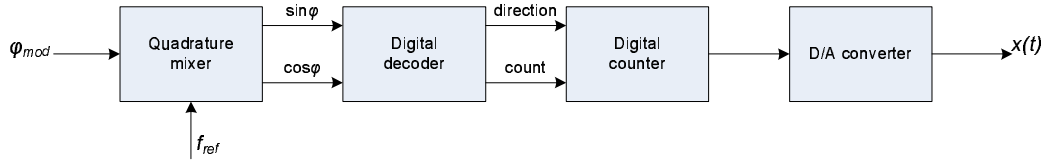
Figure 6.6   The general process of displacement decoding.

6.3   Displacements of Solid Horns

Our new liquid nebulizer is based on a piezoelectric ceramic driven hollow horn transducer. As seen in the FEM simulations in Chapter 5, the center drilled hole on the horn is not very big and does not substantially influence the mechanical properties. The experimental studies start with solid horns bonded with piezoelectric ceramic disks. Both the PZT and lead-free BSZT disks are bonded on the horns by resin epoxy. The dimensions and photo of the device are shown in Figure 6.3.

6.3.1   Solid Horn with a PZT Ceramic Disk

To test the displacement of different horn transducers, we first measured a PZT based one as a reference. The solid stepped horn was bonded to a PZT 402 ceramic disk. The horn transducer was fixed on the experimental table. It was held at its nodal plane, i. e. the position near the stepped surface.

(a) Dimensions   (b) Photograph
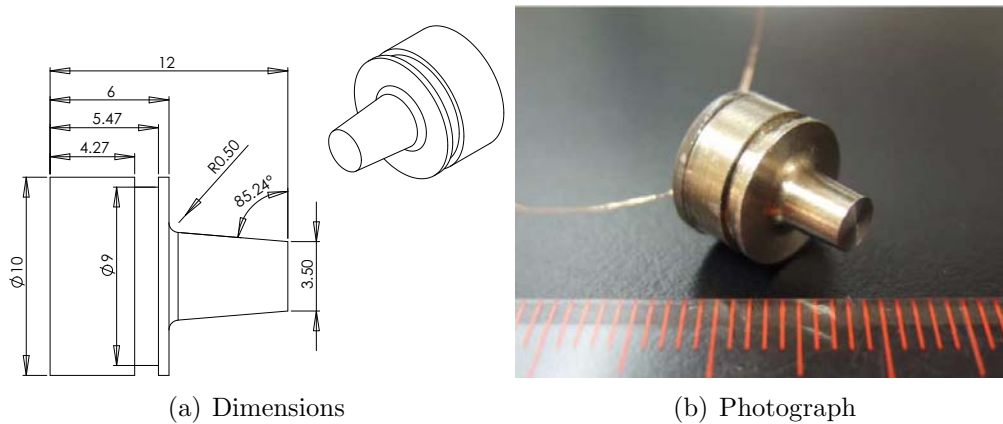
Figure 6.7   Schematic and photograph of a solid stepped horn transducer.

The axial peak-to-peak displacement of the horn tip, i.e. two times the vibration amplitude, was measured by a Laser Doppler Vibrometer: Polytec outplane vibrometer, Model No. OFV-3001. The experimental data are plotted in Figure 6.8. This figure was measured under a 3V continuous sinusoidal driving voltage. A sharp displacement peak could be observed near 180kHz. The maximum axial displacement value is 0.428µm at 180.0kHz, which matches the resonance peak in the impedance spectrum (Chapter 3) very well. The resonance frequency was predicted accurately by the finite element modeling (Chapter 5) also.

6.3.2   Solid Horn with a Lead-free Ceramic Disk

For a lead-free ceramic based transducer, the axial displacement of the horn tip was measured and plotted in Figure 6.9. The piezoelectric ceramic is a BSZT disk. To compare this performance with the PZT-based transducer, the results were measured under the same driving voltage, i.e. a 3V continuous sinusoidal signal. The displacement of PZT based transducer is also
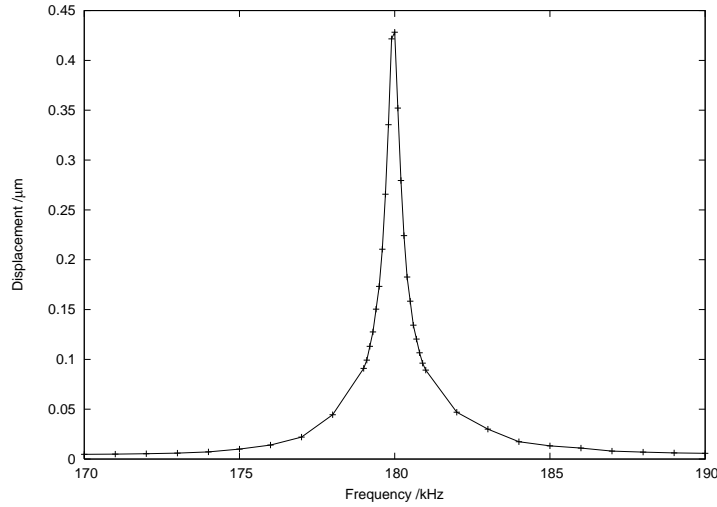
Figure 6.8   Axial displacements of a horn tip, driven by a PZT-402 disk, as a
function of frequency under a 3V amplitude sinusoidal voltage near
the resonance frequency.

plotted as a comparison.

The peak of the BSZT curve is lower than the PZT one. It is located
at 183.6kHz, which differs from the PZT one by 3.6kHz. The maximum
displacement is 0.381µm which is about ten per cent lower than the PZT
one.

6.3.3   Discussion

Several important properties of the PZT and BSZT ceramics from the char-
acterization results in Chapter 3, are listed in Table 6.1.

Table 6.1   Piezoelectric properties of three different types of ceramics.

	d_{33}	Coupling factors		Mechanical	N_t^D	Z_a
	(pC/N)	k_p	k_t	Q factor	(m·Hz)	(MRayl)
PZT-402	275	0.52	0.47	500	2032	30.9
BSZT	200	0.49	0.49	250	1913	25.3
KNN	92	0.40	0.47	800	3150	29.6
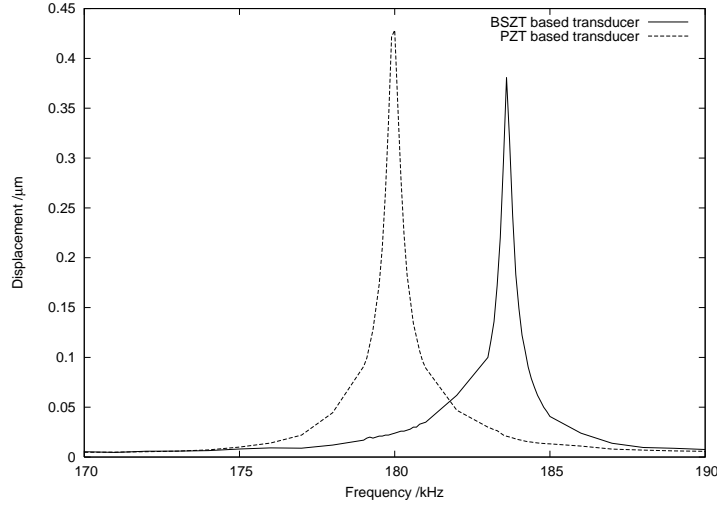
Figure 6.9   Axial displacements of the horn tip against the frequency, driven by a BSZT disk, as well as the one driven by a PZT-402 disk for comparison, under a 3V amplitude sinusoidal voltage near the resonance frequency.

From Figure 6.9, a frequency shift of the displacement peak (i.e. the change of resonance frequency) could be observed between the PZT and lead-free curves. This is due to the lower density (BSZT: 5850kg/m^3, PZT: 7600kg/m^3), acoustic impedance (BSZT: 25.3MRayl, PZT: 30.9MRayl) and frequency constant N_t^D (BSZT: 1913m$\cdot$Hz, PZT 2032m$\cdot$Hz) of the lead-free ceramic. The displacement of the lead-free ceramic based transducer is comparable with the one of PZT based transducers: there is only ten per cent difference in maximum displacement, but PZT has a forty per cent higher d_{33} than BSZT. A reasonable explanation for this fact is: the lead-free BSZT ceramic has an acoustic impedance better matched to that of titanium (Z_a =26MRayl) than PZT (see Table 6.1) which compensates for its lower piezoelectric properties.

6.4 Displacements of Hollow Horns

In our new nebulizer, there is a hole channel along the axis in the center of the stepped horn to allow the liquid to flow to the mesh on the horn tip, and we use piezoelectric ceramic ring as the driving element instead of the ceramic disk in the solid horn transducer. Using FEM simulations, it is found that a larger center hole gives a stronger nebulizing capability. Therefore, after optimization through FEM simulations the hollow horns are made with a larger diameter than the solid horn and the ceramic rings have a 12.7mm outer diameter comparing with 10.0mm diameter of a disk in a solid horn transducer. The center drilled hole has a diameter of 3mm.

6.4.1 Hollow Horn with a PZT Ceramic Ring

We still use the Laser Doppler Vibrometer to measure the vibration amplitude of the horn tip. The hollow horn was fixed on an experiment table by holding at its nodal plane (the place with minimum displacement which was predicted by the FEM simulation). Figure 6.10 shows the axial tip displacement against the frequency. The hollow horn transducer is driven by a PZT (APC-840) ring, and under a 3V continuous sinusoidal voltage. The displacement peak of 0.306μm is found at the frequency of 184.5kHz.

Clearly, we could increase the axial displacement of the horn tip by merely lifting the driving voltage. The displacements and the driving voltage have a good linear relation at a low displacement range, but when the driving voltage is increased, the displacement deviates from the line gradually, as shown in Figure 6.11. The displacement measurement was conducted at the
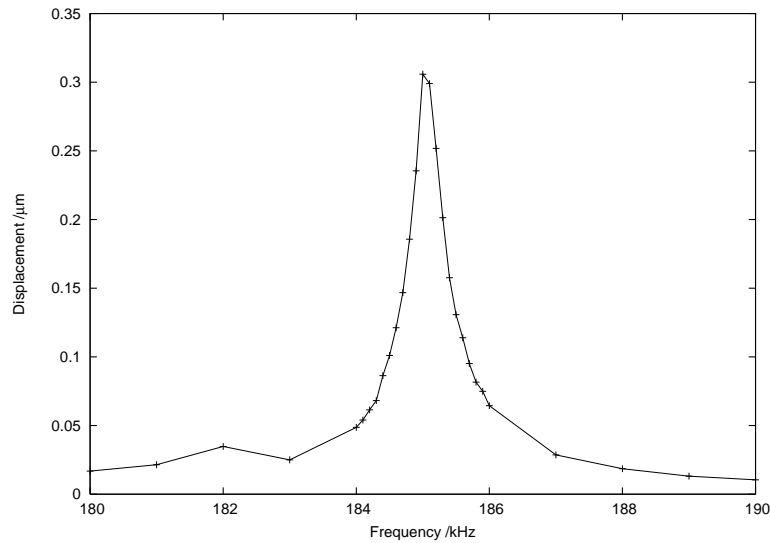
Figure 6.10   Axial displacements of the horn tip of a PZT (APC-840) ring based hollow horn transducer, as a function of frequency.

resonance frequency where the displacement peak is.

If we continue to lift the driving voltage, a maximum displacement of about 2.0μm could be achieved, and after this, the displacement remains constant in spite of the voltage increase, until the piezoelectric ceramic stops to function.

6.4.2   Hollow Horn with a Lead-free Ceramic Ring

Similar experimental measurements have been done for a hollow horn driven by a lead-free ceramic $((Na_{0.5}K_{0.5})NbO_3)$ ring. $(Na_{0.5}K_{0.5})NbO_3$ is one kind of hard lead-free ceramic which has a d_{33} of 90pC/N. The axial displacements as a function of frequency are plotted in Figure 6.12, and the displacement versus driving voltage curve at resonance are plotted in Figure 6.13. The displacements versus frequency curve is still measured under a 3V contin-
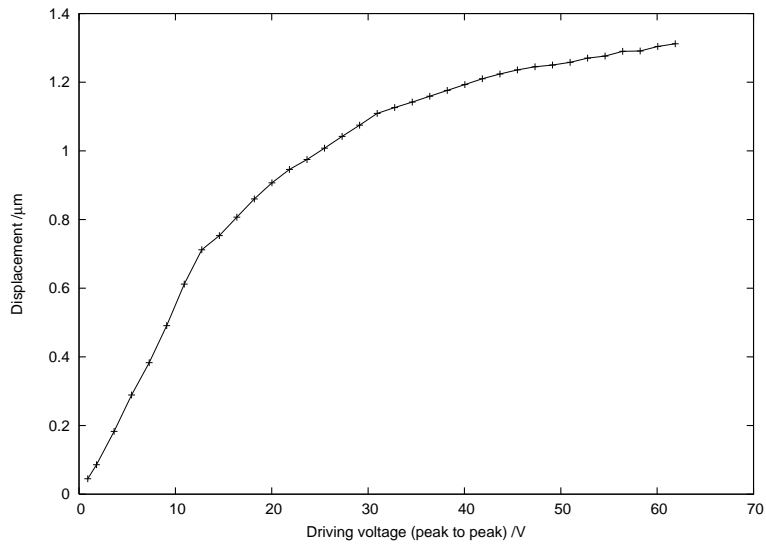
Figure 6.11   Axial displacements of the horn tip of a PZT (APC-840) ring based hollow horn transducer, as a function of the driving voltage, at 184.5kHz.

uous sinusoidal voltage; and the displacements on driving voltage curve is measured at its resonance frequency of 165.1kHz.
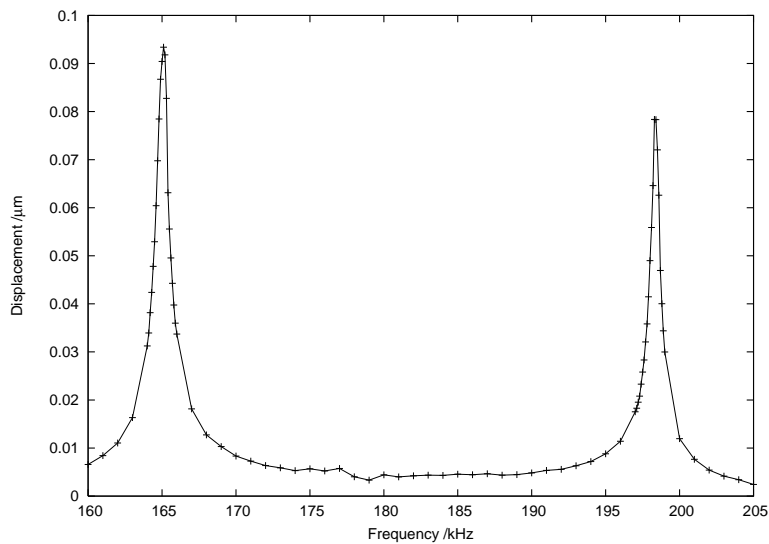
Figure 6.12   Axial displacements of the horn tip of a lead-free ceramic ring based hollow horn transducer, as a function of the frequency.
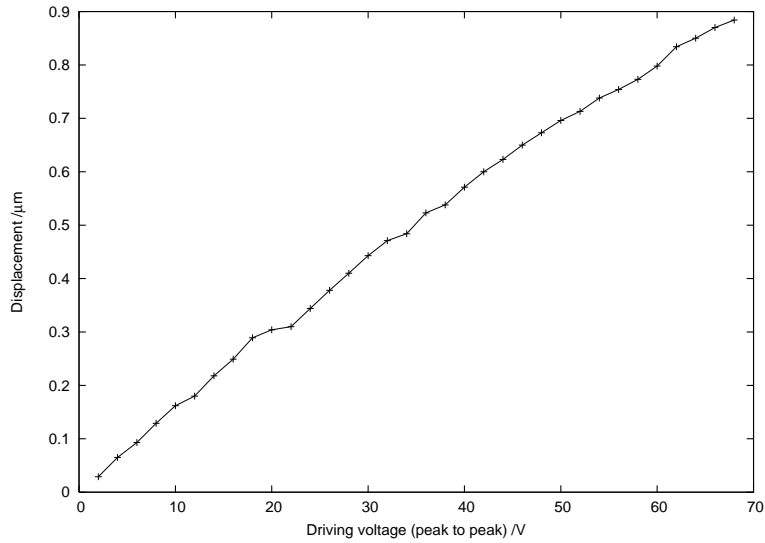
Figure 6.13   Axial displacements of the horn tip of a lead-free ceramic ring based hollow horn transducer, as a function of the driving voltage, at 165.1kHz.

6.4.3   Discussion

The hollow horn has different behavior compared to the solid horn. Comparing Figures 6.10 and 6.12, we could find that the ratio of the two maximum displacements (PZT: 0.306μm and lead-free: 0.093μm) is approximately equal to the ratio of d_{33} (PZT: 300pC/N and lead-free: 90pC/N) in the two ceramics. The advantage of "better acoustic impedance matching" in lead-free ceramics decreases or disappeared, because that the ceramic ring does not have a exact area adhering to the hollow horn base: the inner diameter of the ceramic ring ($d_i = 5$mm) is larger than the center hole of the horn.

It could be also noticed from Figures 6.11 and 6.13 that the lead-free one has a far better linear relation with the driving voltage than the PZT one. This is understandable, because the lead-free one has a smaller displacement

than PZT horn and even at 60V, the lead-free curve is in the linear range. This may be an advantage for our nebulizer, since we can drive it with higher voltage to get large displacement.

Chapter 7

Nebulization Performance of
The Nebulizer

7.1 Introduction

As reviewed in Chapter 1, nebulization or the generation of the micro liquid drops is a complicated process. In our nebulizer, we fabricated an alloy mesh with multiple holes and affixed it on the ultrasonic horn tip. While the mesh vibrates together with the horn tip at a high frequency ($\sim 10^5$Hz), the liquid behind the mesh is pushed through the holes. The liquid droplets get accelerated and are eventually atomized.

The alloy mesh is fabricated by electroplating. It is capped on the horn tip (see Figure 7.1(a)) and is replaceable. The mesh (Figure 7.1(b)) has a thickness of approximately 100μm and consists of multiple cone-shaped apertures. The diameter of the apertures on the inside surface is about 40μm and the apertures have a diameter of approximately 4μm on the outside

surface of the mesh.

(a) The mesh on the nebulizer   (b) A closer look of the alloy mesh

Figure 7.1   Photographs of the nebulizer and the alloy mesh.

Figure 7.2(a) and 7.2(b) show the inside and outside surface views of the mesh under a scanning electron microscope (SEM), well defined "cone-shape" can be seen.
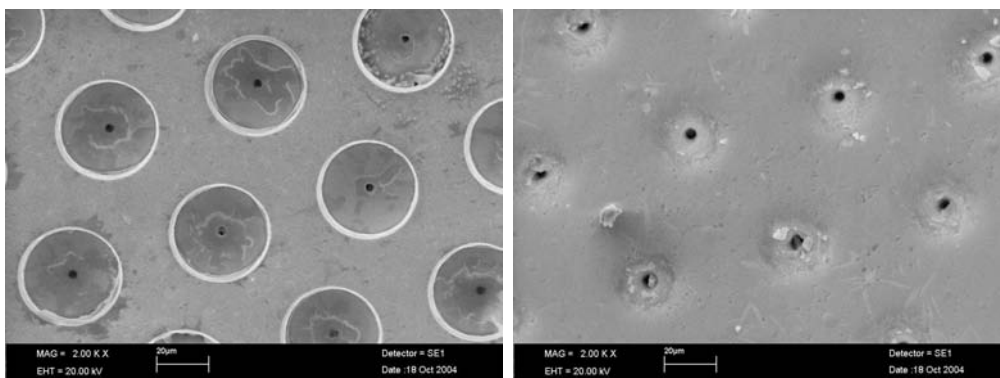
(a) Inside surface   (b) Outside surface

Figure 7.2   SEM micrographs of the inside and outside surfaces of the alloy mesh.

7.2   Some Calculations

The process of nebulization is essentially the process of generating micro droplets. The liquid behind the alloy mesh is pressed into the cone-shaped apertures and gets accelerated in each of them when the mesh vibrates together with the horn tip; the liquid volume in each aperture breaks off at the exit of the aperture and then forms a small liquid drop. This process starts and completes in one period of the vibration of the horn tip. Obviously, the newly formed liquid drops increase the total surface area of the liquid. It requires that the liquid volume at the exit of each aperture has a kinetic energy large enough to overcome the surface tension force of the liquid. Roughly, it requires:

$$E_{kinetic} > E_{surface} \tag{7.1}$$

And it is a necessary and critical condition of new drops generation. Replacing $E_{kinetic}$ as $mv^2/2$, $E_{surface}$ as $\sigma \cdot \Delta A$, a requirement of v, the velocity of liquid volume at the exit of an aperture, could be obtained:

$$v > \sqrt{\frac{2\sigma \cdot \Delta A}{m}} \tag{7.2}$$

where ΔA is the increased area of the droplet. σ and m are the coefficient of the liquid surface tension and the mass of the liquid volume, respectively. If we assume the newly formed drop is in a simple spherical shape with radius r (the assumption is not accurate but has a correct order of magnitude),

$\Delta A = 4\pi r^2$ and $m = \rho \cdot 4\pi r^3/3$, then Equation (7.2) could be simplified to:

$$v > \sqrt{6\sigma/\rho r} \qquad (7.3)$$

Equation (7.3) gives the requirement of the velocity of the liquid volume before it breaks off. To generate a water droplet with radius of 2μm at room temperature, the requirement can be calculated as $v > 14.7$m/s using the surface tension coefficient and density of water ($\sigma = 72.7 \times 10^{-3}$N/m, $\rho = 1000$kg/m^3).

On the other side, the maximum velocity of the vibrating mesh is:

$$v_{mesh} = 2\pi f z_0 \qquad (7.4)$$

where f is the working frequency and z_0 is the amplitude of the vibration. Consider the cone-shaped aperture in the nebulization process (Figure 7.3): when the mesh is moving toward the liquid in the hollow horn, the liquid will be compressed into the apertures; due to the incompressibility of the liquid, the expelled liquid has the same volume as the liquid getting into the aperture, that is:

$$A_o d_o = A_i d_i \qquad (7.5)$$

and it could be rewritten as:

$$\frac{v_o}{v_i} = \frac{A_i}{A_o} \qquad (7.6)$$

v_o is the velocity of the liquid volume at the exit of the aperture before nebulization and v_i is the velocity of the liquid relative to the vibrating

mesh, which equals to v_{mesh}.
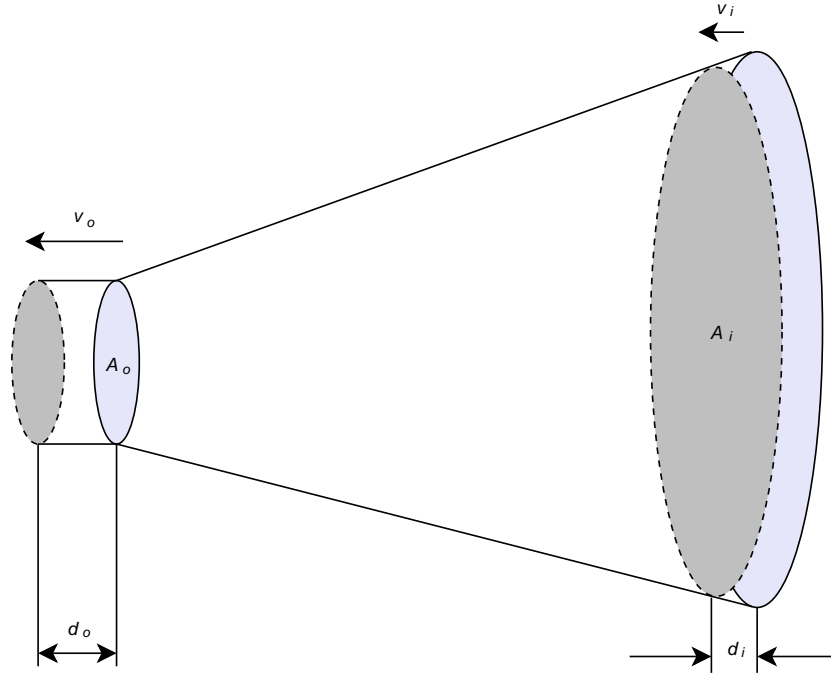
Figure 7.3   A cone-shaped aperture.

If we define an amplification factor $N = v_o/v_i$, there is:

$$N = \frac{A_i}{A_o} = (\frac{d_i}{d_o})^2 \tag{7.7}$$

d_i and d_o are the diameters of the two parallel surfaces. In our mesh design, $d_i = 40\mu m$ and $d_o = 4\mu m$ (Figures 7.2(a) and 7.2(b)), then $N_{max} = 100$. With the consideration of other aspects which may adversely influence M, such as the fluidity of the liquid, deformation of the mesh and friction, we assume $N \sim 10$ which is about one-tenth of the maximum value. Hence, at the working frequency of around 180kHz, if the amplitude of the mesh vibration reaches 1.5μm, a v_o of 17m/s could be obtained. It meets the requirement in

Equation (7.3): $v > 14.7$m/s. The nebulization can be obtained.

7.3 The Nebulization Performance

When an AC voltage with appropriate frequency is applied to the piezoelectric ceramic ring, the stepped horn transducer vibrates and the capped mesh vibrates together with the horn tip. If the driving frequency matches the resonance frequency of the transducer, the capped mesh and the horn tip obtains a maximum axial amplitude of the vibration. When this displacement exceeds a threshold value, the nebulization starts. In our experiment, we use water or low viscosity ink as the nebulizing liquid.

For the nebulizer with PZT (APC-840) ring, the working frequency is near 184.5kHz because the maximum displacement is located there (see the displacement spectrum: Figure 6.10). The loading of water may slightly shift the resonance frequency to the lower end. Experimentally, at a frequency of 183.9kHz, the nebulization starts with the lowest applied voltage. The nebulizing mist is visible to the naked eye when a 54V peak-to-peak voltage at 183.9kHz has been applied to the piezoelectric ring. At this condition, the displacement of the horn tip reaches 1.43μm as measured by the laser vibrometer. It matches our estimation in the previous section.

When the driving voltage increases, the nebulization becomes more intense because the larger amplitude of the mesh vibration generates larger size droplets. Meanwhile, the range of the nebulization increases since the generated microdrops obtained a higher initial velocity which is accompanied with the larger displacement of the horn tip. The photograph in Figure

7.4 records the nebulization when a 183.9kHz and a 70V peak-to-peak AC voltage is applied.
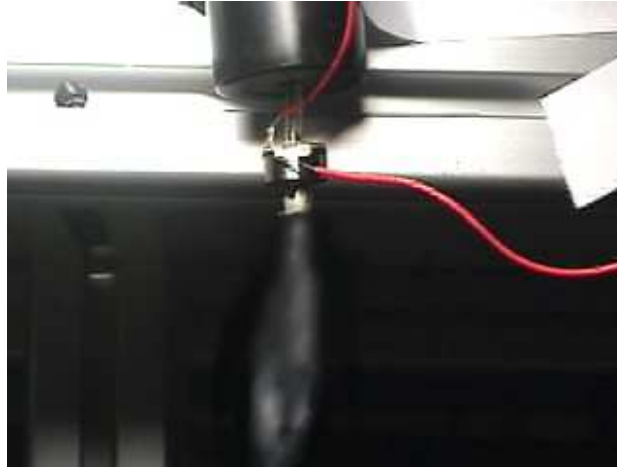
Figure 7.4   Downward nebulization under a 80V p-p driving voltage.

The nebulization shown in Figure 7.4 is downward, however a nebulizer having real value in medical applications especially in asthma therapies, needs the nebulization towards any directions. Fortunately, the working principle of our nebulizer is gravity excluded. Because in the nebulization process, the gravity of each microdrop is negligible comparing with either the surface tension before atomized or the air resistance after the droplet has been nebulized. The nebulizer performs well at horizontal and upward directions. The threshold voltage when nebulization starts is still about 54V peak-to-peak. Figure 7.5 shows a horizontal nebulization when a 120V peak-to-peak voltage is applied. An intense nebulization could be observed.

Lead-free piezoelectric ceramic based nebulizer has also been developed. $(Na_{0.5}K_{0.5})NbO_3$ (KNN) is a kind of hard lead-free ceramic; it has a lower piezoelectric performance but is more stable. Some softer lead-free ceramics

Figure 7.5   Horizontal nebulization under a 120V p-p driving voltage.

with higher d_{33} have also been tested as the driving elements of our nebulizer. They do have larger displacements under the same driving voltage, however, the ceramics depolarize quickly because of their low Curie temperature. The device is working at its resonance frequency and the electrical impedance is low, hence, heat generation during the operation is unavoidable. For KNN lead-free ceramic based nebulizer, it has a relatively lower displacement, and consequently a higher driving voltage is required to generate the necessary vibration displacement. In our experimental test, nebulzation begins with applying an 80V peak-to-peak AC voltage and the working frequency of the device is 164.8kHz which is slightly (0.3kHz) deviated from the frequency location of the displacement peak (Figure 6.12) because of the loading of water. The horn tip displacement under this threshold driving voltage is about 1.52μm which matches our preliminary estimation as well. A more intense nebulization could be achieved when 110V is applied, as shown in

Figure 7.6.
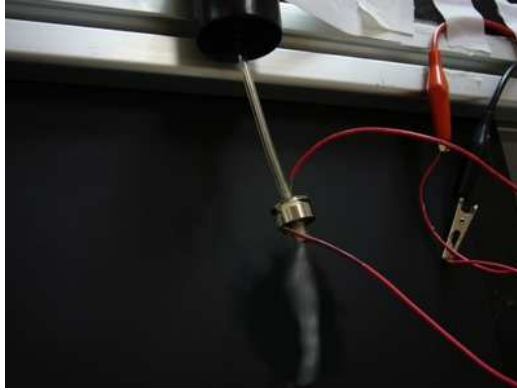
Figure 7.6   Nebulization of the lead-free ceramic based nebulizer under a driving
             voltage of 110V p-p.

Similarly, the lead-free ceramic based device could nebulize with any orientation. It reveals that the KNN lead-free ceramic has potential to be used as an alternative to PZT ceramics in nebulizer application.

Chapter 8

Conclusions and Future Work

8.1 Conclusions

A small and easy to control liquid nebulizer has been designed and developed in this project. The structure of the nebulizer is based on an ultrasonic horn transducer driven by a piece of piezoelectric ceramic. Lead-base (PZT) ceramics have been first used to drive the device. After the successful attempt using PZT, several lead-free ceramic based devices have been studied too. Good displacement performance was achieved with a solid horn on a BSZT ceramic disk and a new nebulizer was successfully developed with a hollow horn transducer on a $(Na_{0.5}K_{0.5})NbO_3$ ceramic ring.

The piezoelectric ceramics, including the PZT ones and lead-free ones, were prepared using dry pressing method. They were calcinated and then sintered. By poling at their optimum poling conditions, the ceramics exhibited good piezoelectric properties. The ceramics are characterized by the resonance method. The *IEEE* standard on piezoelectricity was used to cal-

culate the properties of each material.

Because the BSZT lead-free ceramic has a good piezoelectric property, and more importantly, its acoustic impedance is close to that of the titanium horn, the BSZT ceramic disk has been chosen as the driving element of the solid horn transducer. As the nebulizer device which is built based on a hollow horn transducer works at its resonance frequency and also a relative large power input is needed, a more stable hard ceramic KNN has been used to fabricate the lead-free nebulizer. The ceramics were glued on the horns firmly using a resin epoxy. The geometries of the hollow horn are slightly changed from the solid one, to facilitate the nebulization and to get a better match of the horns and the ceramic rings at their resonance frequencies.

To have a thorough understanding on the ultrasonic horn transducers, the longitudinal wave motion in a simple rod and a stepped horn structure has been mathematically studied through its wave equation. Also, by comparing four different horn configurations, the stepped horn was determined as the one which has the highest capacity of displacement magnification.

Finite element models of the devices have been created by a commercial FEA software package ANSYS. The modal analysis and harmonic analysis of the transducers have been conducted. The simulations accurately predicted some of the experimental results including the resonance frequencies and the modal deformations at those frequencies of the devices. The FEA work assisted the design of the transducer and enabled the optimization of the devices.

The experimental displacement measurement is performed using a laser Doppler vibrometer. This instrumentation is based upon the principle of

Doppler effect and uses a modified Mach-Zehnder interferometer. While driving by a 3V (in amplitude) sinusoidal voltage, the maximum displacement of the solid horn transducer with a PZT-402 disk is about 0.43μm at 180kHz, whereas the lead-free one (BSZT) has a displacement peak of 0.381μm at 183.6kHz. The frequency shift is due to the different acoustic velocities in PZT and BSZT, and the comparable displacement shows that BSZT has potential as a substitute to PZT in some transducer applications. The displacements of hollow horns were also measured, the transducer with lead-free ceramic KNN shows a better linearity at voltages lower than 70V, and the difference in displacement values between PZT and KNN became smaller when a larger driving voltage was applied.

Nebulization tests of the new hollow horn nebulizers have been conducted. The nebulizers are easily controlled and can generate aerosols at any orientations. The starting voltage of nebulization is 54V peak-to-peak sinusoid for the transducer based on PZT ceramic and 80V for the one with $(Na_{0.5}K_{0.5})NbO_3$. The nebulization became more intense as the driving voltage increased. Several photos were taken to record the nebulization under different circumstances.

8.2 Future Work

8.2.1 New Materials

In choosing piezoelectric ceramics for nebulizer design, there is a compromise: for obtaining large displacement, the piezoelectric ceramics are usu-

ally expected to have high piezoelectric coefficient (e.g. in soft piezoelectric ceramics). However, with the concerns about the device stability, the piezoelectric ceramics should be "harder" with higher E_C and T_C, because the device is working at its resonance mode and the large current may induce large amount of heat which depolarize or adversely influence the properties. Lead-free ceramics encounter this problem more seriously than PZT ones as some of them have lower Curie temperatures T_C and inferior piezoelectric properties compared to PZT. Hence, there are much fewer choices between performance and stability.

In our new nebulizer prototype, we adopt a hard type lead-free ceramic, $(Na_{0.5}K_{0.5})NbO_3$. It has a high T_C of about 300°C, but its poor d_{33} (less than 100pC/N) can only be compensated by lifting the operating voltages. Thus, the required driving voltage of the lead-free nebulizer is much higher than the PZT one. Therefore, it is necessary to find new materials which have better balance between the piezoelectric performance and stability. With such materials, a durable and more efficient lead-free nebulizer device could be developed.

8.2.2 Seeking a Better Match

The nebulizer device works at its resonance frequency, and this frequency is mainly decided by the whole length of the transducer and the acoustic properties of the materials. Meanwhile, the piezoelectric ceramic rings have three fundamental resonance modes (disk shaped ones have two) and these frequencies are determined by the geometry of the element. Commonly, a

good match between one of the three (two for disks) fundamental modes of the driving element and the natural frequency of the ultrasonic horn may lift the device performance. However, the accurate quantitative relation is hard to obtain because of the coupling of the two objects. Seeking a better frequency match of the horn and the ceramic ring (disk) may be helpful in the device optimization, and hence, it should be added to the list of future work.

Bibliography

[1] R. A. Millikan, The isolation of an ion, a precision measurement of its charge, and the correction of Stokes' law, *Phys. Rev.*, vol. 32, no. 4, pp. 349-397, 1911.

[2] A. Schober et al., Accurate high-speed liquid handling of very small biological samples, *BioTechniques*, vol. 15, no. 2, pp. 324-329, 1993.

[3] J. Bharathan et al., Polymer electroluminescence devices processed by inkjet printing: I. Polymer light-emitting logo, *Appl. Phys. Lett.*, vol. 72, no. 21, pp. 2660-2662, 1998.

[4] E. R. Lee, *Microdrop Generation*, CRC Press, 2003, chap. 2.

[5] H. B. Lin et al., Vibrating orifice droplet generator for precision optical studies, *Rev. Sci. Inst.*, vol. 61, no. 3, pp. 1018-1023, 1990.

[6] G. L. Switzer, A versatile system for stable generation of uniform droplets, *Rev. Sci. Inst.*, vol. 62, no. 11, pp. 2765-2771, 1991.

[7] E. Stemme et al., The piezoelectric capillary injector – A new hydrodynamic method for dot pattern generation, *IEEE Transactions on Electron Devices* vol. 20, no. 1, pp. 14-19, 1973.

[8] S. A. Elrod et al., Acoustic lens arrays for ink printing, U. S. Patent 4,751,530, 1988.

[9] I. Amemiya et al., Ink jet printing with focused ultrasonic beams, *Recent Progress in Ink Jet Technologies II*, Eric Hansen, Ed., Society for Imaging Science and Technology, 1999, pp. 275-279.

[10] G. Percin et al., Piezoelectrically actuated droplet ejector, *Rev. Sci. Inst.*, vol. 68, no. 12, pp. 4561-4563, 1997.

[11] G. Percin et al., Piezoelectric droplet ejector for ink-jet printing of fluids and solid particles, *Rev. Sci. Inst.*, vol 74, no. 2, pp. 1120-1127, 2003.

[12] G. Percin et al., Controlled ink-jet printing and deposition of organic polymers and solid particles, *Appl. Phys. Lett.*, vol 73, no. 16, pp. 2375-2377, 1998.

[13] R. Carson et al., Natural pulsations in electrical spraying of liquids, *AIAA J.* vol. 3, no. 6, pp. 1072-1075, 1965.

[14] M. Cloupeau et al., Electrohydrodynamic spraying functioning modes: a critical review, *J. Aerosol Sci.*, vol. 25, no. 6, pp. 1021-1036, 1994.

[15] A. Jaworek et al., Classification of the modes of EHD spraying, *J. Aerosol Sci.*, vol. 30, no. 7, pp. 873-893, 1999.

[16] T. Pan, Monolithic thermal ink jet printhead with integral nozzle and ink feed, U. S. Patent 4,894,664, 1990.

[17] J. D. Meyer, Thermal ink jet: Current status and future prospects, *Color Hard Copy and Graphic Arts III*, SPIE, vol. 2171, pp. 88-91, 1994.

[18] E. Manini et al., The liquid spark inkjet technology, Proceedings of the Third International Congress on Advances in Non-Impact Printing Technologies, Joseph Gaynor, Ed., Society for Imaging Science and Technology, 1987, pp. 314-321.

[19] N. Kiyohiro et al., Model for droplet ejection in the electro-rheological fluid inkjet, IS & T Eighth International Congress on Advances in Non-Impact Printing Technologies, H. Taub and E. Hanson, Eds., Society for Imaging Science and Technology, 1992, pp. 340-342.

[20] S. F. Pond, *Inkjet Technology and Product Development Strategies*, Printhead design, Torrey Pines Research, Carlsbad, CA, 2000, pp. 83-151.

[21] P. C. Reist, *Aerosol Science and Technology*, 2nd ed., McGraw Hill, New York, 1993.

[22] J. F. Dessanges, A history of nebulization, *J. of Aerosol Med.*, vol. 14, no. 1, pp. 65-71, 2001.

[23] D. R. Hess, Nebulizer: principles and performance, *Respir. Care*, vol. 45, no. 6, pp. 609-622, 2000.

[24] R. W. Niven, Atomization and nebulizers, *Inhalation aerosols: physical and biological basis for therapy*, A. J. Hickey, Ed. Marcel Dekker, New York, 1996, pp. 273-312.

[25] J. H. Dennis, A review of issues relating to nebulizer standards, *J Aerosol Med*, vol 11, no. 1, pp. 7379, 1998.

[26] L. Vecellio, The mesh nebuliser: a recent technical innovation for aerosol delivery, *Breathe*, vol. 2, no. 3, pp. 253-260, 2006.

[27] K. Nikander, et al., The conventional ultrasonic nebulizer proved inefficient in nebulizing a suspension, *J. Aerosol Med.*, vol. 12, no. 1, pp. 4753, 1999.

[28] M. T. Newhouse et al., Aerosols for systemic delivery of macromolecules, *Respir. Care Clin. N. Am.*, vol. 7, no. 2, pp. 261-275, 2001.

[29] R. Dhand, Future directions in aerosol therapy, *Respir. Care Clin. N. Am.*, vol. 7, no. 2, pp. 319-335, 2001.

[30] K. Nikander, Drug delivery systems, *J. Aerosol Med.* vol.7 (Supply), pp. S19-S24, 1994.

[31] R. M. Kaemarek, Care-giver protection from exposure to aerosolized pharmacologic agents. Is it necessary? *Chest*, vol. 100, no. 4, pp. 1104-1105, 1991.

[32] A. Clark, et al., In vitro testing of pharmaceutical aerosols and predicting lung deposition from in vitro measurements, Drug delivery to

the lung X, H. Bisgaard, et al., Ed., Marcel Dekker, New York, 2002, pp. 105-142.

[33] R. Dhand, Nebulizers that use a vibrating mesh or plate with multiple apertures to generate aerosol, *Respir Care*, vol. 47, no. 12, pp. 1406-1416, 2002.

[34] R. Dhand, New frontiers in aerosol delivery during mechanical ventilation, *Respir Care*, vol. 49, no. 6, pp. 666-677, 2004.

[35] Yasuyoshi Saito et al., Lead-free piezoceramics, *Nature* 432, pp. 84-87, 2004.

[36] N. Setter. *Piezoelectric Materials in Devices*, EPFL Swiss Federal Institute of Technology, Lausanne, 2002.

[37] Fundamentals of Piezoelectricity and Piezoelectric Actuators, tutorials on http://www.physikinstrumente.com/tutorial/4_15.html.

[38] http://www.piezo-kinetics.com/pzt.htm

[39] D. W. Richerson, *Modern ceramic engineering, properties, processing, and use in design*, Marcel Dekker, Inc., New York, 1982, pp. 178-181.

[40] W. D. Callister, *Materials science and engineering: an introduction*, 4th Ed. John Wiley & Sons, Inc., New York, 1997.

[41] *IEEE Standard on Piezoelectricity*, ANSI/IEEE Standard 176-1987.

[42] Stewart Sherrit et al., Novel Horn Designs for Ultrasonic/Sonic Cleaning Welding, Soldering, Cutting and Drilling, *Proceedings of the SPIE*

Smart Structures Conference, Vol. 4701, Paper No. 34, San Diego, CA., March 2002.

[43] The stepped horn. *Technical Publication* TP-214, Morgan Electro Ceramics.

[44] R. D. Cook, *Finite Element Modeling for Stress Analysis*, John Wiley & Sons, Inc., New York, 1995.

[45] A. A. Becker, *An Introductory Guide to Finite Element Analysis*, The American Society of Mechanical Engineers, New York, 2004.

[46] H. Allik et al., Finite Element Method for Piezoelectric Vibration, *International Journal for Numerical Methods in Engineering* 12, pp. 151-157, 1970.

[47] P. C. Kohnke, *ANSYS 5.2 User's Manual - Volume IV Theory*, ANSYS Inc., 1995.

[48] Introduction to Adaptive Finite Element Analysis for Electromagnetic Simulations. *Technical article*, International Compumag Society, UK.

[49] Principles of Vibrometry. *Measurement Solutions*, Polytec Corporation, Germany.

[50] Polytec Scanning Vibrometer PSV-300 hardware manual, Polytec Corporation, Germany.

[51] Signal Processing. *Vibrometer University*, www.polytec.com.